

**Dissertation zur Erlangung des Doktorgrades
der Fakultät für Chemie und Pharmazie
der Ludwig-Maximilians-Universität München**

**Assembly, oriented growth and
sorption behavior of microporous films**

von

Enrica Biemmi

aus Gavardo (BS), Italien

2007

Erklärung

Diese Dissertation wurde im Sinne von § 13 Abs. 3 bzw. 4 der Promotionsordnung vom 29. Januar 1998 von Herrn Prof. Dr. Thomas Bein betreut.

Ehrenwörtliche Versicherung

Diese Dissertation wurde selbstständig, ohne unerlaubte Hilfe erarbeitet.

München, am 9.11.2007

(Unterschrift des Autors)

Dissertation eingereicht am 9.11.2007

1. Gutachter: Prof. Dr. Thomas Bein
2. Gutachter: Prof. Dr. Norbert Stock

Mündliche Prüfung am 17.12.2007

per Sebastian...

*„Das Volumen des Festkörpers wurde von Gott geschaffen,
seine Oberfläche aber wurde vom Teufel gemacht.“*
(W. Pauli, Nobelpreisträger)

Preface

Acknowledgment

There is a lot of work behind this thesis, and this would have not been possible without many special people. I would like to express my thanks and gratitude to my supervisor Prof. Dr. Thomas Bein for all the guidance and encouragement he has offered me throughout the period of this research. Thank you for the stimulating ideas, the fruitful discussions and for supporting my creativity. Furthermore, I would like to thank you for the opportunity of participating to diverse international conferences, where I could exchange scientific and social experiences while visiting different countries.

My sincere acknowledgment goes to Prof. Dr. Norbert Stock from the Christian-Albrechts-Universität in Kiel, for being my second referee, for his valuable suggestions and for the active cooperation in the research work concerning metal-organic frameworks. Thank you for your passion in science, which inspire and enrich my growth as a researcher. Last but not least, thank you for the sushi, which tastes much better in Kiel!

Additionally, I would like to express my gratitude to the committee members for their time and effort in reviewing this work.

Without the funding this research work would have not been possible, therefore I would like to express my gratitude to the “Università degli Studi di Milano” for the Scholarship which gave me the opportunity to come to Munich. In addition I acknowledge the financial support by the Bayrische Forschungsstiftung in relation to the ForNano project.

I am thankful to Dr. Peter Mayer for the acquisition of the single-crystal data, to Thomas Miller for performing diffraction capillary measurements; and for the NMR measurement, I would like to thank Christian Minke.

Preface

In particular, I would like to thank all those people who made this thesis an enjoyable experience for me: "The AK Beins & Co" for our philosophical debates, exchanges of knowledge, skills, and venting of frustration during my graduate program, which helped surviving!!!

Barbara, thank you for using your precious time to read this thesis, and for the crucial comments ... Thus, you know what I am talking about! My sincere thanks go to Camilla, for being a wonderful colleague and becoming a special friend; to Hendrik and Johannes for introducing me to the "Fett war's" philosophy; to Lea for the hugs and the dancing; to Johann for being just as he is (incredible!!!) and to my "Bruder" Alex. A sincere thank goes to Ralf for the helpful discussions, and for always providing precious feedback. Tina, thanks for the sorption and the TGA measurements and for keeping my samples safe from the "Aufräumungsaktionen"!

I want to thank Keily, Andreas, Monika, Karin, Gabriela, Olivier, Markus, Steffen, Stephan, Svetlana, Nikolay and the new entries: thank to all of you for the help, the support, the wonderful atmosphere, and especially for the time spent together celebrating...

My affectionate thanks go to Stefano my "Italian Connection" for donating me true friendship, thank you! A warm thank to Parisa and Daniel for making me feel so special!

Thank you happy people! 

I cannot forget to thank all my new colleagues at Rodenstock: Katrin, Axel, Stefan, Alex, Uwe, Reiner, Marina and Dr. Herbert Schuster for supporting me during the final rush to the end of my thesis. Thank you!

My most special thanks go to my parents and family for their love, support, encouragement and patience throughout my entire life. Thanks to all my "guardian angels" for looking after me at any time.

Finally, I would like to thank my "piccolo Piddu" simply for making my life complete.

Ringraziamenti

C'è molto lavoro alla base di questa tesi, lavoro che non sarebbe stato possibile senza la presenza di tante persone speciali. Anzitutto vorrei esprimere la mia gratitudine al mio supervisore Prof. Dr. Thomas Bein per avermi offerto guida e incoraggiamento durante tutto il periodo di questa tesi di ricerca. Grazie per le idee stimolanti, per le produttive discussioni e per aver sempre supportato la mia creatività. In particolare, grazie per avermi dato la possibilità di partecipare a diverse conferenze internazionali, dove scambiare esperienze scientifiche e sociali, visitando paesi nuovi.

Il mio sincero ringraziamento va al Prof Dr. Norbert Stock della Christian-Albrechts-Universität in Kiel, per aver accettato di essere il mio secondo correlatore, per i preziosi suggerimenti e per l'attiva cooperazione nel lavoro di ricerca riguardo ai metal-organic frameworks. Grazie per la tua passione scientifica che mi è stata d'ispirazione ed ha arricchito la mia crescita di ricercatore. Infine, grazie per il sushi che a Kiel è molto più gustoso!

Inoltre vorrei esprimere la mia gratitudine ai professori della commissione di esame per il loro tempo e per l'impegno nella revisione di questa tesi.

Questo lavoro di ricerca non sarebbe stato possibile senza il contributo di preziosi finanziamenti, perciò vorrei ringraziare l'Università degli Studi di Milano per la borsa di studio che mi ha permesso di venire a Monaco. Inoltre il mio ringraziamento va alla Bayrische Forschungsstiftung per le sovvenzioni al progetto ForNano.

Sono grata al Dr. Peter Mayer per l'acquisizione dei dati di diffrazione su singolo cristallo, a Thomas Miller per le misure di diffrazione in capillare; infine, per i dati NMR vorrei ringraziare Christian Minke.

Preface

In particolare vorrei ringraziare tutte quelle persone che hanno reso lo svolgimento di questa tesi una fantastica esperienza: "Gli AK Beins & Co" per i nostri dibattiti filosofici, per lo scambio di conoscenza, e per condividere lo sfogo di frustrazione che porta la ricerca... mi avete aiutato a sopravvivere!!!

Barbara, grazie per aver investito il tuo prezioso tempo per leggere questa tesi, perdendo ore di sonno e per i commenti cruciali sui "Thus"!!! Un ringraziamento di cuore va a Camilla per essere una meravigliosa collega e per essere diventata un'amica speciale; a Hendrik e Johannes per avermi introdotto alla filosofia del "Fett war's"; a Lea per le coccole e per il ballo; a Johann per essere quello che è (incredibile!!!) e al mio "fratellone" Alex. Un ringraziamento sincero a Ralf, per le utili discussioni e per i preziosi feedback. Tina, grazie per aver effettuato misure in mia assenza e per aver protetto i miei campioni durante le azioni di pulizia!

Desidero ringraziare Keily, Andreas, Monika, Karin, Gabriela, Olivier, Markus, Steffen, Stephan, Svetlana, Nikolay e i nuovi arrivi: grazie per tutto il vostro aiuto, per la fantastica atmosfera di lavoro, ma soprattutto per il tempo passato a festeggiare insieme!!!

In mio più affettuoso ringraziamento è per Stefano la mia "Italian Connection" per avermi donato vera amicizia, grazie! Un caloroso grazie a Parisa e Daniel per farmi sentire sempre così speciale!

Non posso dimenticare di ringraziare i miei nuovi colleghi alla Rodenstock: Katrin, Axel, Stefan, Alex, Uwe, Reiner, Marina e il Dr. Herbert Schuster per avermi supportato nella fase finale della stesura di questa tesi. Grazie mille!!!

Il mio più speciale ringraziamento è dedicato ai miei genitori e alla mia famiglia per il loro amore, il supporto, l'incoraggiamento e la pazienza che mi regalano da sempre. Vi voglio bene! Grazie a tutti i miei angeli custodi per prendersi cura di me e per non farmi mai sentire sola.

Infine, il più importante ringraziamento, vorrei ringraziare il mio "piccolo Piddu" semplicemente per rendere la mia vita completa!

Abstract

This thesis is focused on the formation of thin films of nano-crystalline porous materials on gold substrates for sensor-applications on piezoelectric devices. The present work addresses several key issues related to successful sensor design, including the formation of stable and compact thin films, interfacing with an appropriate transducer concept for sensitive detection, and characterization of the porous films by means of molecular sorption experiments.

Zeolites and metal-organic frameworks (MOFs) were chosen as promising classes of microporous materials. The synthesis and the thorough characterization of such compounds were performed. Diverse zeolite structures were synthesized as nano-crystalline materials under hydrothermal conditions, LTA and ZSM-5 type structures were investigated in detail.

High-throughput methods were employed to investigate the influence of various parameters (synthesis temperature, reaction time, pH, metal salt etc.) on the formation of inorganic-organic hybrid compounds with particular attention on zinc and copper carboxylate systems. In the course of these investigations, reaction trends could be established and two new compounds with an open-framework structure ($(\text{Zn}_3(\text{OH})_2(\text{BDC})_2 \cdot 2\text{DEF}, (\text{H}_2\text{NEt}_2)_2[\text{Zn}_3(\text{BDC})_4] \cdot 3\text{DEF})$) were obtained and fully characterized.

The chemical methods to assemble thin films of porous crystals on various substrates (gold in this case) can be classified into two groups: “direct growth” and “post-synthetic crystal attachment”. To obtain a self-limiting monolayer of nanocrystals, the “post-synthetic crystal attachment” approach was investigated. The pre-synthesized crystals were chemically attached on gold surfaces by covalent bonding using appropriately functionalized organic molecules. Two different coupling strategies were explored,

Preface

concerning the modification of either the gold substrate or the external zeolite crystal surface with a bifunctional molecular interface.

The production of thin porous films opens new perspectives for potential applications of metal-organic frameworks, for example in the context of optical coatings, catalysts, or for sensor applications. The preparation and characterization of thin films of the porous metal-organic framework $\text{Cu}_3(\text{BTC})_2(\text{H}_2\text{O})_3 \cdot x\text{H}_2\text{O}$ was achieved via direct growth on functional self-assembled monolayers on a gold surface. The control of the oriented growth and the morphology of MOFs on a surface by means of SAM with different functionalities could be demonstrated for the first time. The morphological evolution of such films was investigated by following the development of the crystals.

Gas-sorption measurements of nano-zeolites (LTA, ZSM-5) and MOFs thin films were performed to test the potential of those sensing systems, using the quartz crystal microbalance technique (QCM).

Table of Content

Preface

Acknowledgment.....	i
Ringraziamenti.....	iii
Abstract.....	v

I. Introduction 1

Microporous Materials.....	2
1.1. Zeolites.....	2
1.2. Metal-Organic Frameworks.....	6
1.3. Sensors.....	10
1.4. Motivation and Goals.....	14
References.....	17

II. Materials and Synthetic Methods 21

2.1. Synthesis of Self Assembled Monolayers on Gold Substrates.....	22
2.1.1. Chemicals.....	26
2.2. Zeolites.....	26
2.2.1. Synthesis of Nano-Crystalline Zeolites.....	26
2.2.2. Assembly of Zeolite Monolayers:	
The Post-Synthetic Attachment Method.....	28
2.2.3. Chemicals.....	30
2.3. Metal-Organic Frameworks.....	31
2.3.1. Synthesis of Metal-Organic frameworks.....	31
2.3.1.1 High-Throughput Methods.....	31

2.3.2. MOFs Films Synthesis Preparation:	
The Direct Growth Method.....	33
2.3.2. Chemicals.....	34
References.....	35
III. Characterization Methods	37
3.1. X-Ray Diffraction.....	38
3.2. Scanning Electron Microscopy.....	41
3.3. Dynamic Light Scattering.....	43
3.4. Sorption Measurements.....	45
3.5. Thermogravimetric Analysis.....	52
3.6. Vibrational Spectroscopy: IR and Raman.....	52
3.7. Solid State Nuclear Magnetic Resonance.....	54
References.....	57
IV. Results and Discussion	58
4.1. Assembly on Nanozeolite Monolayers	
on the Gold Substrates of Piezoelectric Sensors.....	60
4.1.1. Results and Discussion.....	60
4.1.2. Conclusions.....	73
4.2. Screening of Synthesis Parameters in the Formation	
of MOF Employing Conventional and HT-Methods.....	74
4.2.1. Results and Discussion.....	74
4.2.1.1. Synthesis Parameter Screening in the Formation of MOF-5.....	74
4.2.1.2 Synthesis Parameter Screening in the Formation of HKUST-1.....	79
4.2.2. Conclusions.....	86

4.3. $(\text{H}_2\text{NEt}_2)_2[\text{Zn}_3(\text{BDC})_4] \cdot 3\text{DEF}$: Synthesis And Characterization of a New Metal-Organic Framework Structure with 2D Porous System.....	88
4.3.1. Results and Discussion.....	88
4.3.2. Conclusions.....	101
4.4. Oriented Growth of $\text{Cu}_3(\text{BTC})_2(\text{H}_2\text{O})_3 \cdot x\text{H}_2\text{O}$ on Gold Substrates Tunable with Functionalized Self-Assembled Monolayers.....	103
4.4.1. Results and Discussion.....	103
4.4.2. Conclusions.....	112
4.5. Direct Growth of $\text{Cu}_3(\text{BTC})_2(\text{H}_2\text{O})_3 \cdot x\text{H}_2\text{O}$ Thin Films on Modified QCM-Gold Electrodes – Water Sorption Isotherms.....	114
4.5.1. Results and Discussion.....	114
4.5.2. Conclusions.....	122
References.....	123
V. Conclusion	126
References.....	131
VI. Appendix	132
List of Abbreviations.....	133
Curriculum Vitae.....	135
Publications and Presentations.....	136
Nano-Lego Star.....	137

I. Introduction

I. Introduction

Microporous Materials

Ordered microporous materials are considered high-performance materials, such as catalysts or selective adsorbent due to their own structural features. Additionally they offer the possibility of creating functional materials by employing them as host systems or building blocks for more complex advanced architectures. [1] Two main classes of microporous materials were employed in this work: zeolites and metal-organic frameworks.

1.1. Zeolites

The term “zeolite”, which means “boiling stone” was introduced by A. Cronstedt, a mineralogist. In fact, the very first zeolite mineral he discovered (stilbite) when heated appeared to “boil” while losing water. Since then, almost 48 naturally occurring zeolites are known. [2] Besides natural zeolites, more than 150 zeolite types have been synthesized; these vary in crystal structure, chemical composition, as well as chemical and physical properties. The systematic research on the production and properties of synthetic zeolites was first started by Barrer in the forties. [3]

Many different definitions of zeolites can be found in the literature. Zeolite is defined by J.V. Smith as “an aluminosilicate with a framework structure enclosing cavities occupied by large ions and water molecules, both of which have considerable freedom of movement, permitting ion-exchange and reversible dehydration.” [4] Some years later D. W. Breck as well as P. A. Jacobs gave such a definition: “zeolites as synthesized or formed in nature are crystalline, hydrated aluminosilicates of group I and II elements. Structurally, they comprise a framework based on an infinitely extending three-dimensional network of SiO_4 and AlO_4 tetrahedra linked together through common oxygen atoms.” [5,6] R. Szostak (1989) stated that “structurally, zeolite is a crystalline aluminosilicate with a framework based on an extensive three-dimensional network of oxygen ions.” [7] While recently, Corma defined zeolites as “crystalline silicalites and aluminosilicates linked through oxygen atoms,

I. Introduction

producing a three-dimensional network containing channels and cavities of molecular dimensions.” [8] Although the four definitions are differently formulated, the main features of a zeolite are expressed as a crystalline aluminosilicate material characterized by a three-dimensional microporous framework structure built of the primary SiO_4 and AlO_4 tetrahedra that are linked through oxygen bridges.

The synthetic varieties of zeolites are among the most widely used sorbents, catalysts and ion-exchange materials in the world. [9] Zeolite crystals are porous on a molecular scale, their structures revealing regular arrays of channels and cavities (ca. 3-15 Å), creating a nanoscale labyrinth which can be filled with guest molecules. [10] The resulting molecular sieving ability has enabled the creation of new types of selective separation processes (ion exchange, sorption), and in their acid form, zeolites are probably the most important heterogeneous acid catalysts used in industry. [8,11]

To understand the different fields of application of zeolites, the structural assembly must be clarified. The elementary structural unit of the zeolite framework is a XO_4 tetrahedron, where the central position X, so-called T-atom, is either occupied by a Si^{4+} or an Al^{3+} ion. From this primary unit, a number of secondary building units (SBU) can be built by a linkage through the oxygen atom via covalent bonding, which is called an oxygen bridge. [12] The secondary building units are of simple geometric shapes, some SBUs are pictured in Figure 1.1. A zeolite structure is finally constructed from the secondary units. The preferential assembly of different SBUs leads to diverse structural classes of zeolites. The structure of zeolites can be explained with the help of polyhedra, formed by the assembly of SBUs, and through the combination of these polyhedra many different zeolite structures can be described.

I. Introduction

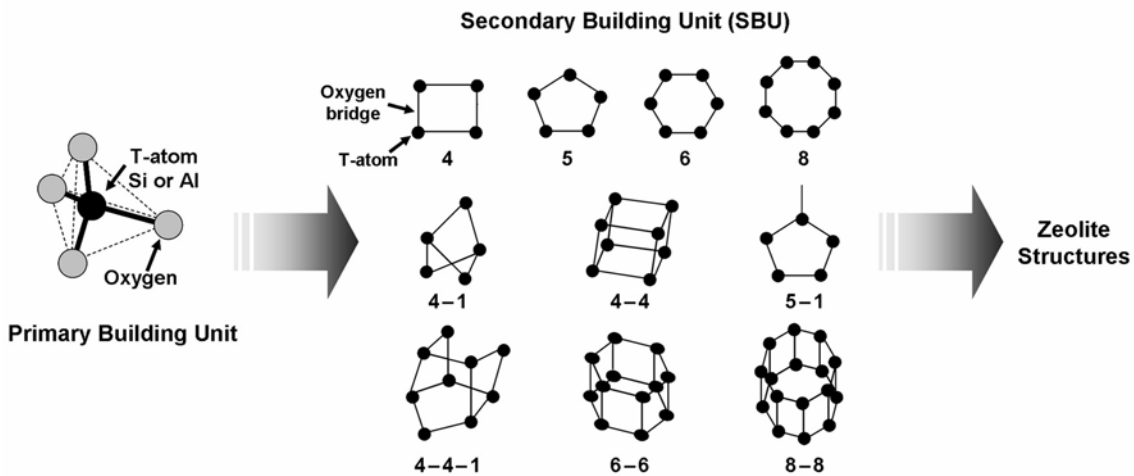


Figure 1.1. Building zeolites: from the tetrahedral unit (SiO_4 or AlO_4) many different secondary building units (SBU) can be conceptually assembled leading to different zeolite frameworks.

The polyhedral building units [13], as well as the framework structure of two industrially important zeolites (LTA and ZSM-5) are shown in Figure 1.2. In this work these two zeolites were employed as microporous materials for selective sorption of gases (see Section 4.2). Zeolite LTA (Linde Type A) can be built by connecting the quadratic faces of the β -cage (Figure 1.2a) by four-bar linkage. This assembly of the sodalite cages generates a new cavity of higher volume called α -cage. Therefore, the structure presents a three dimensional network consisting of cavities (α -cages) of 1.14 nm in diameter separated by circular openings (8-membered rings) of 0.42 nm in diameter. [14,15]

In contrast, the formation of the framework of ZSM-5 is based on the five member ring polyhedron shown in Figure 1.2c. Chains based on this tertiary building unit can be assembled. Thus, the structure of ZSM-5 results from the linkage of several chains. ZSM-5 does not present any super-cage, it has three-dimensional microporous channels with pore openings (10-member rings) of 0.53×0.56 nm for the sinusoidal channels and 0.51×0.55 nm for the straight channels. [16]

Zeolite structures find applications in many industrial areas. [17] Zeolites are used as ion-exchangers, e.g., zeolite A as a detergent builder exchanging the sodium ion of the zeolite framework for hard-water ions such as Ca^{2+} . Zeolites find application as adsorbents because of the large void fractions they contain (zeolites A have about 50% void fraction), in

I. Introduction

combination with their molecular sieve structure as well as for their hydrophilic nature. For instance, zeolite A is used to remove water, and H₂S from natural gas due to its selectivity towards polar molecules. [5] Furthermore, zeolites show shape selectivity, thus LTA is employed to separate normal paraffin from their isomers since the pore opening excludes the adsorption of the branched hydrocarbons.

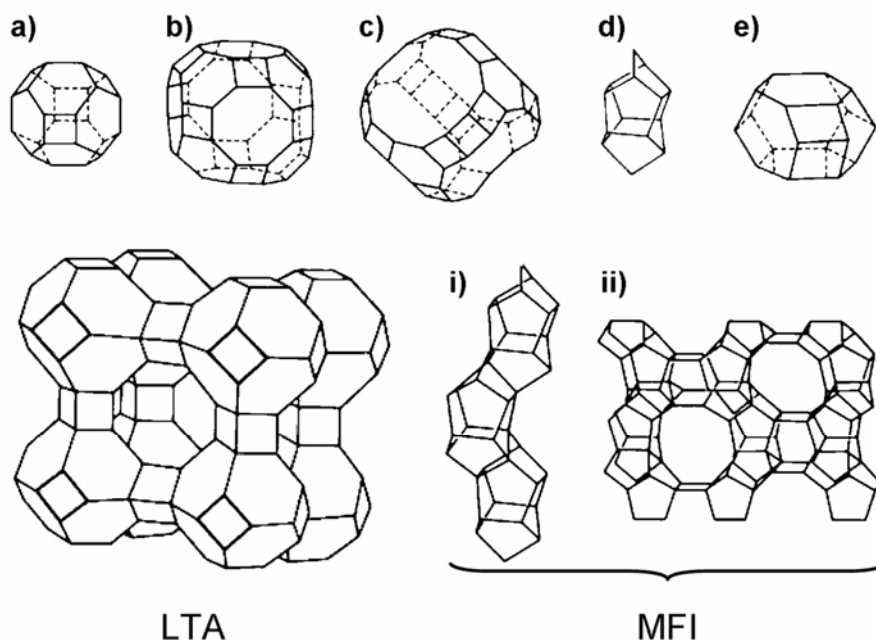


Figure 1.2. Polyhedra as tertiary building units for the assembly of zeolite structures.

a) β -cage (Sodalite-cage): building unit of zeolite A (LTA), and zeolite X (Faujasite). b) α -cage: bigger cavity characteristic of zeolite A, Rho, and ZK-5. c) bigger cavity characteristic of zeolite X. d) five member ring polyhedron of the MFI-framework (Silicalite-1, ZSM-5). e) cancrinite-cage building block of zeolites such as zeolite L.
The framework structures of LTA and ii) MFI are presented. i) The five member ring polyhedra assembled in a chain feature characterize the structure of ZSM-5.

ZSM-5 zeolite is used as fluid catalytic cracking additive that selectively cracks linear versus branched olefins producing gasoline with a higher octane number and higher yield of propylene in the gas products. The industrial process for producing dimethylbenzenes by selective toluene disproportionation when employing the 2D-pore system of ZSM-5 zeolite leads to selective formation of *p*-xylene. [18] Although all three different dimethylbenzenes are formed, the diffusion of *p*-xylene is preferred to the diffusion of *o*- and *m*-xylene which remain blocked in the channels of the structure. Such selectivity for reaction products of special size and shape is defined as “product shape selectivity”.

I. Introduction

Zeolites are typically synthesized under hydrothermal conditions [19] at temperatures up to 200 °C from clear solutions or gels. [20] Thus, most zeolite syntheses lead to micrometer-sized crystals. The increasing interest in the synthesis of zeolites as colloidal suspensions is related to the unique properties of the materials obtained by reducing the particle size to the nanometer scale. Nano-sized zeolite crystallites have been the focus of great interest due to the fact that they can be used as precursor for organizing macroscopic structures such as films or membranes. [21-25] Thus, besides the improvement of the performance of zeolites in traditional application areas (separation, catalysis), these materials can be employed in new fields of application such as chemical sensing, medical applications, and optoelectronics. [26]

1.2. Metal-Organic Frameworks

Metal-organic frameworks (MOF) represent a new class of crystalline porous inorganic-organic hybrid compounds which became subject of great academic and industrial interest in the last few years. [27-29] Due to their fascinating properties and potential applications, metal-organic frameworks (MOFs) have stimulated numerous studies on already known structures as well as the “design” of new systems. [30,31]

The success of MOF synthesis is based on the concept of network design (isoreticular chemistry). [32] Based on a certain network topology, the use of tailored ligands in combination with inorganic units (isolated metal ions as well as metal-oxygen clusters, chains or layers) allow the synthesis of porous crystalline compounds with engineered properties for applications in heterogeneous catalysis, for selective sorption and detection of molecules. [33,34] The modular assembly allows the design and control of structural features such as pore size and topology, or of chemical properties of the framework such as the presence of accessible functional groups. [35,36] New compounds (such as MIL-101)

I. Introduction

with giant pores and cages, achieving extremely high specific surface area have been prepared (Figure 1.3). [37]

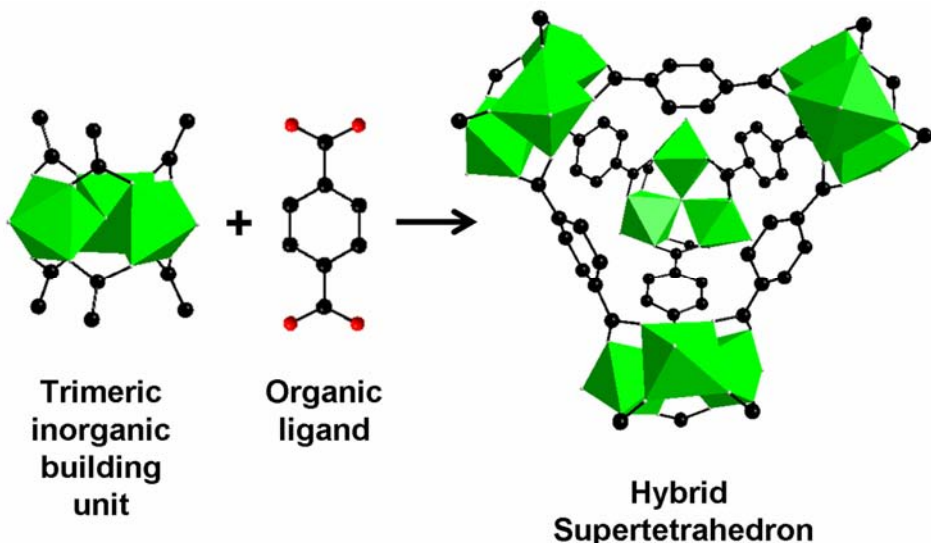


Figure 1.3. Building MOFs: the structure of MIL-101 is constructed by connecting trimers of μ_3 -oxygen bridged Cr(III)O₆ octahedra with benzene dicarboxylate (BDC) ligands into a hybrid supertetrahedron. These supertetrahedra form the vertices of an MTN-zeotype framework presenting giant pores and cages up to the mesopore range.

The use of very long ligands often results in catenated networks, with smaller specific surface area and smaller pore dimensions than the corresponding non-catenated structure. Indeed if the pores of the network are large enough to accommodate the metal-carboxylate clusters, a second network is built inside the first one. Catenation can take the form of interpenetration, where the frameworks are maximally displaced from each other, or interweaving, where they are minimally displaced and exhibit many close contacts. [38] The most immediate consequence of catenation is a reduction of the free diameter of the pores, thus, it represents a potential strategy for improving hydrogen uptake. [39]

The synthesis of the metal-organic framework (Zn₄O)(BDC)₃·(DMF)₈(C₆H₅Cl), denominated MOF-5 by the authors, [40,41] appears to be a decisive step forward in the structural chemistry of this class of compounds. The structure consists of Zn₄O clusters linked by six benzene dicarboxylate units (BDC) in a cubic network topology exhibiting a 3D porous system. The Zn₄O units are settled at each of the cube corners, while the BDC units

I. Introduction

constitute the edges. (Figure 1.4) Thus, the inorganic corners can be considered as four ZnO_4 tetrahedra, all sharing a central oxygen atom, arranged in a tetrahedral symmetry with composition $(\text{OZn}_4)\text{O}_{12}$.

According to the literature [41], MOF-5 was shown to have an apparent Langmuir surface area of $2900 \text{ m}^2 \text{ g}^{-1}$. The interconnected 3d pore system presents pore-openings of 0.8 nm , with enclosed cavities of 1.12 nm free diameter which is in the range of molecules such as cyclohexane or benzene. (Figure 1.4a, the yellow sphere represents the largest sphere that can occupy the pores without coming within the van-der-Waals surface of the framework). Since MOF-5 can be cost efficiently synthesized, from ZnO and terephthalic acid, and due to the extraordinary gas sorption properties it is of industrial interest as vessel filler enhancing the gas uptake efficiency. [29]

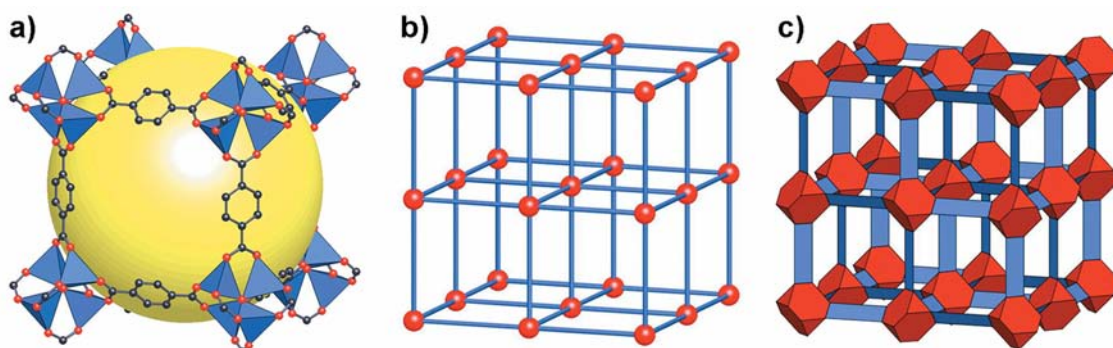


Figure 1.4. a) The MOF-5 structure shown as ZnO_4 tetrahedra (blue polyhedra) connected by benzene dicarboxylate (BDC) linkers in an extended 3D cubic framework (carbon atoms = black, oxygen atoms = red). b) Ball-and-stick model showing the topology of the structure (primitive cubic net). c) The structure is presented with the $(\text{OZn}_4)\text{O}_{12}$ cluster as red truncated tetrahedron and benzene dicarboxylate ions as blue slats. Note that opposing BDC units (slats) are all at 90° . [32]

Another example of great interest is HKUST-1, a metal-organic framework based on Cu^{2+} and 1,3,5-benzenetricarboxylate (BTC) with the chemical composition $\text{Cu}_3(\text{BTC})_2(\text{H}_2\text{O})_3 \cdot x\text{H}_2\text{O}$. HKUST-1 is composed of dimeric copper tetracarboxylate units (so called paddle wheel units) as shown in Figure 1.5a. Such bimetallic units are common features and often highly stable arrangements found for many other transition metal carboxylates. The Cu^{2+} ions are connected through a weak bond, and the residual axial coordination site is filled by a weakly bound water molecule. [42] These primary building blocks are connected through the BTC ligand in a three-dimensional cubic network with an

I. Introduction

open pore system (Figure 1.5b). This pore network consists of main channels of a square cross-section of about 0.9 nm diameter and tetrahedral side pockets of ca. 0.6 nm, connected to the main channels by triangular windows of ca. 0.35 nm. The pore volume has been determined by N₂ as well as H₂ sorption; depending on the sample preparation it varies between 0.33 and 0.62 cm³ g⁻¹. [43,44] The weakly bound water molecules point towards the center of the main pores. Thus, a hydrophilic interior characterizes the main cavity. On the other hand, the smaller pores constituted by the planar BTC-units present a more hydrophobic character. [45] Furthermore, the local structure of the framework has been characterized in detail. [46]

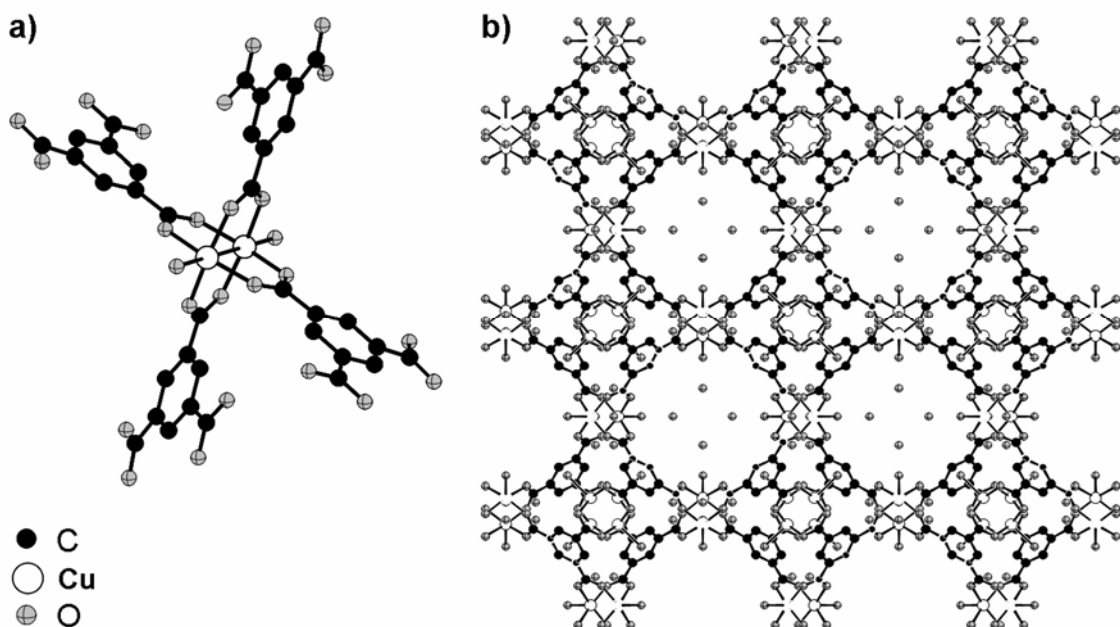


Figure 1.5. HKUST-1 framework structural features. a) paddle-wheel unit: in the cubic network, Cu₂⁺ clusters are coordinated by four carboxylate groups arranged in a square. b) View into the pore of Cu₃(BTC)₂(H₂O)₃·xH₂O. The axially bound water molecules point towards the pore center.

The structural features of HKUST-1 make this material an attractive candidate for many different applications. The unique structure features available coordination sites on the constituent Cu(II) centers which offer the potential for selective adsorption of certain molecules. This has been motivation for several studies concerning the catalytic properties of the MOF. When the coordinated water molecules are removed in vacuum, Lewis acidic Cu²⁺-sites are created and accessible for catalytic transformations. [42]

I. Introduction

Gas purification and separation [47], as well as hydrogen adsorption (storage), [39,44,48] have been studied in relation to the intriguing sorption properties and the high structural stability of HKUST-1. Employing HKUST-1, the removal of sulfur odorant components from natural gas as well as amines and ammonia, water traces, alcohols and oxygenates have been demonstrated. [29] Interestingly, in all cases a dominant color change (from deep blue to turquoise in the case of water – Figure 4.4.3) allows visible detection of breakthrough and contaminant saturation on the MOF. During removal of the contaminant by vacuum treatment or heating, the original color reappears, indicating the regeneration of the adsorbent. The axial sites, which in the as-synthesized material are occupied by removable water molecules, can potentially act as binding sites for the growth/attachment of the crystals on a self-assembled monolayer (SAM) functional surface.

The synthesis of MOFs proceeds mainly under solvothermal conditions. The common characteristic of these systems is their complex synthetic/structural space, where small changes in compositional or process parameters (reaction temperature, reaction time, metal-salt, solvent, or pH value of the reaction solution) can have a profound impact on the structures formed and their properties.

1.3. Sensors

The adsorption process in microporous systems is strongly dependent on the combination of the structural features as well as the interactions between the adsorbate and the framework, thus providing capabilities for molecular recognition.

Nature has provided many examples of specific binding interactions such as enzyme–substrate, or antigen–antibody. To achieve this specificity, biological systems have developed molecular recognition between two complementary species in terms of size, shape and functionality. These so called “lock and key” interactions have been deeply investigated for the design and synthesis of molecular receptors, to understand and mimic

I. Introduction

the specific interactions common in nature. The concepts of shape recognition as well as binding site matching are central for successful molecular recognition in artificial host-guest systems. This selectivity is necessary for the design of chemical sensors; thus the recognition process can be translated into an analytical signal. Successful sensor design requires the efficient combination of appropriate transducer concepts with receptors that can impart chemical selectivity upon the sensor.

Besides selectivity, important features for sensors include fast response and reversibility. For rapid equilibration of the sensor with molecules in the gas phase, the diffusion path in the thin films should be minimized. Reversibility of the responses requires weak interactions between the host and the guest, since the formation of covalent or ionic bonds would result in the permanent saturation of the sensing material. [49] The production of thin microporous films opens new perspectives for potential applications of those materials, for example in the context of optical coatings, catalysts, or for sensor applications. [50,51] All chemical receptors for gas and vapor sensing are used in the solid state, either in the form of organized crystalline films or amorphous layers (polymers). [52] This thesis focuses on the application of crystalline thin films as sensor systems due to the high chemical and thermal stability they present.

Different classes of host-guest materials have been employed for selective sensing applications. Besides, supramolecular organic cavitand systems (container shaped molecules) such as cyclodextrins, calixarenes, and cucurbiturils which have been thoroughly investigated for their host-guest properties, can be tunable towards the recognition of different classes of analytes. [53] Thin films of microporous materials are also of great interest due to their molecular sieving capabilities. [22,54-56] The relationship between the microscopic structure and the sorption properties allows zeolites to recognize and discriminate molecules with precision better than one Å. [57] Several synthetic schemes have been developed for the preparation of thin films, including the post-synthetic attachment of crystals to surfaces as a method to organize compact monolayers on a substrate. In this method, preformed zeolite crystals are chemically attached on substrates

I. Introduction

by ionic or covalent bonding using appropriate organic additives. Organic functional groups are tethered independently onto the zeolites and/or the substrates, followed by covalent linking of the two tethered functional groups. Yoon *et al.* have developed different strategies to organize micron-sized zeolite crystals on substrates such as glass, silicon wafers, alumina and conductive substrates. [58-62]

Biomineralisation, on the other hand, [63-65] has inspired the direct growth of zeolite-type materials on self-assembled molecular layers (SAM) thus offering the opportunity to control the orientation of the grown crystals. [66,67] Furthermore, the increasing interest in the field of metal-organic frameworks has motivated studies focused on the formation of MOF thin films. Recently the preparation of thin, patterned films of MOF-5, as well as the growth of tunable oriented films of the framework structure HKUST-1 on gold substrates on different functional-SAMs have been reported (Section 4.4). [68-70]

Acoustic wave (AW) transducers are ideal devices for applications in molecular sensing. They measure the mass uptake of a sensing layer when exposed to vapors. Usually AW sensors consist of a piezoelectric crystal with attached electrodes. When an oscillating potential is applied at a frequency near the resonant frequency of the piezoelectric crystal, a stable oscillating circuit is formed. The key feature of AW sensors is that the frequency and the amplitude of the acoustic wave are affected by a mass change of the system. The acoustic wave devices mostly employed for sensing applications are the quartz crystal microbalance (QCM) and the surface acoustic wave (SAW) resonator. In the QCM, the acoustic wave propagates through the bulk of the system in a direction normal to the surface. Therefore thickness and permeability of the layer are critical features. Whereas, in the SAW device, the generated acoustic wave propagates in a direction parallel to the surface itself. Since in SAW resonators the acoustic energy is trapped near the surface, they are potentially much more sensitive than bulk wave devices, for the same receptor layers. On the other hand they are much more sensitive to small temperature fluctuations, inhomogeneities of the sensing layer or to mechanical stresses. Thus, their handling and the interpretation of experimental results is not as straightforward as in the case of a QCM.

I. Introduction

For instance, in polymer coatings, the volume changes of the layer associated either with swelling (vapor sorption) or thermal expansion perturbs the viscoelastic properties of the coating and this significantly contributes to the observed response.

A QCM typically consists of a thin disk of quartz crystal AT-cut ($35^{\circ}10'$ with respect to the optical axis) which shows nearly zero frequency drift with temperature around RT, with key-hole gold electrodes patterned on both sides. The electrodes are thermally evaporated, in ultrahigh vacuum (UHV) conditions, onto each face of the crystal, a process which routinely yields (111) polycrystalline Au surface structures. When the electrodes are connected to an oscillator and an AC voltage is applied, the quartz crystal starts to oscillate at its resonance frequency due to the piezoelectric effect. The result of the vibrational motion of the quartz crystal is the establishment of a transverse acoustic wave that propagates across the crystal, reflecting back into the crystal at the surface. A standing wave condition can be established when the acoustic wavelength is equal to twice the combined thickness of the crystal and electrodes. Thus, the resonance frequency can be related to the thickness of the crystal by following relation: $f_0 = v_q / 2t_q$, here v_q is the velocity of the acoustic wave in AT cut quartz ($3.34 \cdot 10^4 \text{ m s}^{-1}$), f_0 is the resonance frequency of the quartz crystal prior to the mass change, t_q is the thickness of the quartz resonator. This relation assumes that the velocities of sound in the electrodes and in quartz are identical, and the thickness of the electrodes is small in comparison with that of quartz. Typical operating frequencies of the QCM lie within the range of 5 to 10 MHz.

If a rigid layer is evenly deposited on one or both of the electrodes the resonant frequency will decrease proportionally to the mass of the adsorbed layer according to the Sauerbrey

equation: $\Delta f = -\frac{2f_0^2 \Delta m}{A \sqrt{\rho_q \mu_q}}$, here Δf is the frequency change, f_0 is the resonant frequency of

the fundamental mode of the crystal (Hz), A is the piezo-active area of the electrode (cm^2), ρ_q is the density of quartz, μ_q is the shear-modulus of quartz, and Δm the mass change (g).

I. Introduction

The QCM technique has been applied to study a number of complex systems in the gas as well as in the liquid phase. Self-assembling systems, such as micellar systems (surfactants), SAM formation processes and their phase transition behavior have been deeply investigated employing this acoustic wave device. Furthermore, the QCM is suited to the study of layer-by-layer deposition, as well as electrochemical phenomena. [71,72] Moreover, sorption properties of small amounts (few µg) of porous materials in the form of thin films can be effectively investigated employing the QCM technique. [73,74]. Thus, the deposition of selective coatings on QCM devices with molecular selectivity to the sorption response is achieved. [22,54-56] In this thesis QCM devices were successfully employed to test the sorption properties and the potential sensing features of microporous materials (Sections 4.1 and 4.5)

1.4. Motivation and Goals

The present study addresses several key issues related to successful sensor design, including the formation of stable and compact thin films, interfacing with an appropriate transducer concept for sensitive detection, and characterization of the porous films by means of molecular sorption experiments. [75]

This thesis focuses on the synthesis, the characterization and the applications of crystalline microporous materials: in particular zeolites and metal-organic frameworks. The preparation of thin microporous films on acoustic wave devices such as QCMs for gas sensing was studied. Two different methods were followed in order to form thin microporous films on gold substrates: i) specific assembly of nano-crystals in a self-limiting monolayer; ii) direct growth of the crystalline phase on a functional self-assembled monolayer.

For sensor applications it is desirable to reduce the crystal size of the microporous materials since this leads to faster transport and equilibration. Combined with a high crystal

I. Introduction

density of the layer, a greater mass response in these sensors can thus be accomplished. To optimize the preparation of selective coatings, and to achieve a self-limiting crystalline monolayer, this work focuses on the “post-synthetic attachment” of nano-meter sized zeolite crystals through a molecular interface. Two different coupling strategies were explored, concerning the modification of either the gold substrate or the external zeolite crystal surface with a bifunctional molecular interface. Thus, the modified gold sensing area with a selected functionality is able to chemically bind the free OH-groups on the zeolite external surface; or a colloidal ink consisting of the functionalized nano-zeolite crystals can selectively react with the gold surface as presented in detail in Section 4.1.

To demonstrate the potential of those sensing systems, gas selective sorption measurements, based on the QCM (Quartz Crystal Microbalance), are presented in this thesis.

The chemistry of metal-organic frameworks has been intensively studied, with particular attention to porous compounds due to the many potential applications such as gas-sorption, -separation, -storage, and catalysis. [27] The synthesis and the characterization efforts have been mainly focused on bulk materials; the next step is the preparation of thin films of those compounds. The growth of one MOF-structure, MOF-5, has been reported on a SAM of COOH-terminated alkanethiols, however, this film did not show preferred crystal orientation. [68] Furthermore, the ability to control the orientation of the crystals and thus the pore-system in such films will open the way to more advanced applications such as selective gas-separation membranes or sensors.

The oriented growth of inorganic compounds such as calcium carbonate, [76] lead sulfide, [77] anatase, [78] zinc and iron oxide [79,80] and zeolites [66,67] on functionalized surfaces has been reported. Self-assembled monolayers such as alkanethiols on gold are ideal candidates for controlling oriented growth of crystalline films since they often exhibit good structural order and offer a wide variety of terminal functional groups. [81]

I. Introduction

In many metal-organic frameworks such as MOF-5, the coordination sites of the metal-ions are blocked by the ligands serving as connectors in the network. In contrast, the Cu²⁺-ions in Cu₃(BTC)₂ present residual coordination sites, on the axial-direction of the “paddle-wheel” Cu₂-cluster (Figure 1.5a), which are occupied by weakly bound water molecules. [42] In the present study, these accessible coordination sites are viewed as potential binding sites for the functional groups terminating different SAMs. The structural features and the stability as well as its intriguing sorption and catalytic properties [42,44,82] make this material an interesting candidate for the growth of thin films.

The work focused on the formation of thin films is associated with the optimization of the synthesis process of the materials involved. Whereas in the synthesis of zeolites the role of several compositional as well as process parameters is well understood, [5,7] systematic investigations of inorganic-organic hybrid compounds are still rare. [83,84] Therefore, one goal of this work was to study the influence of synthesis parameters on the formation of the metal-organic framework materials MOF-5 and HKUST-1, employing conventional as well as high-throughput methods. Thus, compositional parameters (metal salt, reagents concentration, and pH) as well as process parameters (temperature, time) were investigated in order to establish reaction trends and fields of formation (Section 4.2). In this context, high-throughput (HT) methods applied to material science allow an accelerated, systematic investigation of the reaction parameter space while consuming only a minimum amount of reagents. [85-87]

I. Introduction

References

- [1] F. Schuth, W. Schmidt, *Adv. Mater.* 14 (2002) 629.
- [2] Natural Zeolites: Occurrence, Properties, Use, Pergamon Press, Oxford, UK, 1978.
- [3] R. M. Barrer: *Zeolites and Clay Minerals as Sorbents and Molecular Sieves*, Academic Press, London, 1978.
- [4] J. V. Smith, *American Mineral Society, Special Paper* 1 (1963) 281.
- [5] D. W. Breck: *Zeolite Molecular Sieves: Structure, Chemistry, and Use*, Wiley and Sons, London, 1974.
- [6] P. A. Jacobs: *Carboniogenic Activity of Zeolites*, Elsevier Sci. Pub. Co., New York, 1977.
- [7] R. Szostak: *Molecular Sieves: Principles of Synthesis and Identification*, Van Nostrand Reinhold Catalysis Series, New York, 1989.
- [8] A. Corma, *J. Catal.* 216 (2003) 298.
- [9] C. S. Cundy, P. A. Cox, *Chem. Rev.* 103 (2003) 663.
- [10] F. Schueth, *Chem. Unserer Zeit* 29 (1995) 42.
- [11] L. Puppe, *Chem. Unserer Zeit* 20 (1986) 117.
- [12] <http://izasc.ethz.ch/fmi/xsl/IZA-SC/SBUList.htm>.
- [13] <http://izasc.ethz.ch/fmi/xsl/IZA-SC/CBUList.htm>.
- [14] T. B. Reed, D. W. Breck, *J. Am. Chem. Soc.* 78 (1956) 5972.
- [15] D. W. Breck, W. G. Eversole, R. M. Milton, T. B. Reed, T. L. Thomas, *J. Am. Chem. Soc.* 78 (1956) 5963.
- [16] D. H. Olson, G. T. Kokotailo, S. L. Lawton, W. M. Meier, *J. Phys. Chem.* 85 (1981) 2238.
- [17] M. E. Davis, *Ind. Eng. Chem. Res.* 30 (1991) 1675.
- [18] D. H. Olson, W. O. Haag, *ACS Symp. Ser.* 248 (1984) 275.
- [19] A. Rabenau, *Angew. Chem.* 97 (1985) 1017.
- [20] R. M. Barrer: *Hydrothermal Chemistry of Zeolites*, Academic Press, New York, 1982.
- [21] S. Mintova, T. Bein, *Adv. Mater.* 13 (2001) 1880.
- [22] S. Mintova, T. Bein, *Microporous Mesoporous Mater.* 50 (2001) 159.
- [23] J. Sterte, J. Hedlund, D. Creaser, O. Ohrman, W. Zheng, M. Lassinantti, Q. Li, F. Jareman, *Catal. Today* 69 (2001) 323.
- [24] K. T. Jung, Y. G. Shul, *J. Membr. Sci.* 191 (2001) 189.
- [25] S. Mintova, N. H. Olson, V. Valtchev, T. Bein, *Science* 283 (1999) 958.
- [26] L. Tosheva, V. P. Valtchev, *Chem. Mater.* 17 (2005) 2494.
- [27] S. Kitagawa, R. Kitaura, S.-i. Noro, *Angew. Chem. Int. Ed.* 43 (2004) 2338.
- [28] J. L. C. Rowsell, O. M. Yaghi, *Microporous Mesoporous Mater.* 73 (2004) 3.

I. Introduction

- [29] U. Mueller, M. Schubert, F. Teich, H. Puetter, K. Schierle-Arndt, J. Pastre, J. Mater. Chem. 16 (2006) 626.
- [30] M. J. Rosseinsky, Microporous Mesoporous Mater. 73 (2004) 15.
- [31] G. Ferey, C. Mellot-Draznieks, C. Serre, F. Millange, Acc. Chem. Res. 38 (2005) 217.
- [32] O. M. Yaghi, M. O'Keeffe, N. W. Ockwig, H. K. Chae, M. Eddaoudi, J. Kim, Nature 423 (2003) 705.
- [33] T. J. Barton, L. M. Bull, W. G. Klemperer, D. A. Loy, B. McEnaney, M. Misono, P. A. Monson, G. Pez, G. W. Scherer, J. C. Vartuli, O. M. Yaghi, Chem. Mater. 11 (1999) 2633.
- [34] A. K. Cheetham, G. Ferey, T. Loiseau, Angew. Chem. Int. Ed. 38 (1999) 3268.
- [35] N. W. Ockwig, O. Delgado-Friedrichs, M. O'Keeffe, O. M. Yaghi, Acc. Chem. Res. 38 (2005) 176.
- [36] J. L. C. Rowsell, O. M. Yaghi, J. Am. Chem. Soc. 128 (2006) 1304.
- [37] G. Ferey, C. Mellot-Draznieks, C. Serre, F. Millange, J. Dutour, S. Surble, I. Margiolaki, Science 309 (2005) 2040.
- [38] S. R. Batten, R. Robson, Angew. Chem. Int. Ed. 37 (1998) 1461.
- [39] J. L. C. Rowsell, O. M. Yaghi, Angew. Chem. Int. Ed. 44 (2005) 4670.
- [40] M. Eddaoudi, H. Li, O. M. Yaghi, J. Am. Chem. Soc. 122 (2000) 1391.
- [41] H. Li, M. Eddaoudi, M. O'Keeffe, M. Yaghi, Nature 402 (1999) 276.
- [42] K. Schlichte, T. Kratzke, S. Kaskel, Microporous Mesoporous Mater. 73 (2004) 81.
- [43] J. Lee, J. Li, J. Jagiello, J. Solid State Chem. 178 (2005) 2527.
- [44] P. Krawiec, M. Kramer, M. Sabo, R. Kunschke, H. Froede, S. Kaskel, Adv. Eng. Mater. 8 (2006) 293.
- [45] A. Vishnyakov, P. I. Ravikovitch, A. V. Neimark, M. Buelow, Q. M. Wang, Nano Lett. 3 (2003) 713.
- [46] C. Prestipino, L. Regli, J. G. Vitillo, F. Bonino, A. Damin, C. Lamberti, A. Zecchina, P. L. Solari, K. O. Kongshaug, S. Bordiga, Chem. Mater. 18 (2006) 1337.
- [47] Q. M. Wang, D. Shen, M. Bulow, M. L. Lau, S. Deng, F. R. Fitch, N. O. Lemcoff, J. Semancin, Microporous Mesoporous Mater. 55 (2002) 217.
- [48] B. Panella, M. Hirscher, H. Puetter, U. Mueller, Adv. Funct. Mater. 16 (2006) 520.
- [49] A. Hierlemann, A. J. Ricco, K. Bodenhofer, W. Goepel, Anal. Chem. 71 (1999) 3022.
- [50] E. E. McLeary, J. C. Jansen, F. Kapteijn, Microporous Mesoporous Mater. 90 (2006) 198.
- [51] J. Caro, M. Noack, P. Kolsch, R. Schafer, Microporous Mesoporous Mater. 38 (2000) 3.
- [52] L. Pirondini, E. Dalcanale, Chem. Soc. Rev. 36 (2007) 695.
- [53] D. J. Cram, Science 219 (1983) 1177.

I. Introduction

- [54] Y. Yan, T. Bein, *J. Phys. Chem.* 96 (1992) 9387.
- [55] Y. Yan, T. Bein, *Chem. Mater.* 4 (1992) 975.
- [56] Y. Yan, T. Bein, *Microporous Mater.* 1 (1993) 401.
- [57] M. E. Davis, R. F. Lobo, *Chem. Mater.* 4 (1992) 756.
- [58] S. Y. Choi, Y.-J. Lee, Y. S. Park, K. Ha, K. B. Yoon, *J. Am. Chem. Soc.* 122 (2000) 5201.
- [59] A. Kulak, Y.-J. Lee, Y. S. Park, K. B. Yoon, *Angew. Chem. Int. Ed.* 39 (2000) 950.
- [60] K. B. Yoon, *Acc. Chem. Res.* 40 (2007) 29.
- [61] K. Ha, Y.-J. Lee, H. J. Lee, K. B. Yoon, *Adv. Mater.* 12 (2000) 1114.
- [62] Y. S. Chun, K. Ha, Y.-J. Lee, J. S. Lee, H. S. Kim, Y. S. Park, K. B. Yoon, *Chem. Commun.* (2002) 1846.
- [63] D. Braga, *Angew. Chem. Int. Ed.* 42 (2003) 5544.
- [64] E. Dujardin, S. Mann, *Adv. Eng. Mater.* 4 (2002) 461.
- [65] S. Weiner, L. Addadi, *J. Mater. Chem.* 7 (1997) 689.
- [66] J. S. Lee, Y.-J. Lee, E. L. Tae, Y. S. Park, K. B. Yoon, *Science* 301 (2003) 818.
- [67] S. Feng, T. Bein, *Nature* 368 (1994) 834.
- [68] S. Hermes, F. Schroeder, R. Chelmowski, C. Woell, R. A. Fischer, *J. Am. Chem. Soc.* 127 (2005) 13744.
- [69] D. Zacher, A. Baunemann, S. Hermes, R. A. Fischer, *J. Mater. Chem.* 17 (2007) 2785.
- [70] E. Biemmi, C. Scherb, T. Bein, *J. Am. Chem. Soc.* 129 (2007) 8054.
- [71] K. A. Marx, *Biomacromolecules* 4 (2003) 1099.
- [72] C. K. O'Sullivan, G. G. Guilbault, *Biosensors & Bioelectronics* 14 (1999) 663.
- [73] I. I. Postinkov, *Acoustical Physics* 40 (1994) 586.
- [74] R. Schumacher, *Angew. Chem.* 102 (1990) 347.
- [75] S. Mintova, B. Schoeman, V. Valtchev, J. Sterte, S. Mo, T. Bein, *Adv. Mater.* 9 (1997) 585.
- [76] J. Aizenberg, A. J. Black, G. M. Whitesides, *J. Am. Chem. Soc.* 121 (1999) 4500.
- [77] F. C. Meldrum, J. Flath, W. Knoll, *J. Mater. Chem.* 9 (1999) 711.
- [78] D. Wang, J. Liu, Q. Huo, Z. Nie, W. Lu, R. E. Williford, Y.-B. Jiang, *J. Am. Chem. Soc.* 128 (2006) 13670.
- [79] J. W. P. Hsu, Z. R. Tian, N. C. Simmons, C. M. Matzke, J. A. Voigt, J. Liu, *Nano Letters* 5 (2005) 83.
- [80] B. C. Bunker, P. C. Rieke, B. J. Tarasevich, A. A. Campbell, G. E. Fryxell, G. L. Graff, L. Song, J. Liu, J. W. Virden, G. L. McVay, *Science* 264 (1994) 48.
- [81] J. C. Love, L. A. Estroff, J. K. Kriebel, R. G. Nuzzo, G. M. Whitesides, *Chem. Rev.* 105 (2005) 1103.

I. Introduction

- [82] L. Alaerts, E. Seguin, H. Poelman, F. Thibault-Starzyk, P. A. Jacobs, D. E. De Vos, *Chem. Eur. J.* 12 (2006) 7353.
- [83] S. Bauer, N. Stock, *Angew. Chem. Int. Ed.* 46 (2007) 6857.
- [84] P. M. Forster, N. Stock, A. K. Cheetham, *Angew. Chem. Int. Ed.* 44 (2005) 7608.
- [85] N. Stock, T. Bein, *Angew. Chem. Int. Ed.* 43 (2004) 749.
- [86] K. Choi, D. Gardner, N. Hilbrandt, T. Bein, *Angew. Chem. Int. Ed.* 38 (1999) 2891.
- [87] J. Klein, C. W. Lehmann, H.-W. Schmidt, W. F. Maier, *Angew. Chem. Int. Ed.* 37 (1999) 3369.

II. Materials and Synthetic Methods

II. Materials and Synthetic Methods

2.1. Synthesis of Self-Assembled Monolayers on Gold Substrates

Self-assembled monolayers (SAMs) have received considerable attention, both with respect to fundamental aspects, and in view of potential technological applications fields, such as sensing systems for molecular recognition, [1] corrosion protection, [2] substrate for crystallization, [3,4] alignment of liquid crystals, organic-molecular electronics, [5,6] and electrochemistry. [7] Self-assembled monolayers have been intensively studied as model systems for fundamental research areas such as double layer phenomena, biological membrane systems and the nature of organic/inorganic interfaces. [8-10] They can be prepared using different types of molecules and different substrates. Well-known examples are alkylsiloxane monolayers on oxidic materials (SiO_2) and alkanethiolate monolayers on metal substrates, the latter being well-defined model systems.

The preferred substrate for the preparation of alkanethiolate SAMs are Au(111) surfaces, which can be obtained either from single crystals or by evaporation of thin gold films on planar supports, typically mica, glass or silicon wafers. Different thiol-, sulfide-, or disulfide-functionalities were used to study head group - substrate interactions and different chain lengths were employed to study the importance of tail interactions. [11-13]

The commonly used preparation procedure to prepare thiol-based self-assembled monolayers is the result of studies designed to optimize the reproducibility of the prepared SAMs. It consists in the immersion of the cleaned (plasma-cleaning or oxidation in a liquid mixture) gold substrate in a diluted ethanolic solution (1-10 mM) of the desired thiol or thiol mixture for 18-24 h at RT. [14] Despite the fairly simple preparation, the complexity of the solution environment has made it difficult to characterize the dynamic aspects of this form of assembly as detailed as for the synthesis from the gas-phase. [11] The Langmuir adsorption model employed for the gas-phase assembly has been proposed as approximation of the kinetic evolution in the assembly stage. The assembly of SAMs

II. Materials and Synthetic Methods

thiolates on gold from solution is believed to be analogous to the assembly from the gas phase; [15] even though it proceeds through one or more intermediate low-coverage phases, so called “striped phases”, where alkanethiol molecules are lying flat on the gold surface. A schematic sketch of the suggested SAM formation process on such gold substrates is given in Figure 2.1.

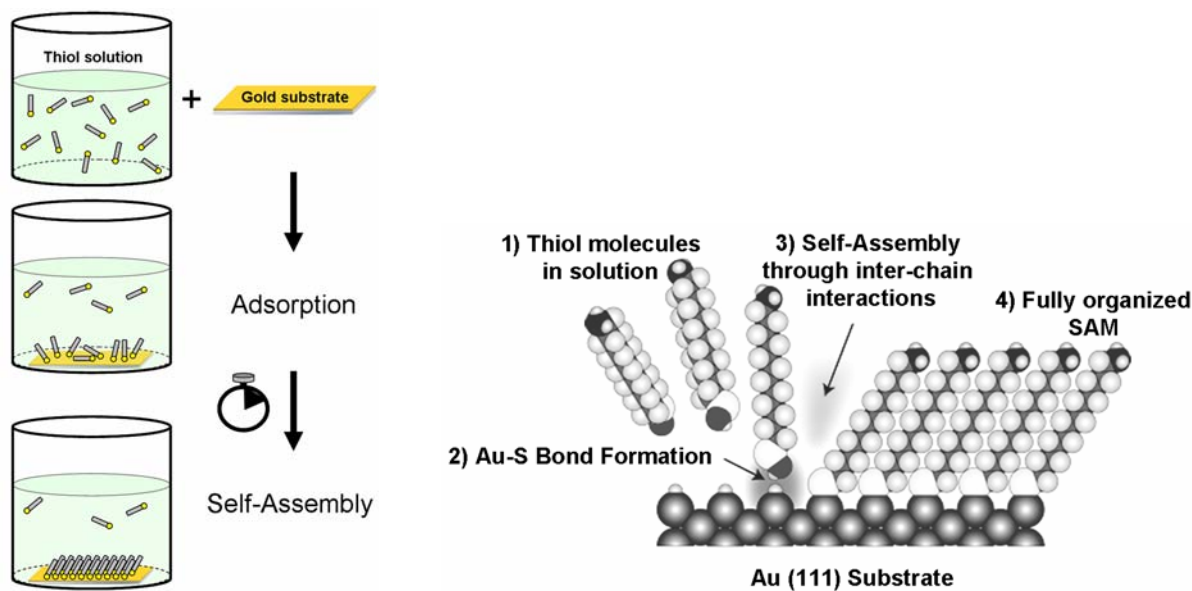


Figure 2.1. Preparation of self assembled monolayers (SAMs). The gold substrate is immersed into an 1 mM ethanol solution of the thiol(s). After an initial fast adsorption process of the thiol molecules, an organization phase takes place in which the self-assembly occurs. This step is crucial for a good quality of the self-assembled monolayers: for best results typically 24 h are required.

The ability to manipulate the structure and chemical properties of these materials, as well as their stability in both vacuum and ambient environments, make them ideal substrates for surface chemistry studies. SAMs on planar substrates have been thoroughly characterized using a number of techniques for surface analysis and spectroscopic/physical characterization such as reflectance absorption infrared spectroscopy (RAIRS), [16,17] optical ellipsometry, [18] contact angle goniometry and electrochemistry, [9] X-ray photoelectron spectroscopy (XPS), [19] as well as scanning tunneling microscopy (STM) measurements. [11] It has been shown that self assembled monolayers formed by thiols with alkane chain length of 12 or more methylene units present well-ordered and dense monolayers on Au(111) surfaces. The thiols are believed to attach primarily to the threefold

II. Materials and Synthetic Methods

hollow sites of the gold surface, losing the proton in the process and forming a $\sqrt{3} \times \sqrt{3}$ R30° overlayer structure (Figure 2.2). [20] The schematic diagram illustrates the arrangement of decanethiolates on a Au(111) lattice when maximum coverage of the thiolates is reached. This is a structural model of the layer formed by thiols on the gold lattice.

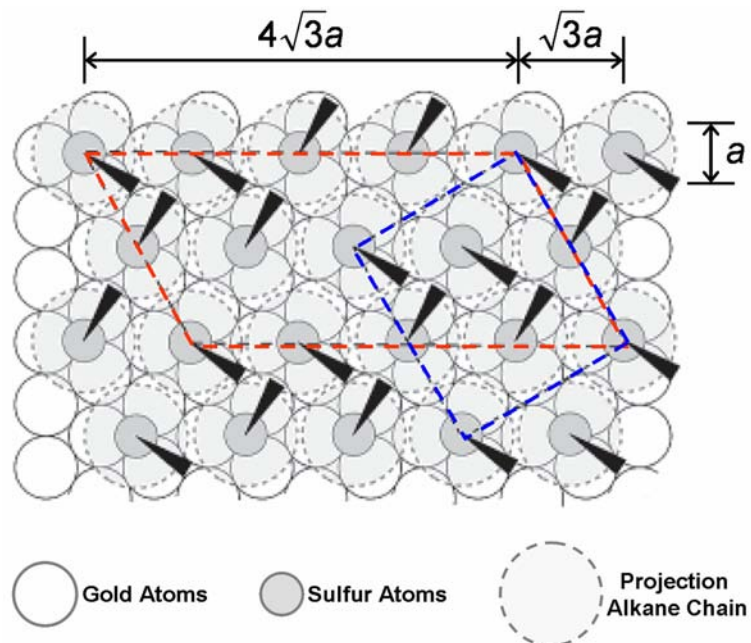


Figure 2.2. Schematic model of the $(\sqrt{3} \times \sqrt{3})R30^\circ$ overlayer structure formed by alkanethiolate SAMs on Au(111).

The arrangement shown is a $(\sqrt{3} \times \sqrt{3})R30^\circ$ structure where the sulfur atoms are positioned in the 3-fold hollows of the gold lattice (2.88 Å). The light gray circles with the dashed lines indicate the approximate projected surface area occupied by each alkane chain. The literature strongly confirms that this organization adopts a secondary ordering of the chains corresponding to a c(4 × 2) superlattice structure. [21] In Figure 2.2, the formal c(4 × 2) unit cell is marked by red dashed lines; while an equivalent $2\sqrt{3} \times 3$ unit cell is marked by blue lines. The alkane chains are tilted in the direction of their next-nearest neighbors. The distance between pinning sites in this geometry is 5.0 Å, resulting in an available area for each molecule of 21.4 Å². Since the van-der-Waals diameter of the alkane chain is somewhat too small (4.6 Å) for the chain to completely occupy that area, the chains will tilt,

II. Materials and Synthetic Methods

forming an angle of approximately 30° with the surface normal. [22] As the chain length decreases, the surface becomes increasingly disordered with low packing density and coverage. The lack of order in short chain SAMs has been attributed to a greater concentration of gauche defects and to weak interchain interactions. [18]

Considering the low thiol concentrations that are typical in the preparation of SAMs, several different solvents can be employed; care must be taken when starting from mixed thiol solutions, since the final composition of the monolayer depends on the relative solubilities of the different compounds.

The functionality of the SAM is provided by the alkane chain tail; many functional thiols are commercially available. Other functional groups can be synthesized by chemical modification of the tail group, which is possible also after formation of the SAM, taking into account potential steric impediments. Thus, the available range of functionalities can be further enlarged, providing almost infinite possibilities of variation. In this work three alkanethiols ($\text{HS}(\text{CH}_2)_n\text{X}$) were used, where n is the number of methylene units ($6 \leq n \leq 15$) and X represents the end group of the alkyl chain (- CH_3 , - OH , - COOH).

The preparation of mixed SAMs can be achieved by mixing two differently terminated thiols in the initial solution. The relative proportion of the two functionalities in the assembled monolayer will depend on the mixing ratio in solution, the lengths of the alkane chain, as well as on the solubility of the thiols in the solvent. Thiol molecules with equal alkyl chain length usually form SAMs with composition comparable to the one of the mixed solution.

In this work 1 mM solutions of different alkane thiols (see Chemicals 2.1.1) were prepared employing absolute ethanol as solvent. The gold substrates were prepared from glass slides (76 x 26 mm, Menzel-Gläser) coated with 10 nm Ti/100 nm Au by electron-beam evaporation (Advalytix AG).

II. Materials and Synthetic Methods

2.1.1. Chemicals:

• 1-Mercaptoundecane	HS(CH ₂) ₁₀ CH ₃	98 %	Aldrich
• 11-Mercaptoundecanoic acid	HS(CH ₂) ₁₀ COOH	≥ 95 %	Aldrich
• 6-Mercapto-1-hexanol	HS(CH ₂) ₅ CH ₂ OH	≥ 97 %	Fluka
• 11-Mercapto-1-undecanol	HS(CH ₂) ₁₀ CH ₂ OH	97 %	Aldrich

2.2. Zeolites

2.2.1. Synthesis of nano-crystalline Zeolites

Zeolites are typically synthesized under hydrothermal conditions [23] at temperatures up to 200 °C from clear solutions or gels. [24] Thus, most zeolite syntheses lead to micrometer-sized crystals. Crystal formation is dominated by the concepts of nucleation and crystal growth. The synthesis of zeolite nano-crystals requires conditions that favor nucleation over crystal growth in the system. Conditions that favor higher nucleation rates are for instance:

- i) low crystallization temperature (80- 100 °C), [25]
- ii) high concentration ensures high supersaturation;
- iii) high alkalinity to achieve complete dissolution of the silica and alumina species.

Additionally, the utilization of a copious amount of organic templates (often quaternary ammonium cations) provides the steric stabilization of the nuclei, and prevents further agglomeration. [26]

The zeolite crystals were prepared as colloidal suspensions by thermal treatment of clear synthesis solutions with the following molar compositions:

- zeolite A: 0.4 Na₂O : 1.9 Al₂O₃ : 14.0 (TMA)₂O : 11.9 SiO₂ : 700 H₂O
- ZSM-5: 4.5 (TPA)₂O : 0.25 Al₂O₃ : 25 SiO₂ : 599 H₂O
- Silicalite-1: 4.5 (TPA)₂O : 25 SiO₂ : 480 H₂O
- LTL: 1 SiO₂ : 0.05 Al₂O₃ : 0.5 K₂O : 20 H₂O

II. Materials and Synthetic Methods

In a typical LTA synthesis, 2.29 g of aluminum isopropoxide, and 15.04 g of tetramethylammonium hydroxide pentahydrate are first dissolved into a sodium hydroxide aqueous solution (0.1 g NaOH in 27.2 g H₂O). After stirring the mixture at RT for 24 h to obtain a clear solution, 7.04 g of an aqueous colloidal silica solution are added drop wise under vigorous stirring. The gel is aged for 72 hours at RT and finally treated in a sealed polypropylene vessel at 60 °C for 24 h.

The ZSM-5 synthesis solution is obtained by adding 17.11 g tetraethyl orthosilicate to a solution prepared by stirring for 1 h a mixture of aluminum isopropoxide (0.34 g), and 30.60 g of a 1 M solution of tetrapropylammonium hydroxide in doubly distilled water (11.70 g). After aging for 72 h, the gel is treated in a sealed polypropylene flask at 90 °C for 24 h.

For a typical batch of Silicalite-1, 22.27 g of a 1 M solution of tetrapropylammonium hydroxide and 3,744 g of dd H₂O are mixed in a polypropylene bottle and stirred for 30 minutes. After drop-wise addition of TEOS (13.39 g) to the clear solution, the mixture is aged over night. The sealed bottle is treated at 90 °C for 24 h.

LTL-type nano-crystals are prepared by adding 6.574 g of potassium hydroxide, 0.265 g of aluminum pellets and doubly distilled water (22.01 g) in a polypropylene bottle and stirring over night. To the clear solution, 20.374 g of colloidal silica are added drop wise under stirring. The resulting milky white solution is stirred for 24 h while gradually clearing up. Hydrothermal treatment is performed in a 100 ml Teflon®-lined steel autoclave at 170 °C for 4 h.

The solid phase contained in the colloidal suspensions is recovered by repeated cycles of ultracentrifugation at 19000 rpm (1 h), removal of the liquid, and ultrasonic re-dispersion (0.5 h) in fresh doubly distilled water (three times).

In order to collect the nanometer-sized crystals from the colloidal suspension, the samples are freeze-dried under vacuum. The organic template is removed by calcination in air at 420 °C for 10 h.

II. Materials and Synthetic Methods

2.2.2. Assembly of Zeolite Monolayers:

The Post Synthetic Attachment Method

The different strategies involving either the modification of the zeolite crystals or of the substrates are introduced. To optimize the preparation of selective coatings, and to achieve a self-limiting crystalline monolayer, this work focuses on the “post-synthetic attachment” of nano-meter sized zeolite crystals through a molecular interface. The assembly of nano-zeolite monolayers was achieved by the modification of the gold surfaces with a selected functionality (isocyanate) able to chemically bind the free OH-groups on the zeolite external surface (Figure 2.3).

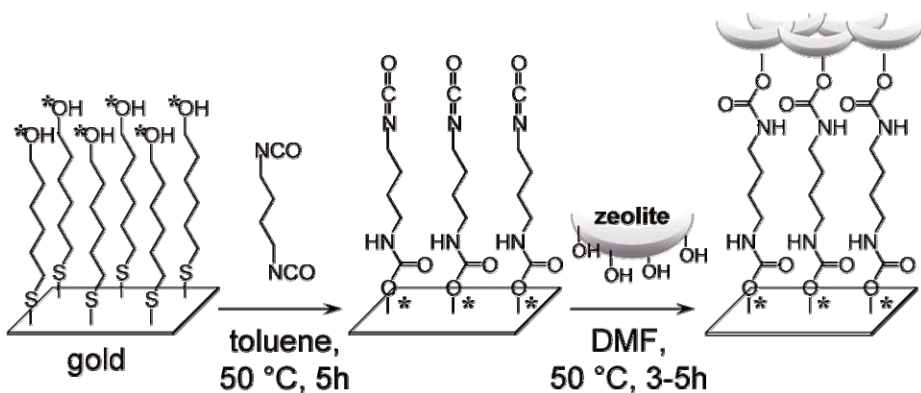


Figure 2.3. Schematic of the assembly procedure of nano-meter sized zeolite crystals to an isocyanate-functionalized gold surface. After formation of an alcohol-terminated self-assembled monolayer, the reaction with 1,4-diisocyanatobutane follows to form the urethane linkage and the active –NCO surface ready to couple with the free -OH groups of the zeolite external surface.

Assembly of nano-zeolite monolayers on isocyanate-modified gold substrates.

In a typical synthesis, the first step requires the formation of a thiol-bonded self-assembled monolayer (SAM) on the gold surfaces (Figure 2.3). In this work both gold films on glass (Advalytix AG) and QCM devices (XA 1600 AT-cut, KVG Quartz Crystal Technology) with a fundamental frequency of 10 MHz were employed as gold substrates. Prior to the attachment of the functionalized monolayer, each gold substrate was plasma-cleaned for 20 min. in 12 mbar oxygen. The pre-treated gold substrates were immersed in 20 ml of a 1 mM ethanolic solution of 6-mercaptop-1-hexanol for reaction times between 24 and 48 h.

II. Materials and Synthetic Methods

The following step implies the reaction between the OH-groups on the modified gold surfaces and 1,4-diisocyanatobutane to form an isocyanate-functionalized surface through a urethane bridge. The OH-functionalized gold substrates were removed from the SAM solution and washed repeatedly with ethanol and finally with anhydrous toluene. In a glass flask, the devices were positioned up-right on a Teflon holder, and covered with a 0.1 M solution of the isocyanate in water-free toluene. The mixture was gently stirred for 5 h at 50 °C (the low temperature ensures the stability of the self-assembled monolayer). After removing the treated gold surfaces from the cooled reaction solution, they were repeatedly washed with anhydrous toluene and directly immersed in a colloidal suspension of the zeolite crystals in water-free N,N-dimethylformamide (DMF). The coupling of the zeolite crystals with the gold substrates was performed at 50 °C for 3 to 5 h under moderate stirring (50 rpm) to maintain a homogeneous mixture. The produced zeolite-monolayers were subsequently removed from the reaction flask and weakly sonicated in fresh DMF for 10 s to remove the physisorbed crystals. All experiments were carried out under inert atmosphere (Ar flow), as the procedure is extremely water-sensitive.

In a second approach, the modification of the nano-zeolite crystals was performed to produce a colloidal ink capable of selective reaction with the gold surfaces. The nano-zeolite crystals were modified by grafting reaction with (3-mercaptopropyl)-trimethoxysilane; followed by specific reaction with the metal surface, as gold shows strong specific interactions with thiol groups (Figure 2.4).

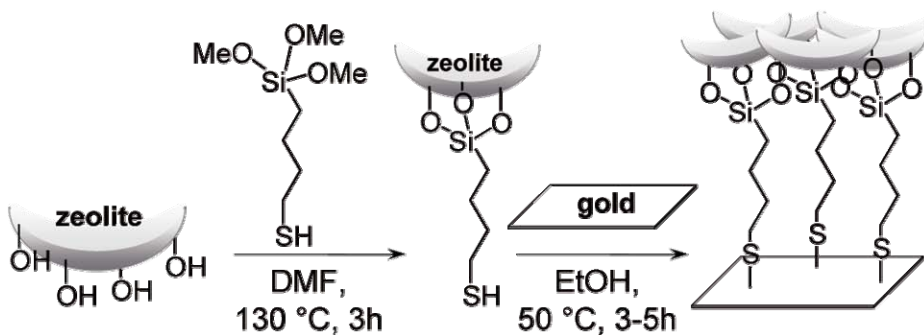


Figure 2.4. Schematic of the assembly of SH-functionalized nano-zeolite on bare gold surfaces. The external surface of the zeolite nano-crystal is modified by grafting reaction with (3-mercaptopropyl)-trimethoxysilane. The thiol-zeolite crystals are directly linked to the clean gold substrate.

II. Materials and Synthetic Methods

Assembly of SH-functionalized nano-zeolite on bare gold surfaces.

In a typical synthesis prior grafting reaction, the excess of water present in the freeze-dried zeolite samples was partially removed by repeated cycles of vacuum treatment (30 min) under argon at 50 °C. Then, 40 ml anhydrous DMF are added to 200 mg of zeolite powder and sonicated for 1 h to achieve good re-dispersion of the crystals. The grafting agent (3-mercaptopropyl)-trimethoxysilane, 0.6 ml, is added to the zeolite suspension and the mixture stirred under argon at 130 °C for 3 h. The functionalized crystals are then washed by a series of high speed centrifugation steps (30 min at 19000 rpm, 3 times), and re-dispersion in fresh solvent: DMF (2 times) and finally absolute ethanol. The linking of the MPS-zeolite suspension to the bare gold substrates is realized by soaking the plasma-cleaned gold substrates in the crystal suspension for 3 to 5 h at 50 °C. After cooling at RT, the devices are carefully washed with copious amounts of ethanol and dried at 60 °C. The organic template is removed by calcination in air at 420 °C for 10 h.

2.2.3. Chemicals:

• Sodium Hydroxide	NaOH	≥ 98.5 %	Fluka
• Potassium Hydroxide	KOH	≥ 85 %	Aldrich
• Aluminum Isopropoxide	Al(OiPr) ₃	98 %	Aldrich
• Aluminium Pellets	Al	99.99 %	Aldrich
• Tetramethylammonium (TMAOH) Hydroxide Pentahydrate	(CH ₃) ₄ NOH·5H ₂ O	97 %	Aldrich
• Tetrapropylammonium (TPAOH) Hydroxide	(C ₃ H ₈) ₄ NOH	1 M sol.	Aldrich
• Colloidal Silica Ludox HS-30	SiO ₂	30 wt %	Aldrich
• Tetraethyl Orthosilicate (TEOS)	Si(OEt) ₄	≥ 98 %	Fluka
• 6-mercaptop-1-hexanol	HS(CH ₂) ₅ CH ₂ OH	≥ 97 %	Fluka
• 1,4-diisocyanatobutane	OCN(CH ₂) ₄ NCO	97 %	Aldrich
• Toluene anhydrous (over molecular sieves)	C ₆ H ₅ CH ₃	≥ 99.7 %	Fluka
• N,N-dimethylformamide (DMF) (over molecular sieves)	HCON(CH ₃) ₂	≥ 99.8 %	Fluka

II. Materials and Synthetic Methods

2.3. Metal-Organic Frameworks

2.3.1. Synthesis of Metal-Organic Frameworks

The systematic screening of reaction parameters of two MOFs, $Zn_4O[(OOC)_2\cdot C_6H_4]_3$ (MOF-5) [27] and $(Cu_3[(OOC)_3C_6H_3]_2(H_2O)_3\cdot xH_2O)$ (HKUST-1) [28] was performed in this thesis employing HT as well as conventional methods.

The metal-organic frameworks were synthesized under solvothermal conditions and the typical recipes employed are described in the following:

MOF-5: The framework structure is typically synthesized from a clear solution of *N,N'*-diethylformamide (DEF) (5 ml), Zn(NO₃)₂·6H₂O (178.5 mg, 0.6 mmol) and 1,4-benzenedicarboxylic acid (33.2 mg, 0.2 mmol) at 105 C for 18-24 h. The reaction product is filtered off, rinsed with fresh DEF, and dried in air at RT.

HKUST-1: In a typical synthesis, a water solution (12 ml) of 0.837 g (3.6 mmol) Cu(NO₃)₂·2.5H₂O (98%, Aldrich) was added to an absolute ethanol solution (12 ml) of 0.42 g (2.0 mmol) of 1,3,5-benzentricarboxylic acid (%), Fluka) in a sealed-glass reactor, and left for 8 days in a preheated oven at 75 °C.

2.3.1.1. High-throughput methods

High-throughput (HT) methods applied to materials science allow an accelerated, systematic investigation of the reaction parameter space while consuming only a minimum amount of reagents. [29-31] The influence of synthesis parameters (reaction temperature, reaction time, metal-salt, solvent, or pH value of the reaction solution) on the formation of

II. Materials and Synthetic Methods

the metal-organic frameworks (MOFs) was studied in this context employing HT methodology.

For the HT screening a reactor block with 24 cavities containing Teflon[®] liners was used (Figure 2.5). A multiclave system based on the 96 well-plate format was previously developed in our group and was described previously. [29] The reactor block is made of stainless steel and contains 24 reaction chambers organized in a 4 × 6-array. The inserted miniaturized Teflon[®] reactors with an inner diameter of 14 mm and a depth of 25 mm provide an inert reaction environment and offer a maximal volume of 3.4 ml. This allows us to use reactant volumes of up to 2 ml per hole. The reactor block is covered with two Teflon[®] sheets (0.25 and 1 mm, respectively), and is then sealed inside a stainless steel autoclave. The top part consists of a plate with an array of 4 × 6 metal pins that permit the individual sealing of each Teflon[®] reactor.

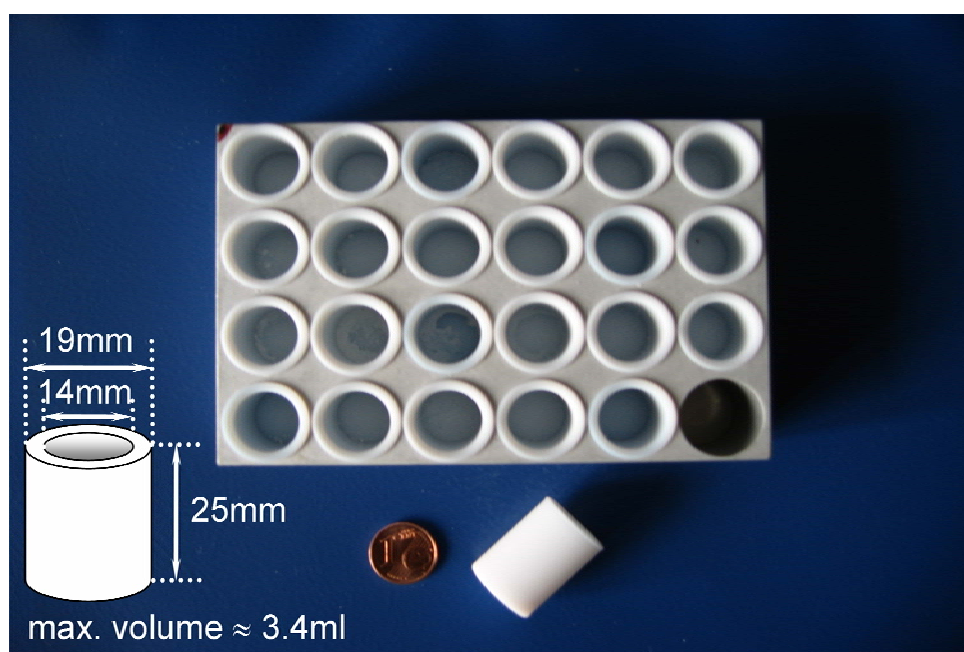


Figure 2.5. Multiclave used for the screening of the influence of synthesis parameters on the formation of metal-organic frameworks. The stainless steel reactor block contains 24 reaction chambers with inserted miniaturized Teflon[®] reactors organized in a 4 × 6-array.

All reaction mixtures in this study were homogenized for 10 min using small stirring bars previous to the solvothermal treatment. The sealed multiclave is placed in a preheated oven for several hours. After cooling to room temperature, the reaction products are recovered

II. Materials and Synthetic Methods

by filtration. The content of each reactor is filtered and rinsed with the appropriated solvent on a vacuum filtering apparatus consisting of aluminum block with a matching hole pattern and filtrate reservoir. The molar ratios and the exact amounts of starting materials for the reported HT-experiments are given in the result and discussion part of this thesis (Section 4.2).

2.3.2. MOFs Films Synthesis Preparation: The Direct Growth Method

In a typical synthesis, the gold-coated slides (glass slides ($76 \times 26 \text{ mm}^2$) coated with 10 nm Ti / 100 nm Au by electron-beam evaporation (Advalytix AG), were cut in smaller pieces ($10 \times 13 \text{ mm}^2$), cleaned in a piranha solution ($\text{H}_2\text{SO}_4(95\text{-}98\%) : \text{H}_2\text{O}_2(30\%)$ - 3:1), and than treated 20 min in a 12 mbar oxygen-plasma. The cleaned gold slides were immersed in a 1 mM ethanolic solution (6 pieces in 30 ml) of the desired thiol, and left at RT for 48 h.

The alkanethiols employed in this work: 11-mercaptop-1-undecanol, 11-mercaptoundecanoic acid, and 1-mercaptoundecan. The SAM-functionalized gold slides were repeatedly washed with ethanol, and stored in fresh absolute ethanol till needed. The SAM-functionalized gold-slides were placed upside-down on Teflon -supports in a clear HKUST-1 crystallization solution (3 pieces in 20 ml). The growth step takes place at RT in a closed glass reactor. For the kinetic investigation the slides were removed after various immersion times (8-210 h). Typically the crystallization solution is prepared with the following procedure: the synthesis mixture of HKUST-1 is prepared in a sealed-glass reactor, and left for 8 days in a preheated oven at 75 °C. After cooling the HKUST-1 synthesis mixture in a water/ice bath, the crystalline product was filtrated and stored for further characterization. The filtrated solution was used as crystallization sol for growing the films. The schematic illustration of the HKUST-1 films preparation procedure is shown in Figure 2.6. For sorption studies thin films of HKUST-1 were prepared on the gold electrode of a quartz-crystal microbalance (QCM), by direct growth on a 11-mercaptoundecanol self-assembled monolayer (SAM).

II. Materials and Synthetic Methods

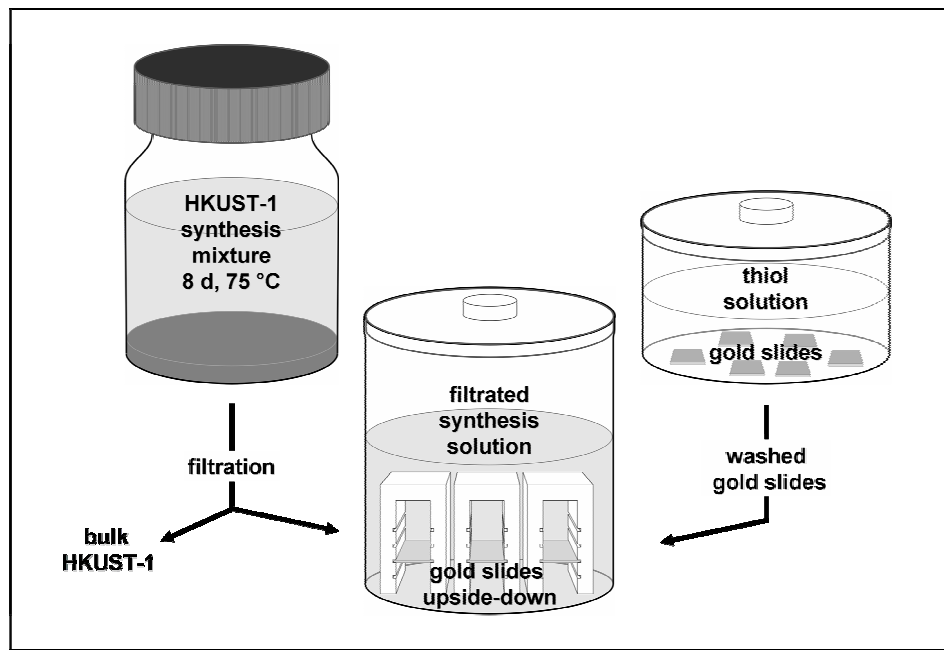


Figure 2.6. Schematic illustration of the HKUST-1 film preparation procedure.

2.3.3. Chemicals:

• Zinc(II) Nitrate hexahydrate	Zn(NO ₃) ₂ · 6H ₂ O	98 %	Acros
• Zinc(II) Oxyde	ZnO	≥ 99.0 %	Fluka
• Zinc(II) Acetate dihydrate	Zn(CH ₃ COO) ₂ · 2H ₂ O	p.a.	Merck
• Zinc(II) Chloride	ZnCl ₂	≥ 98.0 %	Fluka
• Zinc(II) Sulfate heptahydrate	ZnSO ₄ · 7H ₂ O	p.a.	Fluka
• Copper(II) Nitrate hemipentahydr.	Cu(NO ₃) ₂ · 2.5H ₂ O	98 %	Aldrich
• Copper(II) Acetate hydrate	Cu(CH ₃ COO) ₂ · H ₂ O	p.a.	Merck
• Copper(II) Chloride dihydrate	CuCl ₂ · 2H ₂ O	99 %	Grüssing
• 1,4-benzenedicarboxylic acid (H ₂ BDC)	C ₆ H ₄ (COOH) ₂	98 %	Aldrich
• 1,3,5-benzentricarboxylic acid (H ₃ BTC)	C ₆ H ₃ (COOH) ₃	98 %	Fluka
• N,N'-diethylformamide (DEF)	(CH ₂ CH ₃) ₂ NCHO	≥ 98 %	Fluka
• Mesitylene	C ₆ H ₄ (CH ₃) ₂	≥ 98 %	Merck
• Chlorobenzene	C ₆ H ₅ Cl	≥ 99 %	Merck
• Toluene anhydrous (over molecular sieves)	C ₆ H ₅ CH ₃	≥ 99.7 %	Fluka
• Ethanol Absolute	CH ₃ CH ₂ OH	99.98 %	BfB

II. Materials and Synthetic Methods

References

- [1] A. Y. Lee, A. Ulman, A. S. Myerson, *Langmuir* 18 (2002) 5886.
- [2] Y. Xia, X.-M. Zhao, G. M. Whitesides, *Microelectron. Eng.* 32 (1996) 255.
- [3] J. Aizenberg, A. J. Black, G. M. Whitesides, *J. Am. Chem. Soc.* 121 (1999) 4500.
- [4] E. Biemmi, C. Scherb, T. Bein, *J. Am. Chem. Soc.* 129 (2007) 8054.
- [5] A. M. Rawlett, T. J. Hopson, I. Amlani, R. Zhang, J. Tresek, L. A. Nagahara, R. K. Tsui, H. Goronkin, *Nanotechnology* 14 (2003) 377.
- [6] K. K. Berggren, A. Bard, J. L. Wilbur, J. D. Gillaspy, A. G. Helg, J. J. McClelland, S. L. Rolston, W. D. Phillips, M. Prentiss, et al., *Science* 269 (1995) 1255.
- [7] C. E. D. Chidsey, R. W. Murray, *Science* 231 (1986) 25.
- [8] A. Ulman: An Introduction to Ultrathin Organic Films: from Langmuir-Blodgett to self-assembly Academic Press, San Diego (CA), 1991.
- [9] G. M. Whitesides, P. E. Laibinis, *Langmuir* 6 (1990) 87.
- [10] L. H. Dubois, R. G. Nuzzo, *Annu. Rev. Phys. Chem.* 43 (1992) 437.
- [11] G. E. Poirier, *Chem. Rev.* 97 (1997) 1117.
- [12] L. H. Dubois, B. R. Zegarski, R. G. Nuzzo, *J. Am. Chem. Soc.* 112 (1990) 570.
- [13] P. Fenter, A. Ulman: Thin Films: Self-Assembled Monolayers of Thiols, Academic Press, San Diego, 1997.
- [14] C. D. Bain, E. B. Troughton, Y. T. Tao, J. Evall, G. M. Whitesides, R. G. Nuzzo, *J. Am. Chem. Soc.* 111 (1989) 321.
- [15] F. Schreiber, *Prog. Surf. Sci.* 65 (2000) 151.
- [16] D. L. Allara, R. G. Nuzzo, *Langmuir* 1 (1985) 52.
- [17] D. Roy, J. Fendler, *Adv. Mater.* 16 (2004) 479.
- [18] M. D. Porter, T. B. Bright, D. L. Allara, C. E. D. Chidsey, *J. Am. Chem. Soc.* 109 (1987) 3559.
- [19] A.-S. Duwez, *J. Electron Spectrosc. Relat. Phenom.* 134 (2004) 97.
- [20] L. H. Dubois, B. R. Zegarski, R. G. Nuzzo, *J. Chem. Phys.* 98 (1993) 678.
- [21] N. Camillone, III, C. E. D. Chidsey, G. Y. Liu, G. Scoles, *J. Chem. Phys.* 98 (1993) 3503.
- [22] J. C. Love, L. A. Estroff, J. K. Kriebel, R. G. Nuzzo, G. M. Whitesides, *Chem. Rev.* 105 (2005) 1103.
- [23] A. Rabenau, *Angew. Chem.* 97 (1985) 1017.
- [24] R. M. Barrer: Hydrothermal Chemistry of Zeolites, Academic Press, New York, 1982.
- [25] N. N. Feoktistova, S. P. Zhdanov, W. Lutz, M. Buelow, *Zeolites* 9 (1989) 136.
- [26] L. Tosheva, V. P. Valtchev, *Chem. Mater.* 17 (2005) 2494.
- [27] H. Li, M. Eddaoudi, M. O'Keeffe, M. Yaghi, *Nature* 402 (1999) 276.

II. Materials and Synthetic Methods

- [28] S. S. Y. Chui, S. M. F. Lo, J. P. H. Charmant, A. G. Orpen, I. D. Williams, *Science* 283 (1999) 1148.
- [29] N. Stock, T. Bein, *Angew. Chem. Int. Ed.* 43 (2004) 749.
- [30] K. Choi, D. Gardner, N. Hilbrandt, T. Bein, *Angew. Chem. Int. Ed.* 38 (1999) 2891.
- [31] J. Klein, C. W. Lehmann, H.-W. Schmidt, W. F. Maier, *Angew. Chem. Int. Ed.* 37 (1999) 3369.

III. Characterization Methods

III. Characterization Methods

3.1. X-ray Diffraction

X-ray diffraction (XRD) is a non-destructive characterization method that permits the determination of the structural features of crystalline materials. X-rays are electromagnetic radiation with typical photon energies in the range of 100 eV – 100 keV. For diffraction applications, only short wavelength X-rays (hard X-rays) in the range of a few angstroms to 0.1 angstrom (1 keV – 120 keV) are used. Because the wavelength of X-rays is comparable to the size of atoms, they are ideally suited for probing the structural arrangement of atoms and molecules in a wide range of materials. The energetic X-rays can penetrate deep into the materials and provide information about the bulk structure.

X-rays are produced generally by either X-ray tubes or synchrotron radiation. In an X-ray tube, X-rays are generated when a focused electron beam, accelerated across a high voltage field, bombards a stationary or rotating solid target. As electrons collide with atoms in the target and slow down, a continuous spectrum of X-rays is emitted, which is termed bremsstrahlung radiation. The high energy electrons also eject inner shell electrons in atoms through ionization processes. When another electron fills the shell, an X-ray photon with energy characteristic of the target material is emitted. Common targets used in X-ray tubes include the metals Cu and Mo, which emit 8 keV and 14 keV X-rays with corresponding wavelengths of 1.54 Å and 0.8 Å, respectively. The energy E of an X-ray photon and its wavelength is related by the equation:

$$E = hc/\lambda \quad (3.1)$$

where h is Planck's constant and c is the speed of light. Since X-ray wavelengths are comparable with the distances between lattice planes (about 150 pm), they are diffracted when passing through a crystal. These re-emitted wave fields interfere with each other either constructively or destructively, producing a diffraction pattern on a detector. The resulting wave interference pattern is the basis of diffraction analysis. The easiest approach to the analysis of diffraction patterns is to consider a lattice plane as a mirror, and to view a crystal as stacks of reflecting lattice planes at distance d (Figure 3.1). This model simplifies

III. Characterization Methods

the calculation of the angle the crystal must assume in respect to the incoming X-rays beam to reach constructive interference. The equation describing the X-ray “constructive reflection” is known as Braggs law. [1] This is defined as:

$$n\lambda = 2d \sin(\theta) \quad (3.2)$$

where λ is the wavelength of the X-rays, n is an integer number, d is the separation of the lattice planes and θ the glancing angle (Bragg angle). When the incident beam is perpendicular to the lattice plane ($\theta=90^\circ$), the Bragg law is reduced to $n\lambda = 2d$. Thus, the minimum d -spacing detectable is half of the wavelength characteristic of the incident X-ray. The extension of Bragg’s model of a diffraction grating to three dimensions is known as Laue’s analyses. [2] When satisfying the Bragg conditions, a constructive interference occurs between the reflected incoming X-ray beams. The increase in the spot intensity, which results from the constructive interference, is called reflection. An X-ray diffraction pattern of a crystalline substance is a set of lines (reflections), each of different intensity and position (d -spacing or angle 2θ). The intensity of the reflections is proportional to the product of the intensity of the incident beam and the density of electrons in the lattice plane that is reflecting the beam. The combination of different d -spacing and intensities is characteristic for any crystalline material. Thus, XRD allows the identification of a compound in a specific crystalline phase.

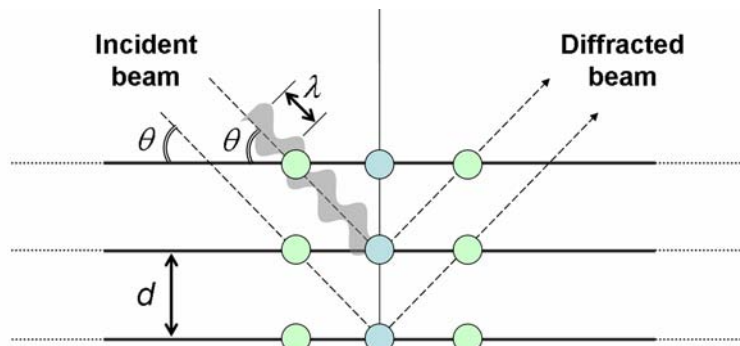


Figure 3.1. Schematic diagram illustrating the derivation of the Bragg Law.

Powder samples are characterized by a large number of microcrystallites randomly oriented around the direction of the incident beam. The various lattice planes are present as well in

III. Characterization Methods

random orientation; thus, the diffraction pattern is formed by cones of diffraction produced from all the sets of planes that satisfy the Bragg conditions. Powder diffraction patterns allow quick identification of crystalline phases by comparison with sample libraries. Scherrer (1918) first observed that small crystallite size could give rise to peak broadening. Thus, incomplete destructive interference occurs in very small crystalline domains (≤ 100 nm). To obtain information about the crystalline domain size (D), which for nano-sized crystals in most cases coincides with the particle size, the Scherrer equation can be applied:

$$D = \frac{K\lambda}{\beta \cos(\theta)} \quad (3.3)$$

here λ is the wavelength, K is the Scherrer constant whose value is approximately 0.9, β is the integral width of a reflection (in radians 2θ) located at 2θ , and θ is the Bragg angle. This equation offers a simple relationship between crystallite size and peak broadening. Since the results are volume weighted, it must be taken into account that the contribution of even a small amount of larger particles will dominate. [3,4]

All powder samples were measured on a Stoe STADI P COMBI transmission X-ray powder diffractometer equipped with an image plate detector and a horizontal xy-stage for automated analysis. The diffraction patterns were collected in the range of -45 – 45 degree (2θ) using Cu $K\alpha_1$ radiation ($\lambda = 154.18$ pm) with an acquisition time for each measurement of 11 min. The horizontal position of the sample holder is automatically tilted stepwise from -5 to +5 degree during the entire measurement. To obtain the final diffraction patterns, the recorded data were read from the image plate and folded ($0 \leq 2\theta \leq 45$).

The diffraction patterns of thin films were collected in reflection geometry between 5 and 20 degree (2θ), on a XDS-2000 diffractometer (Scintag Inc.) using Cu $K\alpha_1$ radiation ($\lambda = 154.18$ pm). The measurements were performed in theta/theta mode, with a step-size of 0.02 degree, and a scan-rate of $0.004 2\theta s^{-1}$.

III. Characterization Methods

3.2. Scanning Electron Microscopy

Electron microscopy is basically used in the reflection (SEM) or transmission mode. Scanning electron microscopy (SEM) is a method for high-resolution imaging of surfaces to characterize the morphology and topography of samples at very high magnifications. The resolution limits of optical microscopy imposed by the wavelength of light limit the measurement applicability to objects of few microns. Electron microscopy offers extremely detailed structural information over a broad range of magnifications (up to 300,000X) and much greater depth of field using a beam of accelerated electrons. This type of electron microscopy covers the magnification range between the lower resolution limit of optical microscopy ($\sim 1\mu\text{m}$) and the upper practical limit of TEM. The schematic representation of an SEM is shown in Figure 3.2.

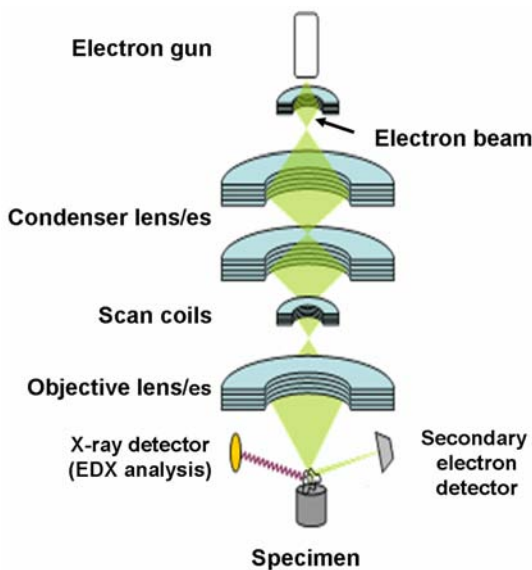


Figure 3.2. Schematic representation of the basic components of a scanning electron microscope.

The electrons emitted from a filament (electron gun) are accelerated through high voltage. Their wavelength is related to the accelerating voltage, V by the equation:

$$\lambda = \frac{h}{(2meV)^{\frac{1}{2}}} \quad (3.4)$$

with m and e the mass and charge of the electron, respectively. The electron beam is condensed by the first condenser lens. This lens is used to both form the beam and limit the

III. Characterization Methods

amount of current in the beam. It works in conjunction with the condenser aperture to eliminate the high-angle electrons from the beam. The second condenser lens forms the electrons into a thin, tight, coherent beam, while a user selectable objective aperture further eliminates high-angle electrons from the beam. To scan the beam in a grid fashion a set of coils is used. Finally the objective lens focuses the scanning beam onto the part of the specimen desired.

When the incident electron beam (primary electrons) is raster-scanned across the sample surface, the energy transferred to the focus spot dislodges electrons from the sample itself. (Figure 3.3) These secondary electrons (SE), are collected by a detector, amplified and then transformed into a signal. The SEM image is the result from the electron beam scans of the analyzed sample area.

In addition to the secondary electrons, backscattered (BSE) electrons from the specimen can be detected. Backscattered electrons are produced by the elastic interactions between the sample and the incident electron beam. These high-energy electrons can escape from much deeper than secondary electrons, so surface topography is not as accurately resolved. The efficiency of production of backscattered electrons is proportional to the sample material's mean atomic number, which results in image contrast as a function of composition, higher atomic number material appears brighter than low atomic number material.

Backscattered electron imaging provides elemental composition variation, as well as surface topographical information. Qualitative and quantitative chemical analysis information is also obtained using an energy dispersive x-ray spectrometer (EDX).

Scanning electron microscopes are often equipped with an EDX analysis system to enable the elemental analysis of the samples. During EDX Analysis, an electron beam strikes the surface of a conducting sample. The energy of the beam is typically in the range 10-20keV. The collision of the incident beam with the atoms of the sample causes an inner shell electron to be ejected. The occupation of the vacancy by a higher-energy electron from an

III. Characterization Methods

outer shell causes X-rays to be emitted from the samples. The energy of the X-rays emitted during the transferring process is specific of every element. Thus, the identity of the atom can be established. The X-rays are generated in a region about 2 microns in depth, and thus EDX is not a surface sensitive technique.

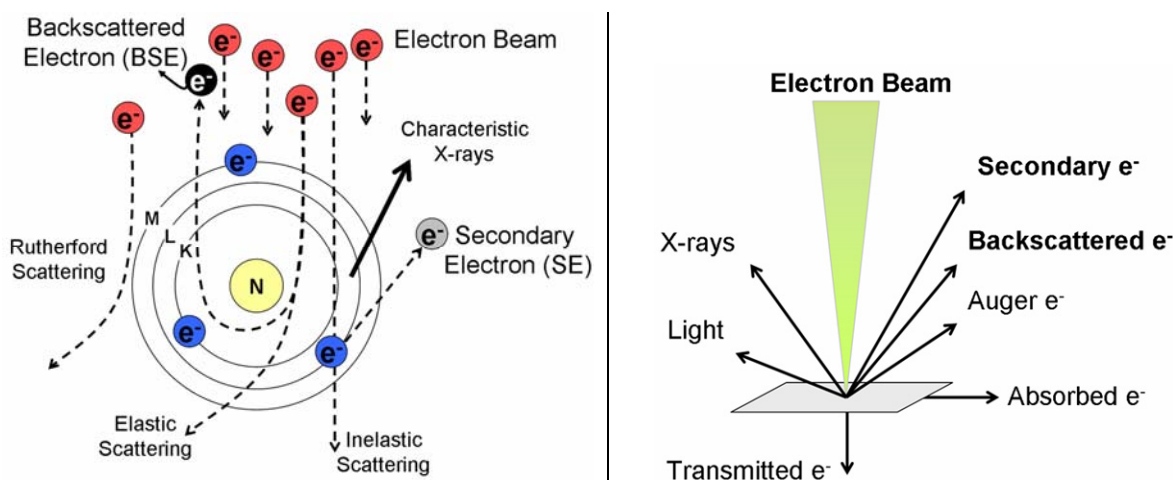


Figure 3.3. Schematic representation of the electron beam – specimen interactions occurring during a SEM measurement.

High-resolution scanning electron microscopy (HR-SEM) was employed to resolve the size and morphology of the crystals as well as to characterize the thin films. The micrographs were collected with a JEOL JSM-6500F operating at 10 kV for the bulk samples, and at 5 kV to measure the assembled films. Prior to SEM measurement, the specimens were sputtered with carbon or gold with a BAL-TEC MED 020 Modular Coating Unit.

3.3. Dynamic Light Scattering

Dynamic light scattering (DLS) is the modulation of visible light caused by the Brownian motion of particles. From the scattered light the speed of movement of particles in a liquid medium is calculated. The mobility is proportional to the diameter of the particles (the Stokes diameter).

When a beam of light passes through a colloidal dispersion, the particles scatter some of the light in all directions (Figure 3.4). When the particles are very small compared with the

III. Characterization Methods

wavelength of the light, the intensity of the scattered light is uniform in all directions (Rayleigh scattering); for larger particles (above approximately 250 nm diameter), the intensity is angle dependent (Mie scattering). If the light is coherent and monochromatic, as a laser, it is possible to observe time-dependent fluctuations in the scattered intensity using a suitable detector such as a photomultiplier capable of operating in photon counting mode. These fluctuations occur from the fact that the particles are small enough to undergo random thermal motion (Brownian motion) and the distance between them is therefore constantly varying. Constructive and destructive interference of light scattered by neighboring particles within the illuminated zone generate intensity fluctuations at the detector which, as it results from particle motion, contains information about this motion.

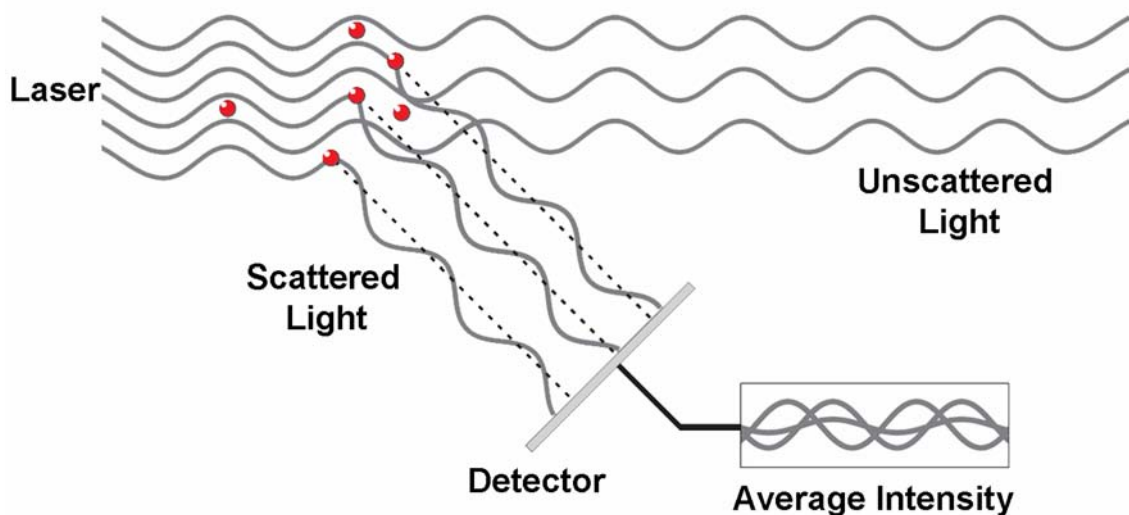


Figure 3.4. The diagram shows the propagated waves from the light scattered by the particles.

The time dependence of the intensity fluctuation is most commonly analyzed using a digital correlator. Such a device determines the intensity autocorrelation function, which describes how a given measurement relates to itself in a time dependent mode. Analysis of the time dependence of the intensity fluctuation can therefore provide the diffusion coefficient of the particles. Applying the Stokes Einstein equation and knowing the viscosity of the medium, the hydrodynamic radius or diameter of the particles can be calculated.

III. Characterization Methods

With the assumption that the particles are spherical and non-interacting, the mean radius (r) is obtained from the Stokes-Einstein equation:

$$r = \frac{k_B T}{6\pi\eta D} \quad (3.5)$$

where k_B is the Boltzmann constant ($1.3807 \cdot 10^{-23}$ J K $^{-1}$), T the temperature (K), and η the shear viscosity of the solvent (water = $8.94 \cdot 10^{-4}$ kg m $^{-1}$ s $^{-1}$).

Dynamic light scattering measurements were performed to determine the hydrodynamic particle diameter in colloidal suspensions at 25 °C on an ALV-NIBS/HPPS High Performance Particle Sizer equipped with a HeNe-laser at 632.8 nm. Data were typically collected over a delay range of 30s.

3.4. Sorption Measurements

Gas sorption is the most employed experimental method for the characterization of the surface and the pore size of porous materials. It allows assessment of the complete range of micro-, meso- and macropores. Depending on the interaction strength, adsorption processes can be classified into chemical and physical adsorption. Chemisorption involves the chemical bonding of the gas (or vapor) phase with specific sites on the surface, thus it is an irreversible phenomenon. Necessarily, only a single layer of adsorbate molecules on the surface can be formed. Physisorption, on the contrary, is a fully reversible process, which involves weak interaction of the adsorbate with the surface, such as Van der Waals interactions (London dispersion, dipole-dipole). Thus, physisorption consents the study of both the adsorption and desorption steps. The coverage of the surface through physisorption can occur by the formation of multi-layers and the consequential condensation of the adsorbate in the pores.

Sorption measurements of microporous materials are most frequently performed either by gravimetric or by volumetric methods. The former one is based on a sensitive microbalance

III. Characterization Methods

and the sorption is investigated by measuring changes in the sample weight. On the other hand, the volumetric method is based on measuring the effective gas pressure above the sample. This method is based on calibrated volumes and pressure measurements by applying the ideal gas equation of state:

$$pV = nRT \quad (3.6)$$

where p is the pressure (Pa), V is the volume (m^3), n the number of moles of the gas, R is the gas constant ($8.314 \text{ Jmol}^{-1}\text{K}^{-1}$), and T is the temperature (K). The adsorbed amount is calculated from the difference of the total amount admitted to the sample chamber with the adsorbent and the amount of gas in the free space. Prior the measurement, the void volume of the sample chamber must be precisely determined. Both volumetric and gravimetric methods allow the measurement of the adsorption under either static and “quasi-equilibrium” conditions. In a quasi-equilibrium experiment the sample is exposed to a gas flow of carrier and analyte gas. The composition of the gas flow is changed step-wise during the adsorption or the desorption process to adjust the different p/p_0 values. To reach at any time satisfactory equilibrium conditions is a crucial point for applying this method. In a typical volumetric measurement, which is performed at static conditions, different known amounts of the analyte gas are dosed stepwise to the sample chamber. Adsorption of the gas occurs at each step, and the pressure in the confined volume falls till equilibrium between the adsorbate and the remaining gas in the sample chamber is reached. The adsorbed gas volumes ($\text{cm}^3\text{g}^{-1}(\text{STP})$) are measured for every step p/p_0 (relative pressure, p_0 is defined as saturation pressure) in both adsorption and desorption processes and sorption isotherms are collected. [5]

IUPAC classifies pores as macropores for pore widths greater than 50 nm, mesopores for the pore range 2 to 50 nm, and micropores for the pores smaller than 2 nm. The sorption behavior is distinct in relation to the pore size. Whereas macropores can be considered as nearly flat surfaces, the sorption behavior in meso- and micropores is influenced by the

III. Characterization Methods

interactions between the fluid and the pore walls. Furthermore, the adsorption in mesopores depends on the attractive fluid-fluid interactions, which can lead to capillary (pore) condensation. Figure 3.5 show the IUPAC classification of adsorption isotherms. [6] In ideal cases, microporous materials exhibit type I isotherms (Figure 3.5a). The characteristic features of a type I isotherm are an initial steep increase corresponding to the progressive filling process of the micropores at relatively low relative pressure because of the narrow pore width and the high adsorption potential, as well as the long horizontal plateau reached at higher pressures, corresponding to monolayer coverage. Indeed, for microporous materials the small pore dimensions of the adsorbent limit the adsorption only to one or a few molecular layers. [5] The Langmuir model describes type I isotherms with a kinetic approach and assuming that the adsorption enthalpy is independent from the coverage. [7] This model yields the Langmuir equation, which relates the coverage, θ , with the applied gas pressure p :

$$\theta = \frac{a \cdot p / p_0}{1 + a \cdot p / p_0} \quad (3.7)$$

where (above the critical temperature of the adsorbate) p_0 is the standard pressure. Below the critical temperature p_0 is substituted with the saturation pressure. The coverage, θ , can be expressed as the ratio between the amount of gas adsorbed at the pressure p and the maximum amount corresponding to monolayer coverage. The adsorption coefficient, a , depends on the heat of adsorption, and on the temperature.

Whereas type I sorption isotherms can be described by the Langmuir equation, recently the interpretation of such isotherm for microporous materials has radically changed. According to the classical Langmuir theory, the adsorption before the plateau represents completion of the monolayer and may therefore be used for the calculation of the surface area. The alternative view is that the initial steep rise of the type I isotherm represents micropore filling (rather than surface coverage) and that the low slope of the plateau is due to multilayer adsorption on the small external area (which becomes noticeable for nano-sized particles).

III. Characterization Methods

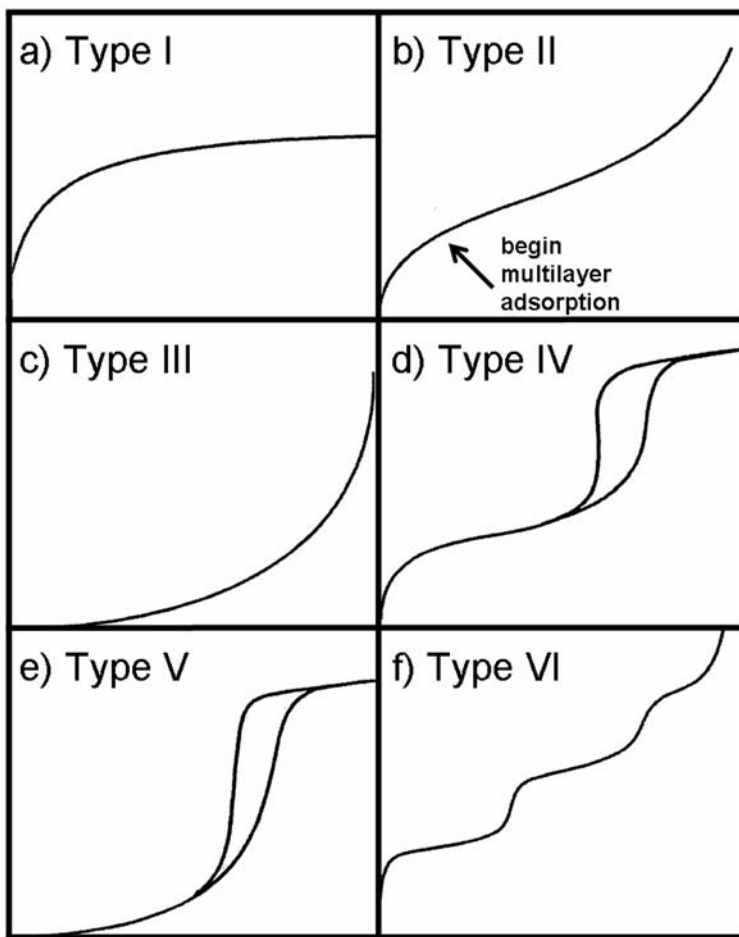


Figure 3.5. IUPAC classification of sorption isotherms. a) The isotherm classified as type I is typical of microporous material. b) Non-porous materials most often present type II isotherm where unrestricted monolayer-multilayer can occur. c) Isotherm type III indicated relatively weak adsorbate-adsorbent interactions, and important adsorbate-adsorbate interaction. d) Type IV isotherms are typical of mesoporous materials. The most characteristic feature of this isotherm type is the hysteresis loop, associated with the occurrence of pore condensation. e) Type V isotherms show pore condensation and hysteresis. f) Isotherm type VI represent stepwise multilayer adsorption on uniform non-porous surface. [6]

No current theory is capable of providing a general mathematical description of micropore filling and caution should be taken in the interpretation of derived quantities (e.g. micropore volume, apparent surface area) obtained by the application of a relatively simple equation to adsorption isotherm data over a limited range of p/p_0 and at a single temperature. A reasonably good fit over a certain range of an isotherm does not in itself provide sufficient evidence for a particular mechanism of adsorption. In order to interpret sorption isotherms measured on microporous materials various methods and theories have been developed. Basically they can be divided in classical and modern methods. The "classical methods" such as Polanyi, Dubinin-Radushkevich, [8] Stoeckli, and Horvath-

III. Characterization Methods

Kawazoe are based on macroscopic, thermodynamic assumptions. In contrast, methods like the density functional theory (DFT), or methods based on molecular simulations (Monte Carlo) provide a microscopic model as well as a better evaluation of the thermodynamic properties of the pore fluid. [5]

Another common isotherm observed in physisorption is the type II isotherm, which typically indicates the formation of multimolecular layers at higher pressures. The type II isotherm is shown in Figure 3.5b, where the inflection point signed by the arrow corresponds to completion of the first monolayer. The Brunauer-Emmett-Teller (BET) theory is an extension of the Langmuir model for multilayer adsorption, and is based on the assumption that the energy of adsorption in the second and in the higher layers is equal to the liquefaction energy of the adsorbent. [9] The BET equation is often expressed in the linear form:

$$\frac{p}{n(p_0 - p)} = \frac{1}{n_m C} + \frac{C-1}{n_m C} \cdot \frac{p}{p_0} \quad (3.8)$$

where n is the number of adsorbed molecules, n_m the monolayer capacity, p_0 is the saturation pressure and the constant C depends on the difference between adsorption energy of the first layer and the liquefaction energy of the adsorbate. Noteworthy, the BET theory is used almost universally for the calculation of the specific surface area of porous solids, because of its simplicity, definitiveness, and its ability to conform to the different isotherm types by changing the C values in the BET equation. Although this model is based on the assumption of multilayer adsorption, in the literature the BET equation is often employed to calculate the specific surface area of microporous materials. For microporous materials it is very difficult to separate the processes of mono-multilayer adsorption from micropore filling. Pore filling is typically completed at $p/p_0 \leq 0.1$, much earlier than the applicability range of relative pressure ($0.05 \leq p/p_0 \leq 0.3$) defined for the BET equation as region near to completed monolayers. Thus, the surface area values obtained for microporous materials applying the BET method should be considered as relative comparisons, reporting the range of linearity of the BET plot.

III. Characterization Methods

Bulk sorption measurements were performed on an Autosorb-1 (Quantachrome Instruments). N₂ sorption was performed at 77 K, while the isotherms for *n*-butane were collected at 273 K. Sorption isotherms of *n*-and *i*-butane, as well as water on microporous thin films, were measured employing the quartz crystal microbalance (QCM) technique.

The QCM offers an alternative technique to estimate the amount of the sorbed gas; the measurement principle relies on the high gravimetric sensitivity of the acoustic wave device. QCM detection is a powerful tool to characterize the sorption properties of porous materials as thin films. The ultrasensitive mass measurements permit the collection of sorption data of very small amounts of the porous material. A typical QCM can measure a mass change of 1-10 ng cm⁻². The QCM device employed in this thesis (XA 1600, KVG Quartz Crystal Technology) consists of a thin disk of quartz crystal AT-cut with key-hole gold electrodes patterned on both sides (Figure 3.6a). The QCM devices are characterized by a fundamental frequency of 10 MHz. When the QCM electrodes are connected to an oscillator and an AC voltage is applied, the quartz crystal starts to oscillate at its resonance frequency due to the piezoelectric effect. The mass sensitivity of the QCM originates from the relationship between the oscillation frequency and the mass loading as described by the Sauerbrey equation, as shown below.

In a typical experiment, the sorption measurements of *n*-butane (99.5 vol. %, AIR LIQUIDE) and *i*-butane (99.5 vol. %, Messer Griesheim) on the zeolite films were performed at room temperature (296 K). Prior to sorption measurements, the zeolite-coated devices were dehydrated directly in the sample chamber at 120 °C for 24 h under ultra-dry nitrogen flow (2 l min⁻¹). Reaching a stable resonance frequency value confirmed the removal of physisorbed water. The gas flow of *n*-butane or *i*-butane in nitrogen was regulated by a computer-controlled gas-flow system (MKS Instruments). Using digital mass-flow controllers and a calibrated gas-flow system it was possible to finely control the partial pressure of the analyte gas at every sorption step. Generation of different analyte-gas

III. Characterization Methods

concentrations was achieved by dilution of different analyte flow (0 – 30 ml min⁻¹) with the carrier gas flow (0 – 580 ml min⁻¹).

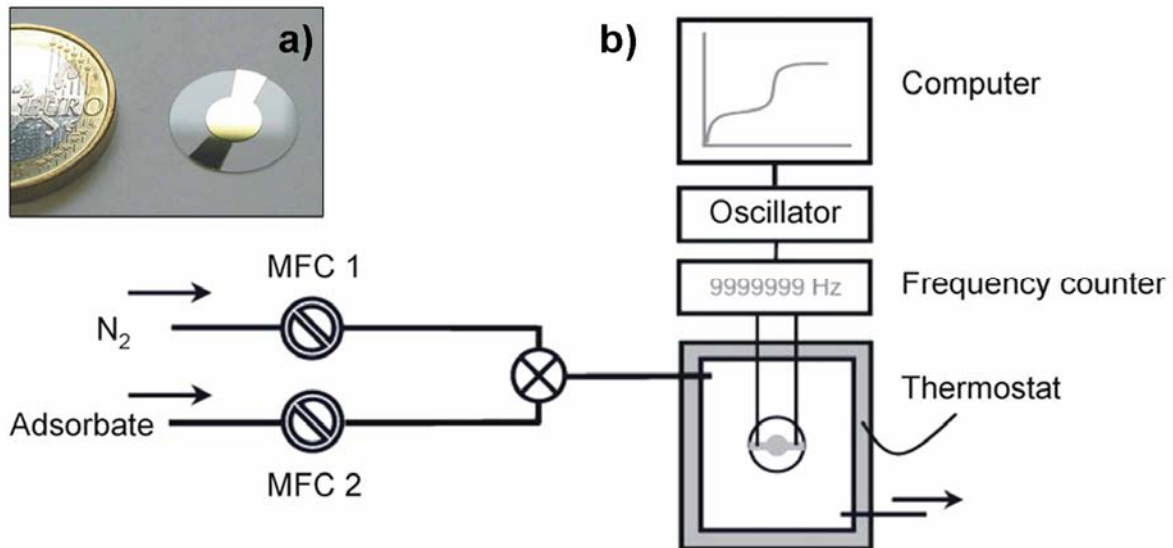


Figure 3.6. a) Quartz crystal microbalance device (XA 1600, KVG Quartz Crystal Technology). b) QCM set-up for the collection of sorption data: the carrier gas (N_2) and analyte gas flows are regulated by a computer-controlled gas-flow system. A thermostat allows temperature regulation of the sample chamber.

Analyte sorption isotherms were obtained by measuring the resonance frequency of the QCM at every adsorption/desorption step (different partial pressure of analyte gas) and recalculating the amount of the hydrocarbon adsorbed through the Sauerbrey equation [10]

$$\Delta f = -\frac{2f_0^2 \Delta m}{A \sqrt{\rho_q \mu_q}} \quad (3.9)$$

In this equation, Δf is the frequency change, f_0 is the resonant frequency of the fundamental mode of the crystal (10 MHz), A is the piezo-active area of the electrode (1 cm²), ρ_q is the density of quartz (2.648 g cm⁻³), μ_q is the shear-modulus of quartz (2.947·10¹¹ g cm⁻¹ s⁻²), and Δm the mass change (g). Thus a frequency change of 1 Hz corresponds to a mass-loading of 4.42·10⁻⁹ g onto a crystal surface of 1 cm². A schematic representation of the analytical system is presented in Figure 3.6b. A gas purifier cartridge (Alltech) was employed to ensure a water-free analyte-gas.

III. Characterization Methods

3.5. Thermogravimetric Analysis

Thermogravimetric Analyses (TGA) is a technique for measuring the weight changes in materials as a function of temperature or time, to study material composition, thermal stability, and dehydration or oxidation phenomena. The sample weight is recorded as a function of the controlled increase of the temperature. In composite materials, such as porous structures, the different components (solvent or template molecules, ligands or inorganic clusters) will be decomposed at different specific temperatures. Differential Scanning Calorimetry (DSC) is often coupled to TGA instrumentation. This technique allows understanding the nature of the decomposition phenomena (exo- or endothermic processes) occurring during a thermogravimetric analyses. The difference in heat-flow to or from a sample and to or from a reference is monitored as a function of temperature or time, during a controlled temperature program. Distinct steps in weight loss correspond to the combustion or desorption of one specific constituent and are characteristic for the decomposition process. Thus, quantitative determination of compositional changes can be obtained.

Thermogravimetric analyses (TGA) of the bulk samples of zeolites as well as MOFs were performed on a Netzsch STA 440 C TG/DSC. The measurements were performed between 23 and 900 °C in a synthetic air flow of 25 mL min⁻¹, with a heating rate of 10 °C min⁻¹.

3.6. Vibrational Spectroscopy: IR and Raman

FT-IR and FT-Raman spectroscopy can be used to investigate solid materials by excitation of the vibrational modes, involving pairs or groups of bonded atoms, to higher energy states by absorption of radiation of appropriate frequency.

IR radiation has enough energy to excite molecular vibration or rotation to higher energy levels. In order to absorb infrared radiation, a molecule must be subjected to a change in dipole moment as a consequence of its vibration or rotation.

III. Characterization Methods

In a Raman measurement, the sample is illuminated with monochromatic light, usually generated by a laser. The samples scatter the monochromatic light either elastically (Rayleigh scattering), or inelastically (Raman-scattering). Whereas IR absorption is the result of a change in the dipole moment, Raman absorption involves a change in the bond polarisability during the vibration. The latter is a two photon process. Thus, the mechanism of Raman scattering is different from that of infrared absorption, and Raman and IR spectra provide complementary information. Vibrational spectra of solid samples present a large number of peaks, each corresponding to specific vibrational transitions. Thus, IR as well as Raman techniques are suitable for identification purposes of both specific functional groups (organic molecules), as well as the local structure of the solid material.

Whereas FT-IR and Raman spectroscopy are typically employed to investigate powder samples, reflection-adsorption IR spectroscopy (RAIRS) utilizes an alternative geometry that allows examination of thin layers such as self-assembled monolayers on reflecting surfaces (metals, polished metal oxides). [11] The set-up of the reflection-absorption FT-IR experiment is shown in Figure 3.7.

IR radiation is directed onto the sample and reflected from an underlying reflective surface. The signal is modulated by the surface film where absorption of the IR radiation occurs and further reflected from the underlying surface. If the reflection layer is a noble metal, only those vibrations whose dipole moments lie perpendicular to the reflection surface can be observed. This is because the incident and reflected p-polarised components of the radiation superimpose constructively (add together), enhancing the signal, whereas the s-polarised components cancel each other out, (as they undergo a phase change on reflection from the reflection surface).

This technique was effectively applied to characterize the SAM functionalization of gold surfaces on a Bruker IFS 66v FTIR spectrometer. The sample chamber mounting a high performance variable angle reflection accessory (A-513), is maintained at 2 mbar during the entire measurement by means of an Edwards rotary-pump. In a typical measurement, an

III. Characterization Methods

incidence angle of 83° to the surface normal was used. Furthermore, a O_2 -plasma-cleaned gold slide was measured as background prior to the measurements.

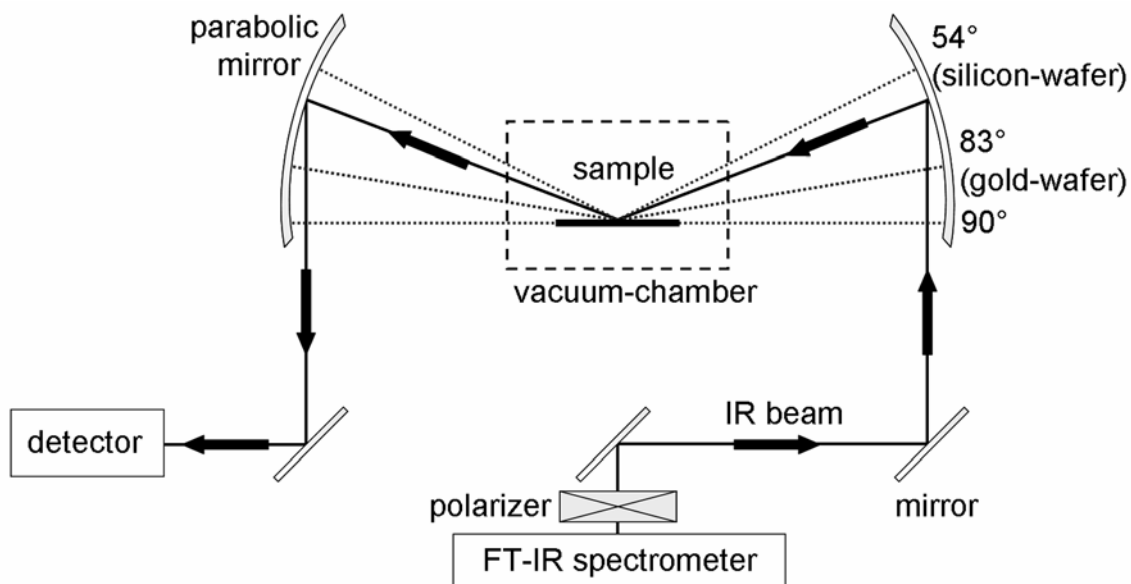


Figure 3.7. Schematic set-up of the reflection-absorption-IR spectrometer.

The infrared spectra of the zeolite powder samples were recorded in the region between 4000 and 400 cm^{-1} on an FT-IR Equinox 55 Bruker using a diffuse-reflection (DRIFFT) set-up.

The sample was diluted with KBr powder.

Raman spectroscopy of bulk samples and of thin films was performed using a LabRAM HR UV-Vis Raman Microscope (HORIBA Jobin Yvon, He-Ne Laser $\lambda = 632.81\text{ nm}$) equipped with a CCD detector (100x objective, measurement exposition time 60 s, accumulation number 2). For the measurement of metal-organic frameworks the data were collected with a laser filter D2, resulting in a laser power of about $0.1\text{ mW }\mu\text{m}^{-2}$.

3.7. Solid State Nuclear Magnetic Resonance

In solution NMR, spectra consist of a series of very sharp transitions, due to averaging of anisotropic NMR interactions by rapid random tumbling. By contrast, solid-state NMR spectra are very broad, as the full effects of anisotropic or orientation-dependent interactions are observed in the spectrum. High-resolution solution-state spectra are a result of fast isotropic molecular tumbling. In the solid state, this motion is (usually) absent,

III. Characterization Methods

and anisotropic interactions, i.e., the chemical shift anisotropy (CSA), and the dipolar and quadrupolar couplings, lead to a broadening of the resonances. These anisotropic interactions, on the one hand, have the significant disadvantage of hindering the resolution of distinct sites, but, on the other hand, contain valuable structural and dynamic information. Specifically, the CSA and quadrupolar interactions provide insight into electronic structure and bonding, while the dipolar coupling offers direct access to internuclear distances. Moreover, all three anisotropic interactions are formidable probes of dynamics. As noted above, in solution, fast isotropic tumbling of the molecules causes the averaging to zero of the line broadening due to the anisotropic interactions. To achieve high resolution NMR in the solid-state, this averaging process should be mimicked.

Rather than requiring random isotropic motion of each molecule, it has been shown that a physical rotation of the whole sample around an axis inclined at an angle of $\arctan(\sqrt{2}) = 54.7^\circ$ (referred to as the magic angle MA) to B_0 suffices to average any second-rank tensor interaction to zero. [12-14]

For solid-state NMR of a dilute spin $I = 1/2$ nucleus, such as ^{13}C or ^{29}Si , magic angle spinning (MAS) is usually combined with the method of cross polarization (CP), [15,16] whereby a sensitivity enhancement results as a consequence of the transfer of polarization from an abundant nucleus with a high magnetogyric ratio, usually ^1H . The approach is referred to as CP MAS NMR (Figure 3.8). [17]

Achieving high-resolution is not the only goal in solid-state NMR the elucidation of the structural and dynamic information inherent to the anisotropic interactions (responsible for the line broadening) is of great importance as well. Recoupling methods allow recovering the anisotropic interaction during part of the NMR experiment. In simple terms, recoupling involves the application of rf (radio frequency) pulses to counteract the effect of the physical rotation. [18,19]

III. Characterization Methods

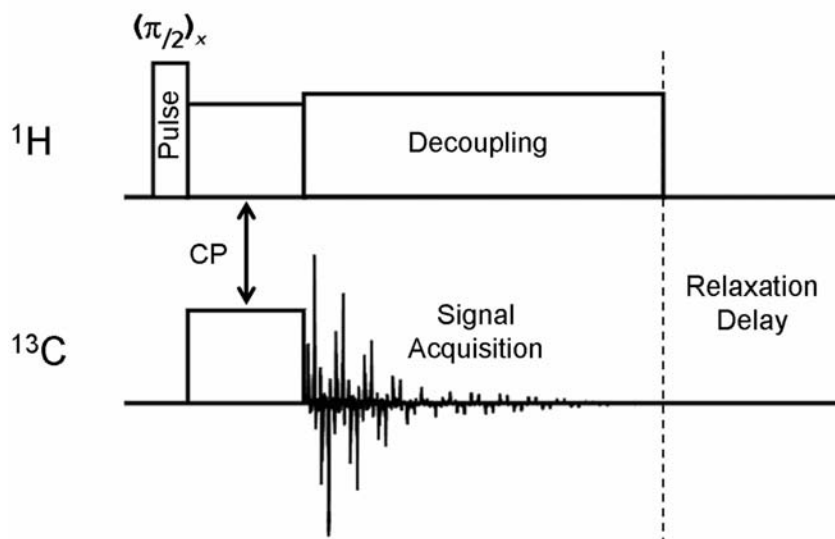


Figure 3.8. Cross polarization (CP) pulse sequence. CP can be used to enhance the signal of nuclei with a low gyromagnetic ratio (^{13}C , ^{15}N) by magnetization transfer from nuclei with a high gyromagnetic ratio (^1H). In order to establish magnetization transfer, the radiofrequency (RF) pulses applied on the two frequency channels must fulfill the Hartmann–Hahn condition.

^1H , ^{13}C , ^{29}Si MAS solid state NMR spectroscopy, both single-pulse (SP) and CP methods, were employed in this thesis as supporting characterization method for the structure determination of a new zinc(II) terephthalate (Section 4.3), as well as to confirm the surface functionalization of nano-zeolites after grafting reaction (Section 4.1). Solid state NMR measurements were performed on a DSX Avance500 FT spectrometer (Bruker) with an 11.75 T magnetic field; a 4 mm ZrO_2 rotor was used. For the ^{13}C experiments the spinning rates were 7 and 10 KHz and the pulse duration of the measurement was 3 μs . A total of 128 scans were recorded with a repetition time of 8 s.

For $^1\text{H}/^{29}\text{Si}$ CP/MAS measurements the spinning rate was 6 kHz and the pulse duration of the measurement was 2.8 μs . A total of 1024 scans were recorded with a repetition time of 1 s. The ^{29}Si SP/MAS measurements were performed at spinning rate of 9 kHz, using single pulses of 2.5 μs duration with 256 repetition rate; 256 scans were accumulated.

III. Characterization Methods

References

- [1] W. L. Bragg, Proceedings of the Cambridge Philosophical Society 17 (1912) 43.
- [2] M. T. F. v. Laue: Materiewellen und ihre Interferenzen, Akademische Verlagsgesellschaft Becker und Erler, Leipzig, 1948.
- [3] A. L. Patterson, Physical Review 56 (1939) 972.
- [4] A. L. Patterson, Physical Review 56 (1939) 978.
- [5] S. Lowell, J. E. Schields, M. A. Thomas, M. Thommes: Characterisation of porous solids and powders: surface area, pore size and density, Kluwer Academic Publisher, Dordrecht, The Netherlands, 2004.
- [6] K. S. W. Sing, D. H. Everett, R. A. W. Haul, L. Moscou, R. A. Pierotti, J. Rouquerol, T. Siemieniewska, Pure Appl. Chem. 57 (1985) 603.
- [7] I. Langmuir, J. Am. Chem. Soc. 40 (1918) 1361.
- [8] M. M. Dubinin, L. V. Radushkevich, Proc. Acad. Sci. USSR 55 (1947) 331.
- [9] S. Brunauer, P. H. Emmett, E. Teller, J. Am. Chem. Soc. 60 (1938) 309.
- [10] G. Sauerbrey, Zeitschrift fuer Physik 155 (1959) 206.
- [11] M. Trenary, Annu. Rev. Phys. Chem. 51 (2000) 381.
- [12] I. J. Lowe, Phys. Rev. Lett. 2 (1959) 285.
- [13] E. R. Andrew, A. Bradbury, R. G. Eades, Nature 182 (1958) 1659.
- [14] E. R. Andrew, L. F. Farnell, T. D. Gledhill, Phys. Rev. Lett. 19 (1967) 6.
- [15] S. R. Hartmann, E. L. Hahn, Physical Review 128 (1962) 2042.
- [16] A. Pines, M. G. Gibby, J. S. Waugh, J. Chem. Phys. 56 (1972) 1776.
- [17] J. Schaefer, E. O. Stejskal, J. Am. Chem. Soc. 98 (1976) 1031.
- [18] A. E. Bennett, R. G. Griffin, S. Vega, NMR 33 (1994) 1.
- [19] T. Gullion, J. Schaefer, Journal of Magnetic Resonance (1969-1992) 81 (1989) 196.

IV. Results and Discussion

IV. Results and Discussion

The following chapter cumulates the results obtained for the different topics explored in this thesis. The related methods for the preparation and characterization were discussed in Chapter 2 and Chapter 3. Each topic is presented and discussed in a separate section, followed by a specific conclusion. These results have been subject of the following scientific publications:

- E. Biemmi, T. Bein "Assembly of nanozeolite monolayers on the gold substrates of piezoelectric sensors"
submitted to *Langmuir* (2007) (section 4.1)

- E. Biemmi, S. Christian, N. Stock, T. Bein "High-throughput screening of synthesis parameters in the formation of the metal-organic frameworks MOF-5 and HKUST-1"
submitted to *Microporous Mesoporous Materials* (2007) (section 4.2)

- E. Biemmi, T. Bein, N. Stock "Synthesis and characterization of a new metal-organic framework structure with 2D porous system: $(H_2NEt_2)_2[Zn_3(BDC)_4] \cdot 3DEF$ "
Solid State Sciences 8 (2006) 363 (section 4.3)

- E. Biemmi, C. Scherb, T. Bein "Oriented growth of the metal-organic framework $Cu_3(BTC)_2(H_2O)_3 \cdot xH_2O$ tunable with functionalized self-assembled monolayers"
Journal of the American Chemical Society 129 (2007) 8054 (section 4.4)

- E. Biemmi, A. Darga, T. Bein "Direct growth of $Cu_3(BTC)_2(H_2O)_3 \cdot xH_2O$ thin films on modified QCM-gold electrodes – water sorption isotherms"
submitted to *Microporous Mesoporous Materials* (2007) (section 4.5)

IV. Results and Discussion

4.1. Assembly of nanozeolite monolayers on the gold substrates of piezoelectric sensors

The QCM technique employed here represents a very sensitive mass sensor offering a wide detection range that allows the measurement of mass changes associated with gas-solid as well as liquid-solid interfacial phenomena. [1-4] For sensor applications it is desirable to reduce the crystal size of the microporous materials since this leads to faster transport and equilibration. Combined with a high crystal density of the layer, a greater mass response in these sensors can thus be accomplished. To optimize the preparation of selective coatings, and to achieve a self-limiting crystalline monolayer, this chapter focuses on the “post-synthetic attachment” of nano-meter sized zeolite crystals through a molecular interface. Two different strategies are explored concerning either the modification of the gold sensing area with a selected functionality able to chemically bind the free OH-groups on the zeolite external surface; or the modification of the nano-zeolite crystals to produce a colloidal ink capable of selective reaction with the gold-electrodes of the QCM device.

4.1.1 Results and Discussion

Nanosized ZSM-5 and LTA-type zeolite crystals were prepared as stable colloidal suspensions. The dynamic light scattering data show the hydrodynamic diameter of the zeolite particles to be around 100 nm (Figure 4.1.1, inset). The morphology of the particles was investigated using scanning electron microscopy: the micrographs (Figure 4.1.1) confirmed the DLS crystal size data and showed spherically-shaped crystals.

IV. Results and Discussion

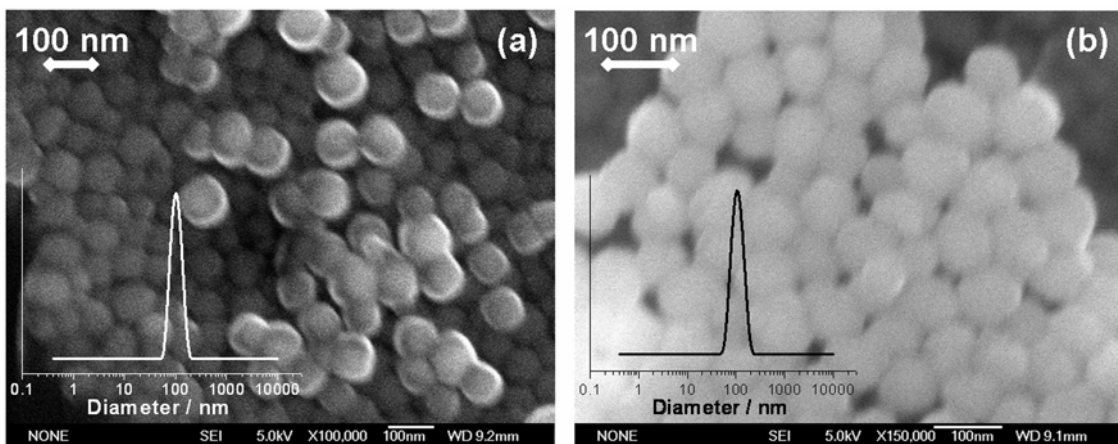


Figure 4.1.1. Scanning electron micrographs with dynamic light scattering data as inset of (a) nanocrystals of zeolite-A and (b) of ZSM-5. The DLS data of both zeolite samples present a monomodal distribution of the particles centered for LTA at 101 nm (PDI = 0.033), and at 103 nm (PDI = 0.039) for ZSM-5.

The crystalline nature of the product was examined by X-ray powder diffraction of freeze-dried powder samples (Figure 4.1.2). The diffraction patterns present all characteristic reflections of zeolite A and ZSM-5, respectively. As described (Section 2.2.1), both assembly procedures are carried out in water-free environment, therefore the re-dispersion of the dried crystals in an anhydrous organic solvent is necessary.

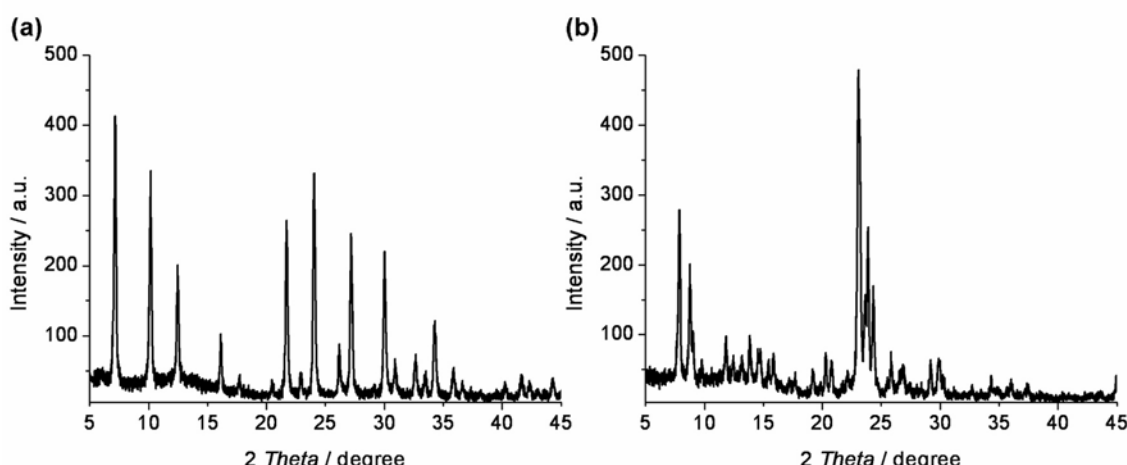


Figure 4.1.2. X-Ray diffraction patterns of nano-crystalline powder samples of (a) LTA, and of (b) ZSM-5.

The right choice of the dispersant is a key point for the formation of a high-quality assembly of the nano-zeolite crystals. In the literature, water-free toluene is largely used for grafting reactions on silica-based materials. Therefore, the re-dispersion of the nano-crystals in different organic solvents was studied by dynamic light scattering: DMF (water free) was

IV. Results and Discussion

preferred to other dispersants. Figure 4.1.3 presents the DLS data of the ZSM-5 colloidal suspension (as synthesized) compared with the re-dispersed dried powder sample in toluene and DMF, after 1 hour of ultrasonic treatment.

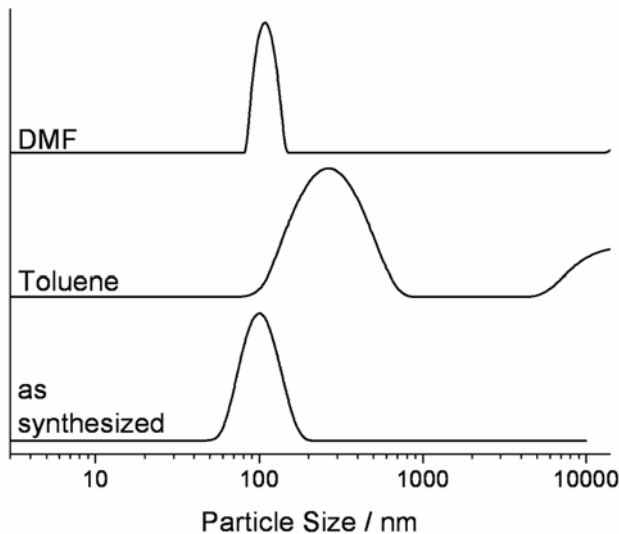


Figure 4.1.3. The dynamic light scattering measurement of a ZSM-5 colloidal suspension (as synthesized) compared with the data relative to the freeze-dried powder sample re-dispersed in toluene and in *N,N*-dimethylformamide after 1 h of ultrasonic treatment.

The complete DLS data corresponding to the re-dispersion study in different solvents (water, ethanol, acetonitrile, *N,N*-dimethylformamide, tetrahydrofuran and toluene) relative to nano-ZSM-5 sample is presented in Figure 4.1.4. Organic solvents with different polarity were chosen; water has been employed to test the possibility of re-dispersion of dried nano-zeolites back to a colloidal suspension. The particle size distribution of the sample re-dispersed in toluene shows two broad peaks at much higher particle size (0.6 and 35 μm) than the as-synthesized one, indicating agglomerated zeolite clusters. In contrast, the DMF re-dispersed sample presents a mono-sized distribution of the particles around 100 nm.

IV. Results and Discussion

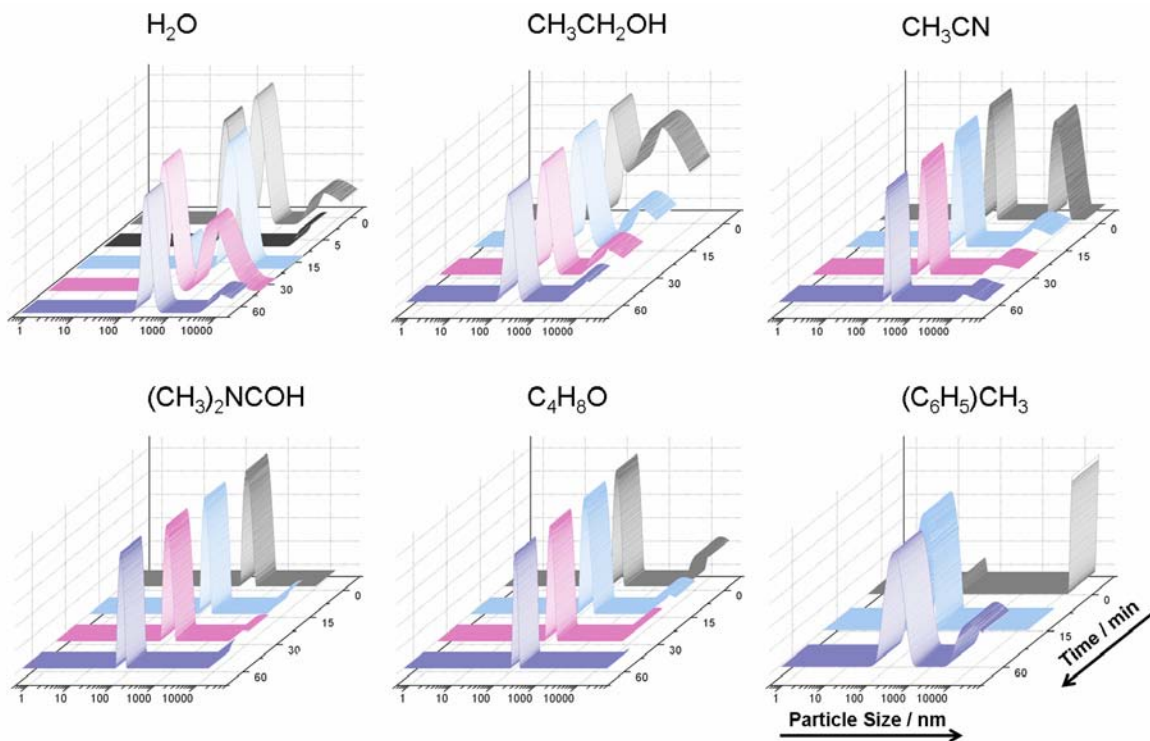


Figure 4.1.4. The dynamic light scattering measurement of a ZSM-5 freeze-dried sample re-dispersed in water, ethanol, acetonitrile, *N,N*-dimethylformamide, tetrahydrofuran and toluene after different ultrasonic treatment duration.

Raman and IR-Spectroscopy. Vibrational spectroscopy was employed to reveal the effective formation of the organic functional monolayer on the zeolite crystal surface. Complementary information was obtained by IR and Raman spectroscopy. Figures 4.1.5 show the comparison between the vibrational spectra corresponding to the nano-crystals as synthesized (a) and after the grafting step (b). The IR spectra of the LTA zeolite samples are presented in Figure 4.1.5 (top-left). The presence of the covalent linkage of the silane to the free hydroxyl-groups of the zeolite is confirmed by the appearance of the Si-C band at 1240 cm^{-1} , as well as the -CH₂ symmetric and asymmetric stretching vibrations relative to the propyl-chain of the MPS located at 2860 and 2931 cm^{-1} , respectively. The low-frequency signal at 690 cm^{-1} can be assigned to the S-C vibration. The hydrophilic character of the Linde Type A zeolite has been decreased by the presence of the organic linker on the crystals surface; thus the broad band around 3250 cm^{-1} , typical of adsorbed water molecules, is reduced as well as the related deformation band at 1650 cm^{-1} . The presence of free mercapto-groups is confirmed with Raman spectroscopy (Figure 4.1.5, bottom-left).

IV. Results and Discussion

The S-H vibrational mode at 2567 cm^{-1} can be identified in the spectra of the grafted zeolite sample.

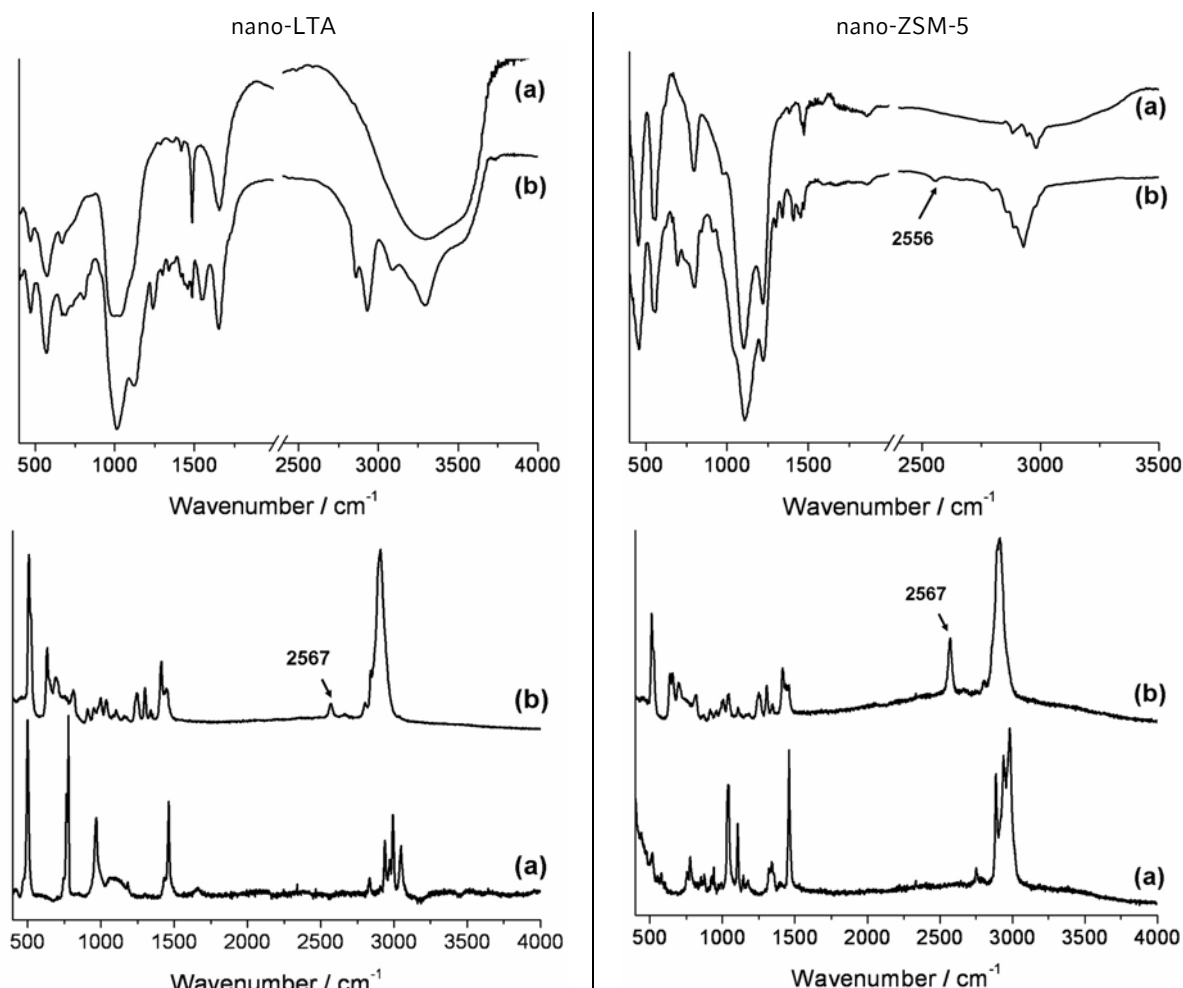


Figure 4.1.5. FT-IR (top) and Raman (bottom) spectra of bulk samples of LTA (left) and ZSM-5 (right) nano-crystals. Each graph compares the samples (a) as synthesized and (b) after grafting reaction with (3-mercaptopropyl)-trimethoxysilane.

Comparable results obtained for the nano-ZSM-5 sample. The IR spectrum of the as-synthesized sample presents the typical features of the zeolitic framework, as well as the vibrational modes related to the organic template TPA(OH). The spectrum after functionalisation presents the S-C stretching vibration at 690 cm^{-1} , and a weak band due to the -SH vibration at 2557 cm^{-1} (Figure 4.1.5, top-right). The successful grafting step was furthermore confirmed by Raman spectroscopy (Figure 4.1.5, bottom-right).

²⁹Si Solid-State NMR. The structural features in molecular sieves as well as the silicon coordination moieties can be evaluated with ²⁹Si solid-state MAS-NMR spectroscopy. [5-8]

IV. Results and Discussion

Both single-pulse/magic-angle spinning (SP/MAS) and $^1\text{H}/^{29}\text{Si}$ cross-polarization/magic-angle spinning (CP/MAS) techniques were combined to determine the species before and after the MPS grafting reaction on the zeolites. Figure 4.1.6 present the comparison between the ^{29}Si NMR spectra corresponding to both zeolite (LTA on the left, and ZSM-5 on the right) before (a) and after (b) silanisation reaction. The NMR spectra corresponding to the as-synthesized nano-crystalline zeolite A (Figure 4.1.6a left) show the presence of five different absorption signals with chemical shifts in the range of -89 to -110 ppm. These absorptions can be assigned to overlapped Q^3 and Q^4 species and are assigned to different silicon environments with a different number of aluminum neighbors (from 4 to 0) in the zeolite structure.²² The CP/MAS ^{29}Si solid-state technique was further employed to reveal the fine structures and connections between the organosilyl groups and the silanol species on the zeolitic surfaces. The ^{29}Si solid-state NMR spectra of the MPS-zeolite present new strong ^{29}Si resonances in the range of -50 to about -70 ppm which are typical for organosiloxane species T^n ($n = 0-3$). The main peak at -67 ppm can be assigned to T^3 sites, while the weaker signals at -60 and -51 ppm correspond to T^2 and T^1 , respectively. [8]

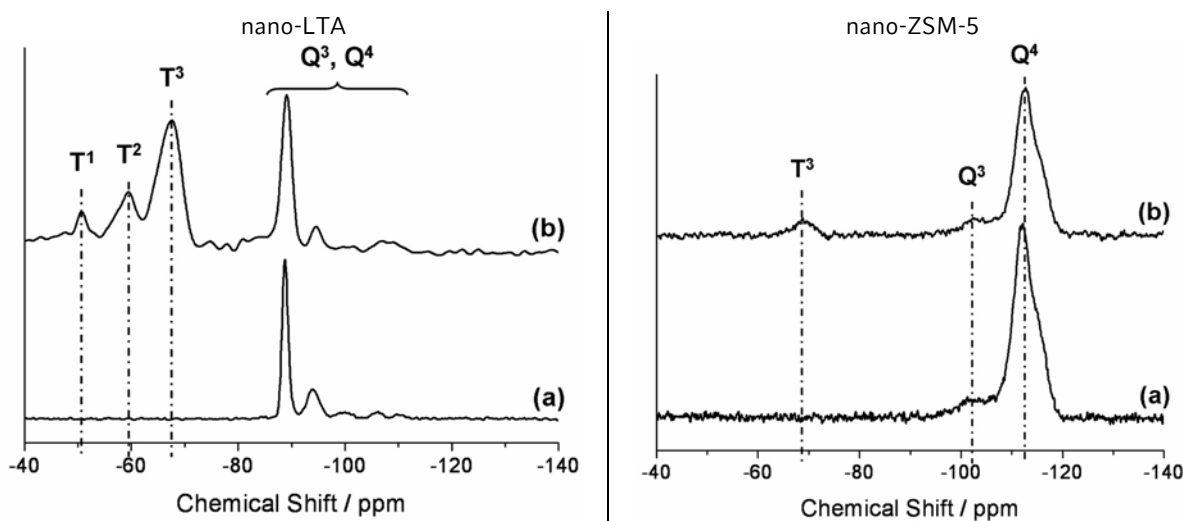


Figure 4.1.6. (left) ^{29}Si solid state NMR spectra of nano-LTA powder samples (a) as synthesized (CP-MAS) and (b) after functionalization of the crystal surface with (3-mercaptopropyl)-trimethoxysilane (SP-MAS). (right) CP-MAS ^{29}Si solid state NMR spectra of ZSM-5 zeolite nano-crystals (a) as synthesized and (b) after grafting reaction with (3-mercaptopropyl)-trimethoxysilane.

Similar observations can be made for the NMR spectra of the as-synthesized and MPS-functionalized samples of nano-ZSM-5 (Fig 4.1.6 right). Both CP-MAS ^{29}Si spectra in

IV. Results and Discussion

Figure 4.1.6 (right) show resonances around -112 to -115 ppm typical of zeolitic framework features (Q^4 sites), and a resonance at 102 ppm assigned to Q^3 species. The ^{29}Si NMR spectrum of the silane-modified zeolite (Fig 4.1.6b right) presents a signal around -69 ppm (corresponding to T^3 species) indicating the covalent linking of the mercaptosilane group to the surface of the zeolite nano-particles.

Thermogravimetric Analysis. The samples were characterized with thermogravimetric analysis to quantify the amount of organic linker present on the zeolite crystals. The TGA/DSC measurement was preformed for both zeolite structures, before and after the organic functionalisation of the crystal surface. Figure 4.1.7 (left) presents the thermogravimetric analysis of the nano-LTA samples. The mass loss due to adsorbed water takes place up to 200 °C, and decreases from 15 % to 10 % after grafting of the silane groups. This confirms the increased hydrophobicity of the crystals. The following exothermic steps from 200 to 480 °C (a) and up to 600 °C (b) are assigned to the removal of TMA and decomposition of MPS. The calculated amount of linker for this sample is about 1.6 mmol g⁻¹. This value is much higher than in the case of MFI type zeolite implying polycondensation of the (3-mercaptopropyl)-trimethoxysilane at the zeolite surface due to the presence of a comparatively high amount of adsorbed water (high Al-content zeolite). Figure 4.1.7 (right) represents the thermogravimetric data corresponding to the ZSM-5 samples. The reference measurement (a) shows a main endothermic effect in the range 360-450 °C. This is attributed to the decomposition of the structure directing agent (TPA). As expected, the measurement of the modified zeolite crystals (b) shows the expected degradation of the zeolite template and additionally, the decomposition of the organic linker up to 650 °C. The mass difference of about 5 % between the two curves corresponds to about 0.34 mmol MPS per gram zeolite.

IV. Results and Discussion

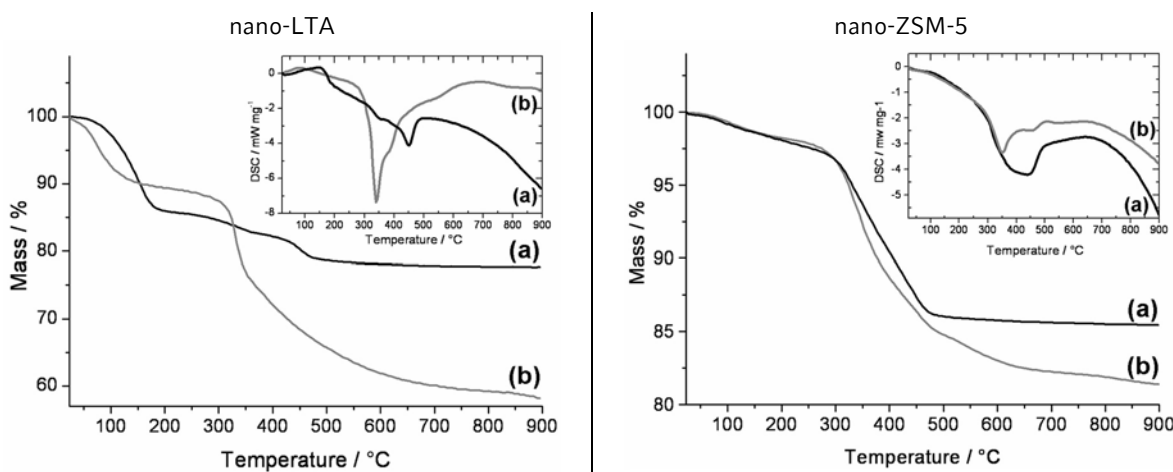


Figure 4.1.7. (left) Thermogravimetric analysis data of zeolite A samples: (a) as synthesized and (b) SH-functionalized. (right) TGA data collected on bulk samples of nano-ZSM-5. The measurement corresponding to the grafted sample (b) is compared with a reference measurement (a) of the non-treated zeolite. The corresponding DSC curves are represented in the inset.

Reflection Absorption Infrared Spectroscopy. RAIR spectroscopy was employed to confirm the formation of the 6-mercaptop-1-hexanol self-assembled monolayer on the gold surface, as well as the carbamate-linking after reaction of the alcohol-groups with 1,4-diisocyanatebutane. The two spectra of the gold substrate after formation of the OH-SAM (a), and subsequent to the isocyanate coupling (b) are compared in Figure 4.1.8. The spectrum (a) of the 6-mercaptop-1-hexanol SAM presents a broad band (centered on 3350 cm^{-1}) related to the hydroxyl groups (hydrogen-bonded). The strong absorption band at 1061 cm^{-1} is due to the stretching vibration of C-O. The low frequency of this band is an indication of hydrogen bonding. The $-\text{CH}_2-$ groups of the aliphatic chain present high-frequency modes at 2920 and 2850 cm^{-1} associated with the asymmetric and symmetric stretching vibrations, respectively. The absorptions between 1465 and 1260 cm^{-1} are attributed to the O-H and C-H deformation vibrations, while the band at 723 cm^{-1} is assigned to the stretching vibration of the S-C bond.

After reaction with the DIC-4 (spectrum b), the formation of the carbamate functionality is confirmed by the band at 1695 cm^{-1} due to the C=O stretching vibration (amide I band), as well as the combined N-H bend with a C-N stretching vibration located at 1530 cm^{-1} (amide II peak). The C-N stretch (amide III) is centered at 1260 cm^{-1} .

IV. Results and Discussion

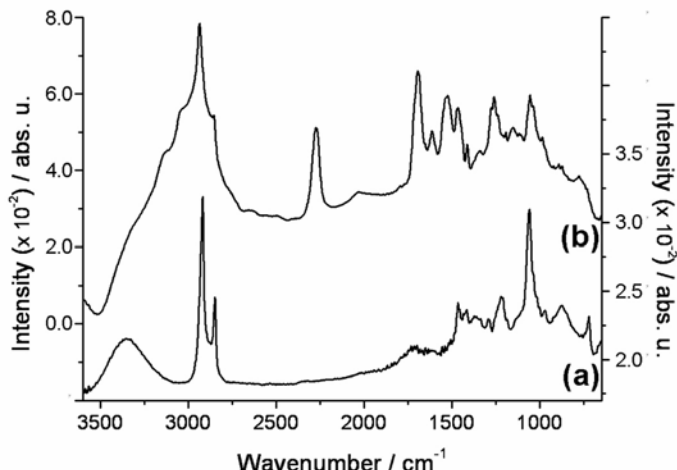


Figure 4.1.8. RAIR spectra of the self-assembled monolayers on gold (a) Au/S(CH₂)₆OH and (b) Au/S(CH₂)₆O(C=O)NH(CH₂)₄N=C=O. In the graph, the right y-axis is related to spectrum (a), while the left one belongs to graph (b).

The lowest frequency modes associated with the carbamate vibration at 1151 and 1056 cm⁻¹ are attributed to the (O=)C-O-C stretch and the C-O-C stretch, respectively. [9,10] Moreover, the existence of available isocyanate groups on the gold surface is demonstrated by the band at 2276 cm⁻¹ due to the asymmetric stretching vibration of the –N=C=O group. [11]

High-Resolution Scanning Electron Microscopy. The monolayer formation and the morphology of the zeolite film on the gold surface were confirmed by SEM. The micrographs of thin films of LTA crystals obtained with the two different assembly strategies are shown in Figure 4.1.9 (a) and (b).

A monolayer of nano-crystals is formed in both cases; the samples prepared *via* modification of the gold surface present higher coverage in comparison with the films obtained employing the SH-grafted zeolite crystals. The better quality of the films produced with the first method can be associated to the homogenous and compact structure typical of the organic SAM on gold substrate.

IV. Results and Discussion

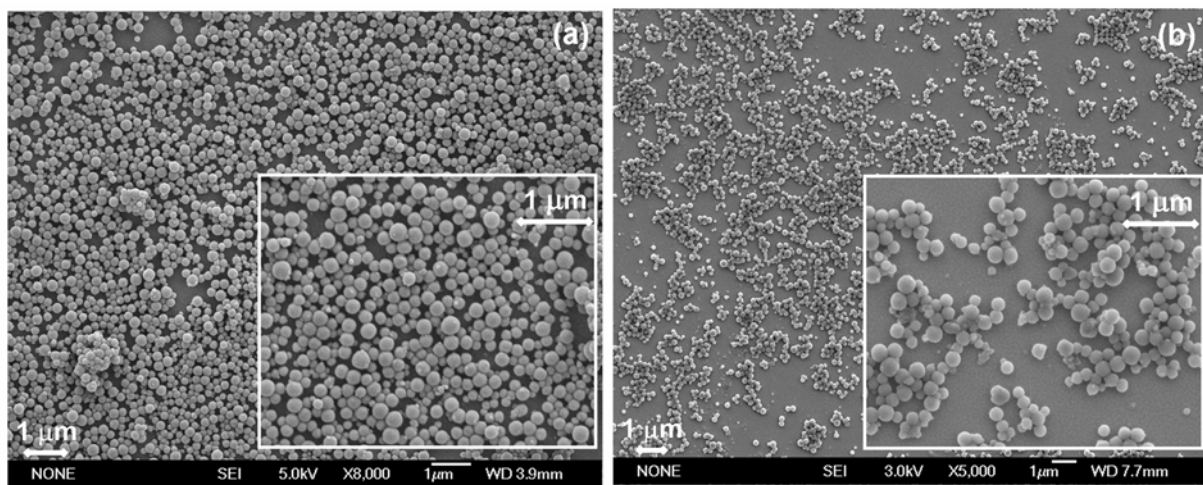


Figure 4.1.9. Scanning electron micrographs of a monolayer of LTA nano-crystals assembled on the gold electrode surface of a QCM-device. Sample prepared by (a) assembly of nano-zeolite crystals on isocyanate-modified gold substrate; and by (b) assembly of SH-functionalized nano-zeolite on bare gold surface. The samples were mildly sonicated in fresh solvent to remove the physisorbed crystals.

The thiol self-assembled monolayers offer an ideal substrate with a high density of anchoring sites where the free OH-groups on the zeolite crystals can covalently bind. The main advantage of the direct modification of the zeolites with an organic active group (*i.e.* -SH) resides in the interesting application of the functionalized zeolite crystal suspension as functional ink (pin-printing applications).

The experiments performed employing water-free toluene (as mainly reported in the literature) for the grafting reactions did not lead to satisfying results due to the difficulties in the re-dispersion step of the nano-sized crystals.

Scanning electron micrographs of “thin-films” obtained using toluene as dispersant for the dried zeolite nano-crystals are presented in Figure 4.1.10. The re-dispersion in this apolar solvent didn’t lead to mono-dispersed suspension (Figure 4.1.3) of the crystalline building blocks. Thus, the presence of agglomerated crystals on the gold surface impedes the formation of a homogeneous layer.

IV. Results and Discussion

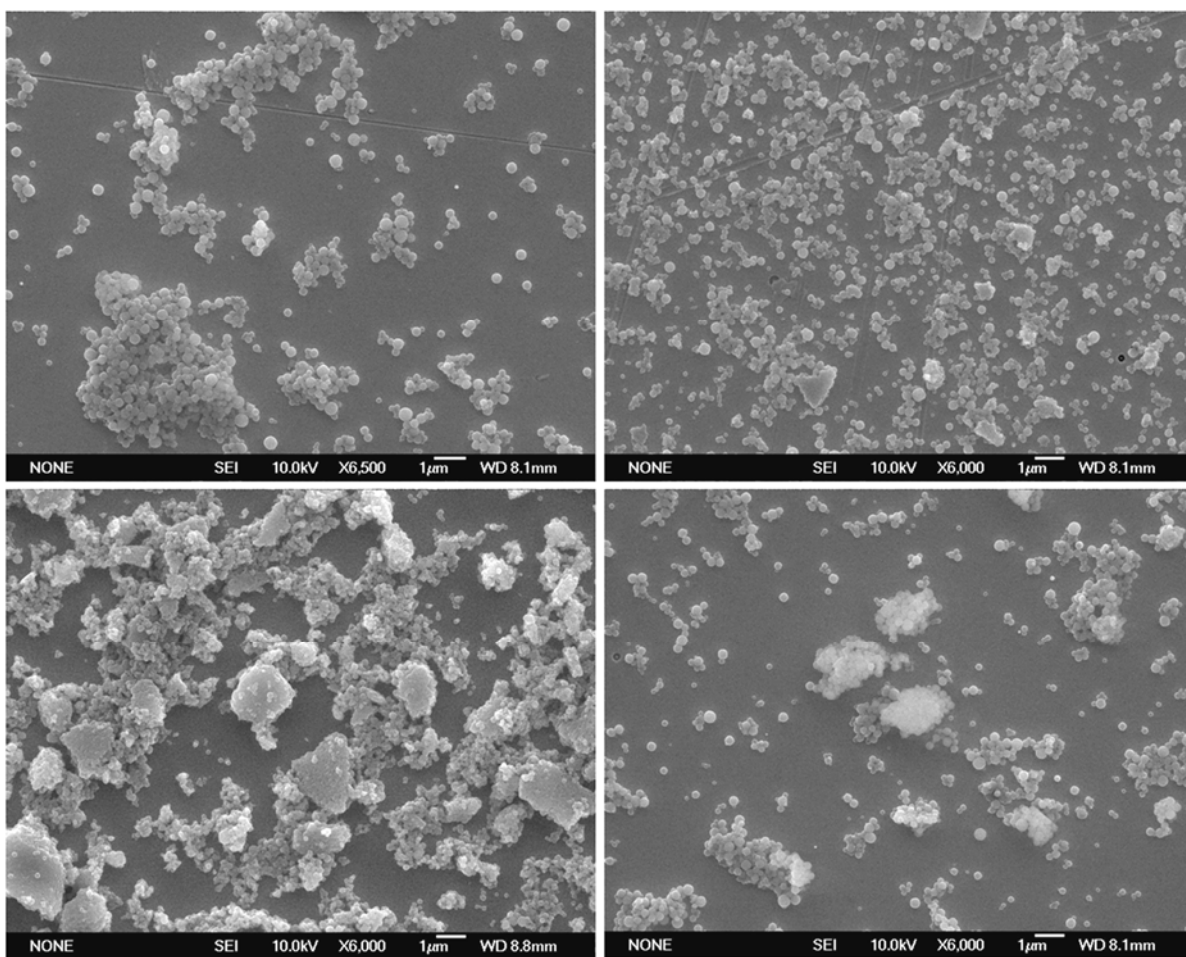


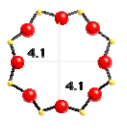
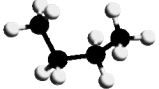
Figure 4.1.10. Scanning electron micrographs of “thin-films” obtained using toluene as dispersant for the dried zeolite nano-crystals.

QCM Sorption Measurement. The sorption isotherms of *n*- and *i*-butane at 296 K were measured based on the frequency changes of the QCM device as a function of partial pressure. The isomeric, above gases are ideal candidates to test selective sorption properties of molecular sieves. The critical diameters of *n*- and *i*-butane are 4.8 and 5.0 Å, respectively. The pore opening of the 8-member ring in the LTA framework is about 4.1 Å, while ZSM-5 presents elliptical 10-membered rings sized between 5.1 and 5.6 Å (Table 4.1.1)

The analytical system used in this work allows measuring two QCM-devices in parallel. Both zeolite films were therefore measured at the same time with one of the gases. The equilibration time for each new step (increase in the hydrocarbon concentration) was different between the two QCMs.

IV. Results and Discussion

Table 4.1.1. Comparison of the pore opening of the zeolite structures LTA and ZSM-5 with the critical diameter of the isomeric adsorbate molecules employed in the sorption measurement.

	LTA	ZSM5	n-butane	i-butane
Zeolite		 10-member rings	Adsorbate	
Pore Opening (Å)	4.1	5.1/5.5 5.3/5.6	Critical Diameter (Å)	4.8 5.0

Equilibration of *n*-butane adsorption/desorption at a certain concentration was much faster for ZSM-5 (about 3 min) than for LTA (about 10 min). Thus, the strong influence of the zeolite pore dimensions on the diffusional behavior was confirmed. For ZSM-5 there was no considerable difference in the sorption equilibration time of *n*-butane or *i*-butane. Figure 4.1.11 (right) shows the sorption isotherms of *n*- and *i*-butane in the ZSM-5 framework. Both isotherms show the typical microporous isotherm shape (Type I, IUPAC). The difference in the adsorbed amount of the two gases can be related to the lower flexibility of the spherical *i*-butane molecule in comparison with the linear and therefore more mobile *n*-butane. In contrast, the data corresponding to LTA presented in Figure 4.1.11 (left) show a substantial difference between the sorption behaviors of the two gases in the zeolitic framework. The QCM coated with zeolite A shows very slow equilibration for the sorption of *n*-butane (about 10 min) and a much faster kinetic with *i*-butane (about 2 min).

The isotherm of *n*-butane presents IUPAC type I shape which confirms sorption of the organic molecules into the pore system of the zeolite, even though the nominal pore opening of the crystalline structure is slightly smaller than the critical diameter of *n*-butane. The curve associated to the sorption of *i*-butane does not present the typical rapid rise of the adsorbed amount at low partial pressure. Thus, the sorption of the gas does not proceed through the filling of the microporous system.

IV. Results and Discussion

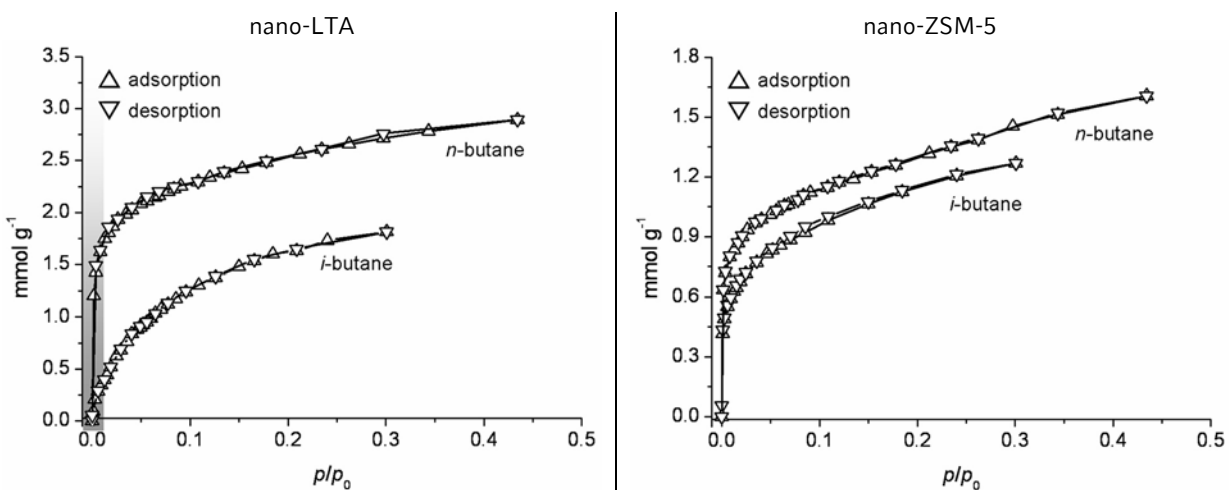


Figure 4.1.11. (left) Sorption of *i*- and *n*-butane data on nano-crystalline LTA thin film collected at 296 K. The drastically different isotherms on the framework structure illustrate the discrimination between the analyte molecules in the “sensing area” (grey bar). (right) Sorption isotherms corresponding to a thin film of assembled ZSM-5 nano-crystals. The measurements were performed at 296 K, and the data were derived from frequency changes with the QCM setup.

The increment of the adsorbed amount measured in the case of *i*-butane on LTA is assigned to interparticular free volume (textural porosity) between the nano-crystals in the compact thin film, as supported by the very fast equilibration time. The region at low partial pressure, corresponding to ppm concentration of analyte molecule, is interesting for potential sensing applications. Figure 4.1.11 (left) clearly shows that in the “sensor region” (gray bar) the dramatically different sorption behaviors of *i*- and *n*-butane in LTA allow to definitely discriminate between the isomeric probe molecules.

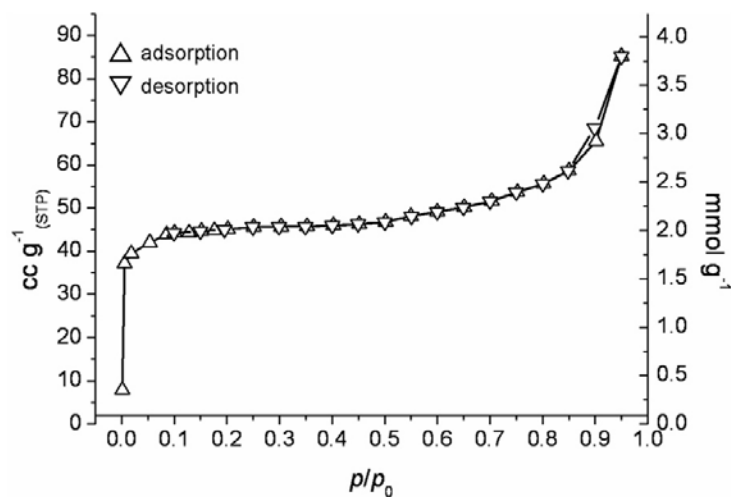


Figure 4.1.12. Sorption data of *n*-butane on a bulk sample of nano-crystalline LTA zeolite. To collect a full isotherm, the measurement was performed at 273 K on an Autosorb-1 (Quantachrome).

IV. Results and Discussion

Sorption data of *n*-butane on bulk samples of nano-LTA at 273 K were collected as reference. The obtained isotherm is presented in Figure 4.1.12.

4.1.2 Conclusion

Nanosized zeolite crystals with ZSM-5 and LTA framework structures were synthesized as stable colloidal suspensions, and were used as building blocks for the assembly of porous films on the gold electrodes of a QCM device. The preparation of the thin films was achieved either by reaction of the as-synthesized nano-crystals with isocyanate-SAM functionalized gold surface; or by assembly of SH-modified zeolite nano-particles on bare gold. Each step of the assembly strategies was fully characterized with different analytical techniques. Both procedures lead to the formation of a nano-crystal monolayer: higher coverage was obtained on the SAM-modified gold, where the ordered compact nature of the organic layer assures an ideal functional surface for the reaction with the free OH-groups of the zeolite crystal surface. The formation of a thin layer by direct functionalisation of the zeolite nano-particles, even though slightly lower coverage was achieved, is a promising result for further studies such as pin-printing applications of the zeolite crystal suspension as functional ink. Sorption isotherms of *n*- and *i*-butane were derived from frequency changes of a quartz crystal microbalance. The data collected at 296 K confirm that the response behavior of zeolite-based piezoelectric sensor depends on the framework structure as well as on size and shape of the analyte molecule. Selective sorption of *n*-butane in LTA-type structure was demonstrated, confirming the capability of producing a molecular sensor able to recognize and discriminate molecules within 1 Å.

IV. Results and Discussion

4.2. Screening of synthesis parameters in the formation of metal-organic frameworks employing conventional and HT-methods

The synthesis of MOFs proceeds mainly under solvothermal conditions. The common characteristic of these systems is their complex phase space, where small changes in compositional or process parameters (reaction temperature, reaction time, metal-salt, solvent, or pH value of the reaction solution) can have a profound impact on the structures formed and their properties. Whereas in the synthesis of the industrial important microporous materials such as zeolites the role of compositional as well as process parameters is well understood [12,13]. Systematic investigations of inorganic-organic hybrid compounds are still rare [14,15]. In this context, high-throughput (HT) methods applied to material science allow an accelerated, systematic investigation of the reaction parameter space while consuming only a minimum amount of reagents [16-18]. In this section the systematic screening of reaction parameters of two MOFs, $Zn_4O[(OOC)_2\cdot C_6H_4]_3$ (MOF-5) [19] and $(Cu_3[(OOC)_3C_6H_3]_2(H_2O)_3\cdot xH_2O)$ (HKUST-1) [20] employing HT as well as conventional methods is reported.

4.2.1. Results and Discussion

4.2.1.1. Synthesis Parameter Screening in the formation of MOF-5

The 24 reactor autoclave described above was used to study the influence of different synthesis parameters on the morphology and phase purity of MOF-5. Thus, two HT experiments were setup. The molar ratios and the exact amounts of starting materials for the reported HT-experiments are given in the following tables. For each HT experiment, in one reference cavity, the reaction mixture for MOF-5 according to the literature [19] but scaled down to the capacity of our microreactors was placed for comparison (31.8 mg (0.107 mmol) of $Zn(NO_3)_2\cdot 6H_2O$, 9.0 mg (0.054 mmol) H_2BDC , 1 ml DEF).

IV. Results and Discussion

Influence of Metal Salts and Cosolvents in MOF-5 Synthesis. In the first HT experiment, the influence of the Zn²⁺-source and the presence of cosolvents on the final product was investigated. Therefore, in the reaction mixture described above, Zn(NO₃)₂·6H₂O was substituted by ZnO, Zn(CH₃COO)₂·2H₂O,, ZnCl₂ and ZnSO₄·7H₂O (Table 4.2.1). These reactions were all repeated for reproducibility tests. In order to screen the influence of the cosolvents mesitylene, toluene and chlorobenzene on the synthesis of MOF-5, mixtures with a varying volume ratio DEF/cosolvent (Table 4.2.1) were realized. Zinc nitrate as well as zinc oxide were used as Zn²⁺-source. After stirring the mixture s the sealed multiclave was heated at 383 K for 48 h.

Table 4.2.1. Compositions of the reaction mixtures for the study the effect of different zinc(II) salts as well as the influence of cosolvents on the formation of MOF-5. The synthesis was performed under solvothermal condition at 383 K for 48 h.

Reactor Number	Zn(II) (mmol)	Zinc Salt	BDC [21]	DEF (ml)	Mesitylene (ml)	Toluene (ml)	Chlorobenzene (ml)
1	0.105	Zn(NO ₃) ₂ ·6H ₂ O	0.04	1			
2	0.105	ZnO	0.04	1			
3	0.105	Zn(OAc) ₂ ·2H ₂ O	0.04	1			
4	0.105	ZnCl ₂	0.04	1			
5	0.105	ZnSO ₄ ·7H ₂ O	0.04	1			
6	0.105	Zn(NO ₃) ₂ ·6H ₂ O	0.04	1			
7	0.105	ZnO	0.04	1			
8	0.105	Zn(OAc) ₂ ·2H ₂ O	0.04	1			
9	0.105	ZnCl ₂	0.04	1			
10	0.105	ZnSO ₄ ·7H ₂ O	0.04	1			
11	0.105	Zn(NO ₃) ₂ ·6H ₂ O	0.04	1			
12	0.105	"	0.04	0.8	0.2		
13	0.105	"	0.04	0.6	0.4		
14	0.105	"	0.04	0.4	0.6		
15	0.105	"	0.04	0.2	0.8		
16	0.105	ZnO	0.04	0.8	0.2		
17	0.105	"	0.04	0.6	0.4		
18	0.105	"	0.04	0.4	0.6		
19	0.105	"	0.04	0.2	0.8		
20	0.105	Zn(NO ₃) ₂ ·6H ₂ O	0.04	0.5		0.5	
21	0.105	ZnO	0.04	0.5		0.5	
22	0.105	Zn(NO ₃) ₂ ·6H ₂ O	0.04	0.5			0.5
23	0.105	ZnO	0.04	0.5			0.5
24	0.105	Zn(NO ₃) ₂ ·6H ₂ O	0.04	1			

Understanding the susceptibility of the products formed on the choice of reagents is of great industrial interest. A BASF-patent (DE10111230) for the synthesis of metal-organic frameworks such as MOF-5 proposing the use of different zinc(II) salts and diverse aromatic cosolvents was of inspiration to systematically study the influence of these crucial reaction

IV. Results and Discussion

parameters. The synthesis of MOF-5 was achieved by employing $\text{Zn}(\text{NO}_3)_2 \cdot 6\text{H}_2\text{O}$, $\text{Zn}(\text{CH}_3\text{COO})_2 \cdot 2\text{H}_2\text{O}$ as well as ZnO . The related XRD patterns are presented in Figure 4.2.1; traces of unreacted ZnO could be confirmed from the diffraction patterns (Figure 4.2.1b). The reaction mixtures with $\text{ZnSO}_4 \cdot 7\text{H}_2\text{O}$ led to an unknown compound (Figure 4.2.1d), while no product was formed when starting from ZnCl_2 .

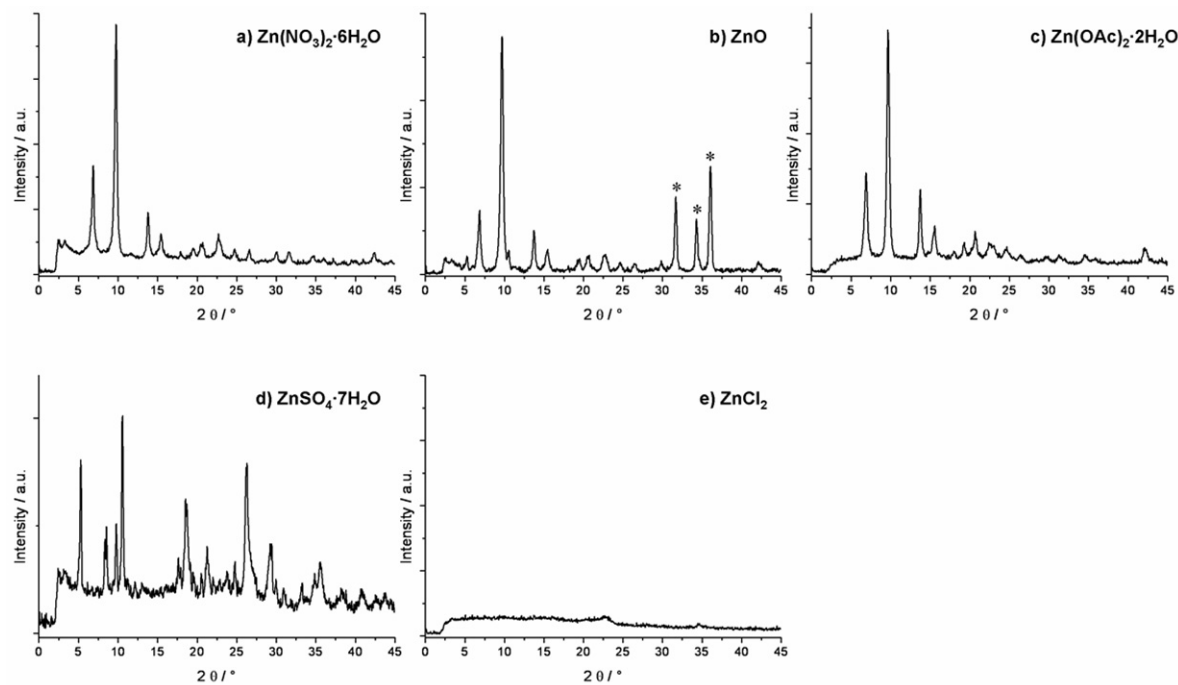


Figure 4.2.1. X-ray diffraction patterns of the reaction products obtained employing different Zn(II) salts. The metal-organic framework MOF-5 was obtained using $\text{Zn}(\text{NO}_3)_2 \cdot 6\text{H}_2\text{O}$ (a), ZnO (b) and $\text{Zn}(\text{CH}_3\text{COO})_2 \cdot 2\text{H}_2\text{O}$ (c) as confirmed by comparison with the theoretical diffraction pattern. The reflections marked with an asterisk in pattern (b) are due to the unreacted ZnO .

Figure 4.2.2 shows the scanning electron micrographs of MOF-5 material obtained when using zinc(II)-nitrate, -oxide and -acetate as Zn^{2+} -salts. Although the formation of the MOF-5 structure is achieved in each reaction mixture, the morphology of the crystalline product is strongly influenced by the zinc source. Employing $\text{Zn}(\text{NO}_3)_2 \cdot 6\text{H}_2\text{O}$ as well as ZnO leads to strongly intergrown big crystals; while in the case of $\text{Zn}(\text{CH}_3\text{COO})_2 \cdot 2\text{H}_2\text{O}$ smaller crystals with well shaped cubic morphology are formed. This might be due to a higher nucleation rate when starting from zinc acetate; resulting from the higher basicity in comparison with zinc nitrate, and better solubility of the zinc source in comparison to the oxide.

IV. Results and Discussion

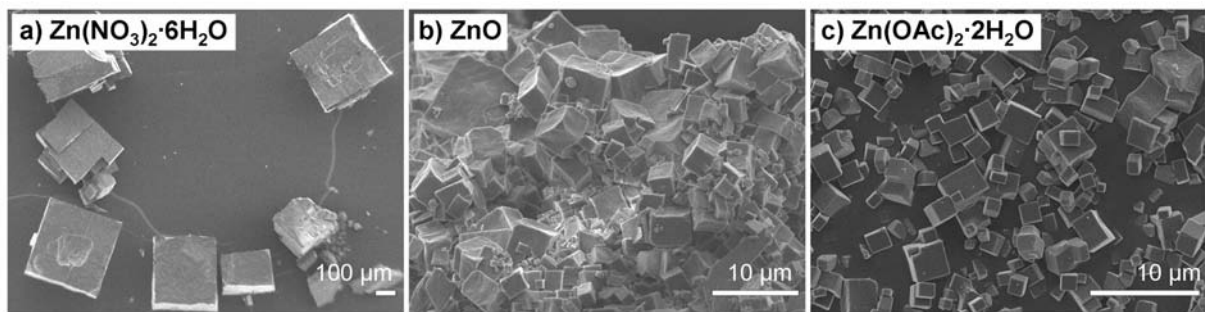


Figure 4.2.2. Influence of different zinc(II) salts on the morphology of MOF-5. The samples were synthesized at 373 K, under solvothermal conditions for 24 h. The scale bar corresponds to 100 μm for (a) and to 10 μm for (b) and (c) respectively. The diagram shows the propagated waves from the light scattered by the particles.

The influence of aromatic cosolvents is summarized in Table 4.2.2. When starting from $\text{Zn}(\text{NO}_3)_2 \cdot 6\text{H}_2\text{O}$, MOF-5 is formed for DEF/mesitylene volume ratios up to 3/2. A higher concentration of the cosolvent led to unknown phases. In contrast, the formation of MOF-5 takes place for all DEF/mesitylene ratios when starting from ZnO . However, the resulting reaction products contain large amounts of unreacted ZnO . Additionally, for the volume ratio DEF/mesitylene of 1/4, an unidentified by-product is observed. The Bragg reflections of this by-product match with the powder pattern of the unknown phase obtained when starting from the same solvents composition and zinc nitrate. Comparable results were obtained for the samples prepared with toluene or chlorobenzene as cosolvents.

Table 4.2.2. Formation of MOF-5 in the presence of cosolvents. The symbols used in the table indicate respectively: (✓) MOF-5; (✗) Unknown Phase; (*) Unreacted ZnO .

Zn(II) salt	Volume Ratio						
	DEF/Mesitylene					DEF/Toluene	DEF/Chlorobenzene
	1/0	3/2	1/1	2/3	1/4	1/1	1/1
$\text{Zn}(\text{NO}_3)_2 \cdot 6\text{H}_2\text{O}$	✓	✓	✗	✗	✗	✗	✗
ZnO	✓*	✓*	✓*	✓*	✓*✗	✓*	✓*

Both the choice of the zinc salt and the amount of cosolvent added to the synthesis mixture can influence the product formation. Thus, when starting from zinc nitrate, reaction mixtures with a high content of mesitylene, and therefore less polar reaction system, do not lead to the formation of MOF-5. Noteworthy, the formation of MOF-5 appears to be less sensitive to changes in the synthesis condition when using ZnO as reagent.

IV. Results and Discussion

Influence of OH⁻ and H₃O⁺ Addition on MOF-5 Synthesis. To understand the influence of the addition of OH⁻ or H₃O⁺ to the synthesis mixture on the structure formation, the system Zn(NO₃)₂ · 6H₂O / DEF was investigated employing high-throughput methods. The adapted literature synthesis mixture for MOF-5 described above was used and a volume of 50 µl of different aqueous solutions with a pH value between 1 and 13 was added to each mixture (with pH steps of 0.5). The alkaline and the acidic aqueous solutions were prepared by successive dilution of 1 M NaOH, and 1 M HNO₃, respectively. The reaction mixtures were stirred for 10 min using small stirring bars; the multiclave was then placed in a preheated oven at 383 K for 48 h.

The resulting sample library was characterized by X-ray powder diffraction. The presence of MOF-5 was not observed in any reaction product; indicating the high sensitivity of the formation of MOF-5 even to small amounts of water as recently described. [22]

The evaluation of the HT experiment leads to the identification of a clear reaction trend in reactivity. Thus, under more basic conditions the zinc terephthalate Zn₃(OH)₂(BDC)₂ · 2DEF [23] was obtained; while the addition of small amounts of nitric acid to the synthesis mixture led to the zinc terephthalate (H₂N_{Et})₂[Zn₃(BDC)₄] · 3DEF [24] (Figure 4.2.3). The Zn₃(OH)₂(BDC)₂ · 2DEF structure is based on infinite chains of ZnO₂(OH)₂ tetrahedral corner-sharing with ZnO₄(OH)₂ octahedra interconnected by BDC units. Thus, a 3D framework with channels running along the *c*-axis is formed. The network formed under more acidic conditions consists of trimetallic zinc units interconnected by BDC groups to form dense layers in the *b,c*-plane. The planes are pillared along the *a*-direction by BDC to form a 2D porous framework. A detailed description of the structure is presented in Section 4.3.

The framework Zn₃(OH)₂(BDC)₂ · 2DEF was only obtained as pure phase by addition of solutions of pH 9, 9.5, and 10. Upon addition of solutions with higher pH, the presence of an unknown byproduct was observed. The reaction products resulting from reaction mixtures with added acidic aqueous solution are dominated by the presence of the zinc

IV. Results and Discussion

terephthalate ($(H_2N\text{Et}_2)_2[\text{Zn}_3(\text{BDC})_4]\cdot 3\text{DEF}$). Upon addition of less acidic solutions, the formation of byproducts ($\text{Zn}_3(\text{OH})_2(\text{BDC})_2\cdot 2\text{DEF}$ and an unknown phase) increases.

In summary, the formation of MOF-5 is very sensitive to the presence of water. In the presence hydroxide, the formation of $\text{Zn}_3(\text{OH})_2(\text{BDC})_2\cdot 2\text{DEF}$ is favored. [22] Interestingly, the addition of an acid leads to the hydrolysis of DEF and the resulting $(H_2\text{N}\text{Et}_2)^+$ probably acts as template for the $(H_2\text{N}\text{Et}_2)_2[\text{Zn}_3(\text{BDC})_4]\cdot 3\text{DEF}$ due to hydrogen bonding interactions with the framework.

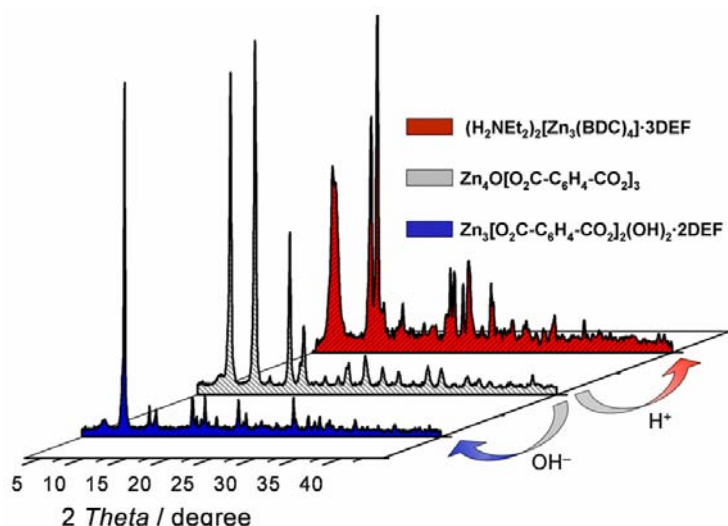


Figure 4.2.3. Reaction trends upon addition of acid or base to a typical reaction mixture of MOF-5 (gray). $\text{Zn}_3(\text{OH})_2(\text{BDC})_2\cdot 2\text{DEF}$ [23] (blue) and $(H_2\text{N}\text{Et}_2)_2[\text{Zn}_3(\text{BDC})_4]\cdot 3\text{DEF}$ [24] (red) were obtained under basic and acidic condition respectively.

4.2.1.2. Synthesis Parameter Screening in the formation of HKUST-1

The synthesis mixture for HKUST-1 as described in the literature [20] was scaled down to a total volume of liquids of 2 ml (69.78 mg (0.03 mmol) $\text{Cu}(\text{NO}_3)_2\cdot 2.5\text{H}_2\text{O}$ and 35.7 mg (0.17 mmol) of H_3BTC , and 2 ml of a 1:1 mixture of absolute ethanol and doubly distilled water (Millipore)).

Influence of Metal Salt on HKUST-1 Synthesis. The influence of different copper(II) salts and salt mixtures on the formation of HKUST-1 was investigated in a second HT experiment. Thus, 12 different molar ratios $\text{Cu}(\text{NO}_3)_2\cdot 2.5\text{H}_2\text{O}/\text{Cu}(\text{OAc})_2\cdot \text{H}_2\text{O}$, six different molar ratios $\text{CuCl}_2\cdot 2\text{H}_2\text{O}/\text{Cu}(\text{OAc})_2\cdot \text{H}_2\text{O}$, and six different molar ratios $\text{Cu}(\text{NO}_3)_2\cdot 2.5\text{H}_2\text{O}$

IV. Results and Discussion

/Na(OAc)·2H₂O were investigated in this study. Na(CH₃COO)·3H₂O was used for tuning the pH of the starting mixtures. The total amount of Cu²⁺ in each reaction mixtures was kept constant at 0.3 mmol. The detailed composition of the different reaction mixtures is reported in Table 4.2.3.

Table 4.2.3. Molar compositions for the HT study of the influence of the copper(II) salt on the formation of HKUST-1. To prepare the synthesis mixture, 2 ml of a 1:1 mixture of EtOH and H₂O was added to each reactor. The synthesis was performed under solvothermal conditions at 458 as well as 348 K for 20 h.

Reactor Number	Cu(OAc) ₂ ·1H ₂ O (mmol)	Cu(NO ₃) ₂ ·2.5H ₂ O (mmol)	BTC (mmol)
1	0.00	0.30	0.17
2	0.03	0.27	0.17
3	0.06	0.24	0.17
4	0.09	0.21	0.17
5	0.12	0.18	0.17
6	0.15	0.15	0.17
7	0.18	0.12	0.17
8	0.21	0.09	0.17
9	0.24	0.06	0.17
10	0.27	0.03	0.17
11	0.28	0.02	0.17
12	0.30	0.00	0.17
	Cu(OAc) ₂ ·1H ₂ O (mmol)	CuCl ₂ ·2H ₂ O (mmol)	BTC (mmol)
13	0.00	0.30	0.17
14	0.06	0.24	0.17
15	0.12	0.18	0.17
16	0.18	0.12	0.17
17	0.24	0.06	0.17
18	0.27	0.03	0.17
	Cu(NO ₃) ₂ ·2.5H ₂ O (mmol)	NaOAc·3H ₂ O (mmol)	BTC (mmol)
19	0.30	0.6	0.17
20	0.30	0.5	0.17
21	0.30	0.4	0.17
22	0.30	0.3	0.17
23	0.30	0.2	0.17
24	0.30	0.1	0.17

Table 4.2.4. Formation of HKUST-1 under solvothermal conditions at 348 as well as 423 K, starting from different copper(II) salts. The symbols used in the table indicate respectively: (✓) HKUST-1; (x) Unknown Phase I; (y) Unknown Phase II; (*) Cu₂O.

Cu(II) Salt and Salt Mixtures	Solvothermal Synthesis	
	348 K	423 K
Cu(NO ₃) ₂ ·2.5H ₂ O	✓	✓ *
Cu(CH ₃ COO) ₂ ·H ₂ O	✓	✓ * x
CuCl ₂ ·2H ₂ O	no product	no product
Cu(CH ₃ COO) ₂ ·H ₂ O / CuCl ₂ ·2H ₂ O	✓	✓ y
Cu(NO ₃) ₂ ·2.5H ₂ O / Na(CH ₃ COO)·3H ₂ O	✓	✓ x

IV. Results and Discussion

The diffraction patterns corresponding to the reaction mixture based on different molar ratios $\text{Cu}(\text{NO}_3)_2 \cdot 2.5\text{H}_2\text{O}/\text{Cu}(\text{OAc})_2 \cdot \text{H}_2\text{O}$ show the formation of HKUST-1 for each composition. Analogous results were obtained for the addition of $\text{Na}(\text{OAc})$ as co-salt to the typical mixtures containing $\text{Cu}(\text{NO}_3)_2 \cdot 2.5\text{H}_2\text{O}$. For both systems the increase of the content of the acetate counter-ions, leads to the formation of an unknown byproduct. A possible explanation is the increase of the pH due to the hydrolysis reaction of the CH_3COO^- ions. Looking at the morphology, the octahedral shape of the HKUST-1 phase becomes less defined with increasing $\text{Cu}(\text{OAc})_2 \cdot \text{H}_2\text{O}$ content, as shown by the scanning electron micrographs of Figure 4.2.4.

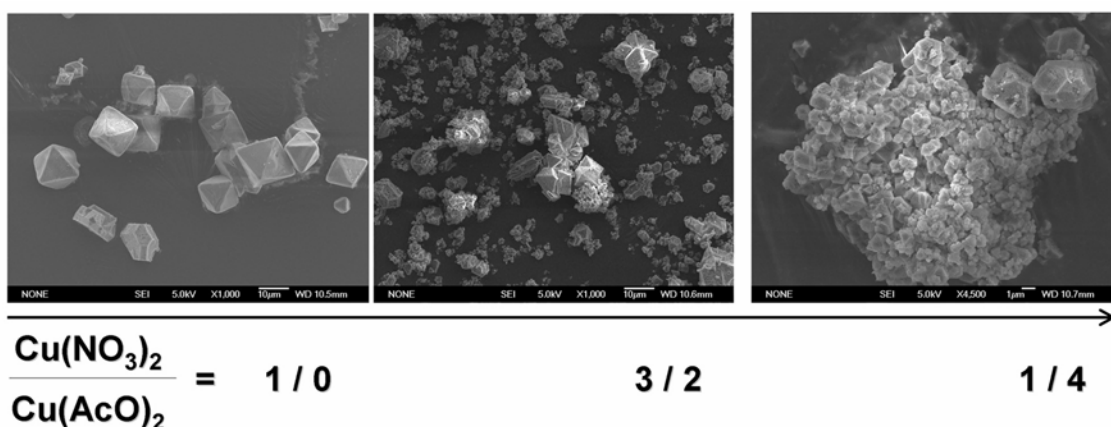


Figure 4.2.4. Morphology of the HKUST-1 crystals obtained at different molar ratio of copper(II) nitrate and acetate. With the increase of the metal acetate concentration smaller and less defined octahedral shaped crystals are formed.

When starting exclusively from copper(II) chloride no solid reaction product could be detected. The diffraction patterns of the product obtained from the syntheses combining $\text{CuCl}_2 \cdot 2\text{H}_2\text{O}$ and $\text{Cu}(\text{OAc})_2 \cdot \text{H}_2\text{O}$ show the formation of HKUST-1 as well as an unknown byproduct. With an increasing molar ratio $\text{Cu}(\text{OAc})_2 \cdot \text{H}_2\text{O}/\text{CuCl}_2 \cdot 2\text{H}_2\text{O}$ in the starting mixture less byproduct is observed. Interestingly, only pure phase HKUST-1 is formed when the same experiments are carried out at 348 K.

Influence of Temperature and Time on the Synthesis of HKUST-1. The typical synthesis procedure for the synthesis of HKUST-1 described in the literature proceeds under

IV. Results and Discussion

solvothermal conditions at 453 K. [20] However, at these conditions a significant amount of Cu₂O is obtained as by-product. [25] For many applications, such as catalysis, the purity of the product is a fundamental criterion. The influence of the synthesis temperature at 453, 423, 393, and 348 K was therefore studied. The solvothermal syntheses were performed in conventional autoclaves (Parr Instrument) with a maximum internal volume of 25 ml. In a typical reaction mixture 0.427 g (1.8 mmol) of Cu(NO₃)₂·2.5 H₂O were dissolved in 6 ml doubly distilled water and mixed with an ethanolic solution (6 ml abs. EtOH) of trimesic acid (0.221 g - 1.0 mmol). The XRD patterns of the reaction products obtained from synthesis mixtures in conventional reactors at different temperatures (348, 393, 423 and 453 K) are shown in Figure 4.2.5.

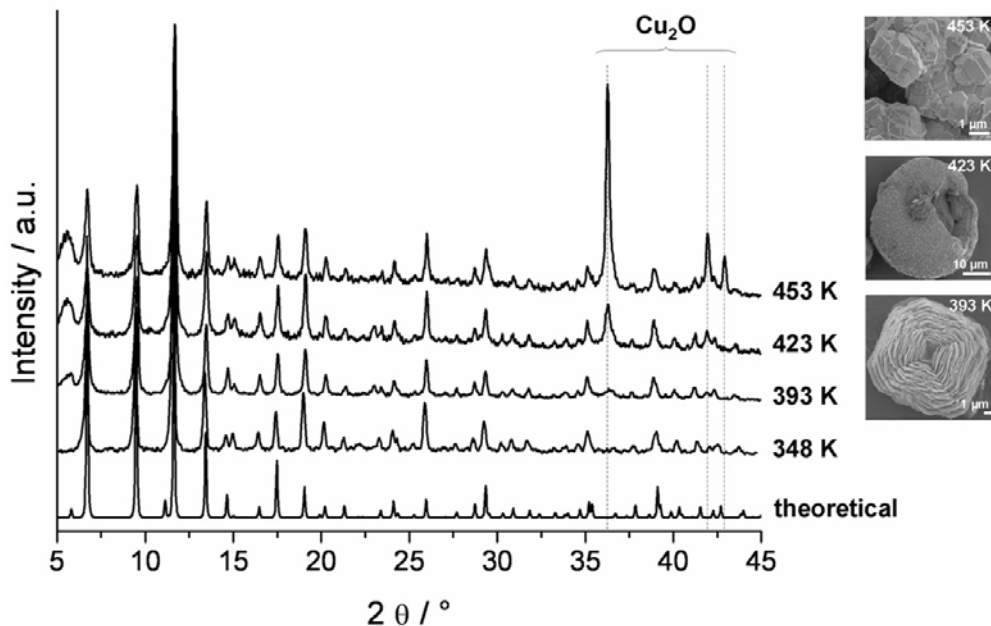


Figure 4.2.5. Influence of the synthesis temperature on the formation and amount of Cu₂O as by-product. The powder diffraction patterns of the samples obtained at different temperatures (348, 393, 423 and 453 K) are compared with the theoretical pattern of HKUST-1. The reflections according to Cu₂O are marked by vertical lines. The different morphologies of Cu₂O obtained at 393, 423 and 453 K respectively are presented in the scanning electron micrographs.

The intensity of the reflections belonging to Cu₂O increases with the increase of the synthesis temperature. Scanning electron microscopic investigations confirmed the presence of the by-product even at 393 K, although the reflections relative to the copper(I) oxide are not detectable in the diffraction pattern. The different morphologies of Cu₂O obtained at 393, 423 and 453 K respectively are presented in the SEM micrographs inserted

IV. Results and Discussion

in Figure 4.2.5. With increasing temperature the morphology changes from platelets to intergrown rhombohedra. The morphology of the HKUST-1 crystals was also characterized by electron microscopy. The crystals formed at higher temperatures don't present the well defined octahedral-morphology observed at 348 and 393 K. Representative crystals obtained at the different temperatures are shown in Figure 4.2.6.

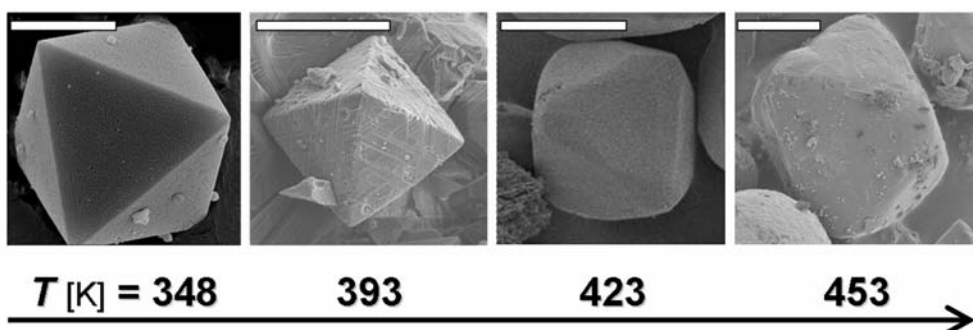


Figure 4.2.6. Influence of synthesis temperature on the morphology of HKUST-1. Each scale bar in the different micrographs corresponds to 10 μm .

The effect of the temperature on the synthesis of HKUST-1 was also investigated using $\text{Cu(OAc)}_2 \cdot \text{H}_2\text{O}$ as the metal salt. Instead of the formation of Cu_2O as by-product, an unknown phase is obtained in addition to the formation of HKUST-1. The amount of the impurity increases with increasing of the temperature, as confirmed by the XRD characterization (Figure 4.2.7).

After confirming that pure phase HKUST-1 can be obtained at 348 K when starting from $\text{Cu}(\text{NO}_3)_2 \cdot 2.5\text{H}_2\text{O}$, the synthesis procedure was further optimized. Therefore, the evolution of the relative yield of $\text{Cu}_3(\text{BTC})_2(\text{H}_2\text{O})_3 \cdot x\text{H}_2\text{O}$ was studied as a function of the synthesis time (up to 350 h).

IV. Results and Discussion

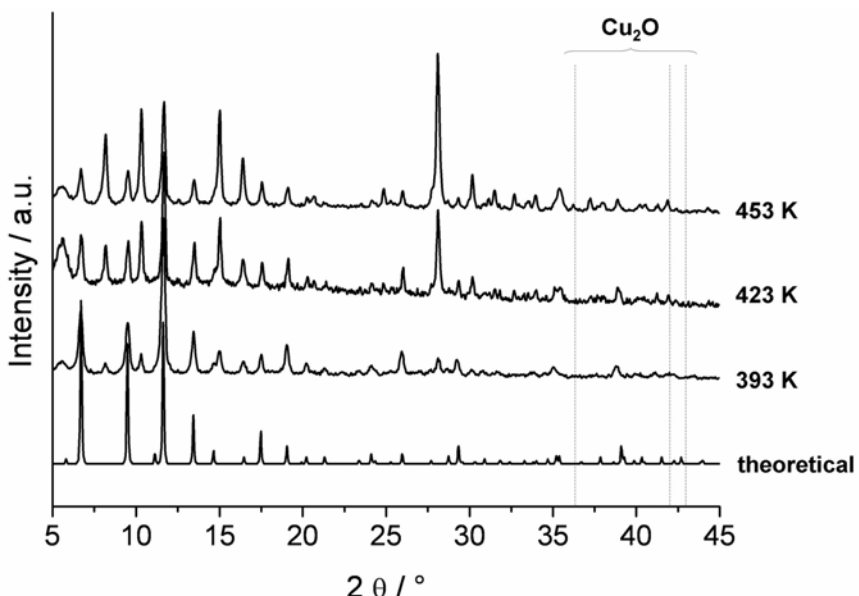


Figure 4.2.7. XRD patterns of the HKUST-1 samples synthesized at 393, 423 and 453 K starting from $\text{Cu}(\text{OAc})_2 \cdot 3\text{H}_2\text{O}$. The increasing of the competitive phase with the increase of the temperature is shown. The reflections positions according to Cu_2O are marked by vertical lines; Cu_2O is not formed when starting from copper(II) acetate as metal salt.

The reaction product was filtered off, rinsed with doubly distilled water, and weighed out after storing in water saturated atmosphere over night. The relative yield was calculated assuming a molar mass of $947.71 \text{ g mol}^{-1}$ corresponding to the water content of a full rehydrated material ($\text{Cu}_3[(\text{OOC})_3\text{C}_6\text{H}_3]_2(\text{H}_2\text{O})_3 \cdot 16\text{H}_2\text{O}$). [9] Plotting the relative yield versus time results in a sigmoid curve, which shows that a maximum yield of about 80 % is achieved after 320 h (Figure 4.2.8).

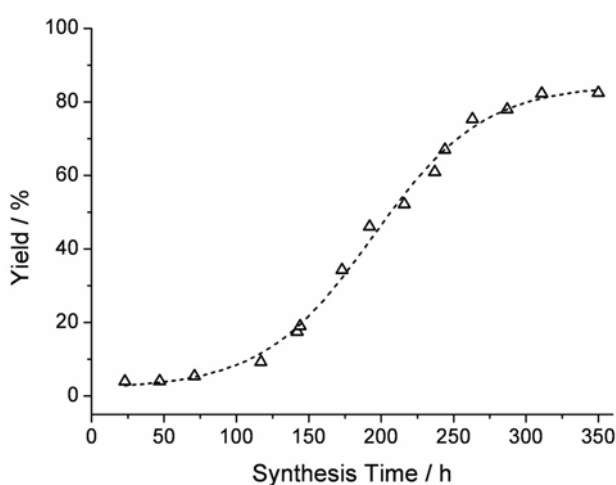


Figure 4.2.8. Relative yield of HKUST-1 as function of the synthesis time at 348 K. The sigmoid trend is emphasized by the dashed-line.

IV. Results and Discussion

Effect of Concentration on HKUST-1 Crystal Morphology. After the determination of the optimum starting material and reaction temperature, HT methods were employed for detailed investigation of the synthesis conditions. Thus, the effect of concentration of the reaction mixtures on the product morphology was investigated in a third experiment. The reaction mixtures were prepared by multiplying the molar amount of $\text{Cu}(\text{NO}_3)_2 \cdot 2.5\text{H}_2\text{O}$ and H_3BTC in the adapted recipe described above by a concentration factor "x" (with $x = 0.1, 0.25, 0.5, 0.75, 1.0, 1.3$, and 1.75). To test reproducibility, the same mixture compositions were repeated at different positions in the 24-reactors array. The multiclave was sealed and treated for 24 h in a preheated oven at 348 K (Table 4.2.5).

Table 4.2.5. The diagram shows the propagated waves from the light scattered by the particles.

Reactor Number	Concentration Factor (x)	$\text{Cu}(\text{NO}_3)_2 \cdot 2.5\text{H}_2\text{O}$ (mmol)	BTC (mmol)
1	0.1	0.03	0.017
2	0.25	0.075	0.0425
3	0.5	0.15	0.085
4	0.75	0.225	0.1275
5	1.0	0.3	0.17
6	1.3	0.39	0.221
7	0.1	0.03	0.017
8	0.25	0.075	0.0425
9	0.5	0.15	0.085
10	0.75	0.225	0.1275
11	1.0	0.3	0.17
12	1.3	0.39	0.221
13	0.1	0.03	0.017
14	0.25	0.075	0.0425
15	0.5	0.15	0.085
16	0.75	0.225	0.1275
17	1.0	0.3	0.17
18	1.3	0.39	0.221
19	0.1	0.03	0.017
20	0.25	0.075	0.0425
21	0.5	0.15	0.085
22	0.75	0.225	0.1275
23	1.0	0.3	0.17
24	1.3	0.39	0.221

According to the XRD data, HKUST-1 was obtained as pure phase for all concentrations. The SEM micrographs (Figure 4.2.9) reveal a morphological evolution of the crystals with increasing concentration of the reaction mixtures.

IV. Results and Discussion

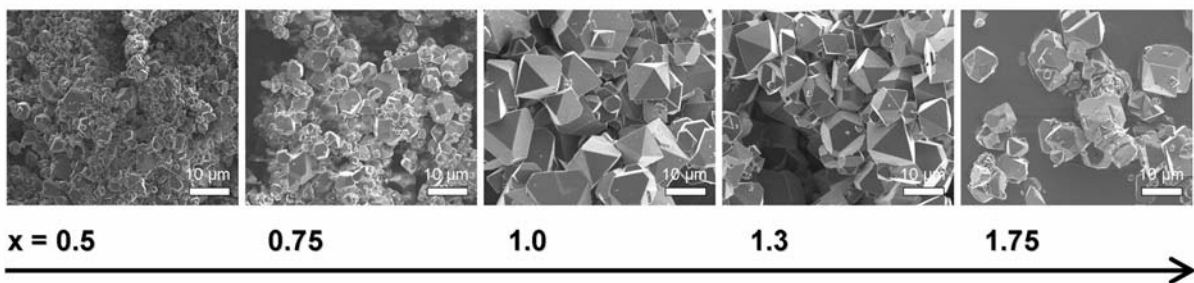


Figure 4.2.9. Influence of concentration on the morphology for HKUST-1. The synthesis was performed under solvothermal conditions at 348 K for 24 h starting from $\text{Cu}(\text{NO}_3)_2 \cdot 2.5\text{H}_2\text{O}$. The scale bar of each micrograph corresponds to 10 μm . “ x ” denotes the concentration factor in respect to the synthesis recipe described in the literature. [20]

The samples obtained at low concentration present agglomerated crystals with truncated octahedral shape of about 1 μm for $x = 0.5$, and slightly bigger crystals of around 5 μm for the sample corresponding to a concentration factor of 0.75. Interestingly, the crystals formed at higher concentrations ($x = 1.0, 1.3$) show a well defined octahedral shape and an average size of 10-15 μm . When starting from a concentration factor 1.75, the typical octahedral morphology of the crystals becomes less defined and irregular. Such a tuning of the morphology of porous crystalline materials is great interest for the assembly thin layers for sensing applications. [26]

4.2.2 Conclusion

The efficiency of employing high-throughput methods to understand the influence of process and compositional parameters on the synthesis of metal-organic frameworks was demonstrated. For both MOF-5 and HKUST-1, the choice of the metal salt has an enormous effect on the phase purity as well as on the product morphology, respectively. In particular, the influence of acetate acting as counter-ion is remarkable. When starting from metal acetates, smaller crystals are obtained; a possible explanation is a change in the nucleation rate of the crystallization process. Thus, higher nucleation rate is usually responsible for an increased number of crystals with limited size. Whereas in the synthesis of MOF-5 the change in the pH of the reaction medium due to the presence of acetate does not lead to by-products, in the synthesis of HKUST-1, the formation of an additional unknown phase is

IV. Results and Discussion

observed. Unexpectedly, with chloride salts no solid products have been obtained in either system under the conditions investigated here. This might be due to differences in solubility or owed to the complexation properties of the Cl^- ions. In the case of HKUST-1, an influence of the metal salt on the product formation is only observed at higher temperatures.

The influence of cosolvents on the formation of MOF-5 was verified employing $\text{Zn}(\text{NO}_3)_2 \cdot 6\text{H}_2\text{O}$, as well as ZnO . The formation of the metal-organic framework is sensitive to the presence of aromatic cosolvents. Thus, with decreasing polarity of the reaction medium the less MOF-5 is formed in favor of other unknown phases. However, the chosen salt plays an important role: in fact the mixture starting from ZnO leads to formation of the desired compounds at any DEF/cosolvent ratio.

The addition of small amounts of H_3O^+ or OH^- and water to the synthesis mixture of MOF-5 leads to the formation of two different compounds. While $\text{Zn}_3(\text{OH})_2(\text{BDC})_2 \cdot 2\text{DEF}$ is obtained under alkaline condition, the presence of H_3O^+ ions and water favor the formation of $(\text{H}_2\text{N}\text{Et}_2)_2[\text{Zn}_3(\text{BDC})_4] \cdot 3\text{DEF}$. The HT experiments permit to identify a clear trend in the reactivity of this system.

Finally, the synthesis procedure for HKUST-1 was further optimized. Cu_2O free samples can be obtained by decreasing the reaction temperature to 348 K; the systematic investigation of the synthesis time shows that after 320 h a maximum yield is achieved. Furthermore, the size and the morphology of the HKUST-1 crystals could be controlled varying the concentration of the starting mixture.

In this section it was shown that compositional as well as process parameters can have a decisive influence on the morphology as well as on the phase purity of metal-organic frameworks, respectively. The understanding of these parameters is of key importance for the efficient synthesis of metal-organic frameworks with desirable properties and application potential.

IV. Results and Discussion

4.3. $(H_2NEt_2)_2[Zn_3(BDC)_4] \cdot 3DEF$: synthesis and characterization of a new metal-organic framework structure with 2D porous system

Carboxylic acids have emerged as an important family of ligands to design novel open framework inorganic-organic hybrid materials. [27,28] In particular the zinc-dicarboxylate compounds, like the isoreticular metal-organic frameworks (IRMOFs), were shown to be promising methane and hydrogen storage systems. [29,30] The $Zn^{2+}/1,4$ -benzenedicarboxylic acid reaction system is very sensitive to the variation of water content and the solvents employed in the starting mixture. Thus, many different structures, for example, $Zn(BDC) \cdot DMF \cdot H_2O$ (MOF-2) [31] $Zn_3(BDC)_3 \cdot 6CH_3OH$ (MOF-3), [32] and $Zn_4O(BDC)_3$ (MOF-5) [19] were synthesized in the last few years. As presented in the systematic investigation (Section 4.2) of the synthesis parameters of MOF-5, the zinc terephthalate $Zn_3(OH)_2(BDC)_2 \cdot 2DEF$ was obtained under more basic conditions. [23] While, the influence of the addition of small amounts of nitric acid to the synthesis mixture leads to the new zinc terephthalate $(H_2NEt_2)_2[Zn_3(BDC)_4] \cdot 3DEF$. The structure determination and the detailed characterization of the framework are presented in this section.

4.3.1 Results and Discussion

The new open-framework structure was synthesized under solvothermal conditions in a DEF solution of 1,4-benzenedicarboxylic acid in the presence of a sintered ZnO tablet. The reaction mixture was prepared in a sealed glass reactor by adding 80 mg (0.4815 mmol) of 1,4-benzenedicarboxylic acid to 10 ml DEF; a sintered ZnO tablet, previously immersed for 1 min in a 2M HNO_3 solution and dried at 60 °C for about 10 min , was further added. The closed system was placed into a preheated oven at 100-120 °C for 12-24 h. A colorless crystalline product resulted at the bottom of the reactor. Additionally, the entire surface of the ZnO tablet was covered with well-shaped crystals of the same product. After the

IV. Results and Discussion

removal of the tablet, the product was isolated by filtration, washed with DEF and dried at room temperature.

The amount of product obtained (a few mg at a time) as well as the reaction rate increased by employing an already used tablet. Thus the reaction seems to be strongly dependent on the diffusion of the zinc ions in the reaction solution, which should be faster for the already used and therefore activated ZnO tablet.

Performing the reaction with a new or a used pellet resulted also in different dimensions of the crystals: with a new ZnO sintered tablet bigger and less intergrown crystals were produced than using pellets previously employed in another synthesis batch. This confirms also the importance of the diffusion of the Zn^{2+} ions. Hexagonal plate-shaped crystals (30–300 μm size) were observed in the solution and on the entire surface of the ZnO tablet (Figure 4.3.1).

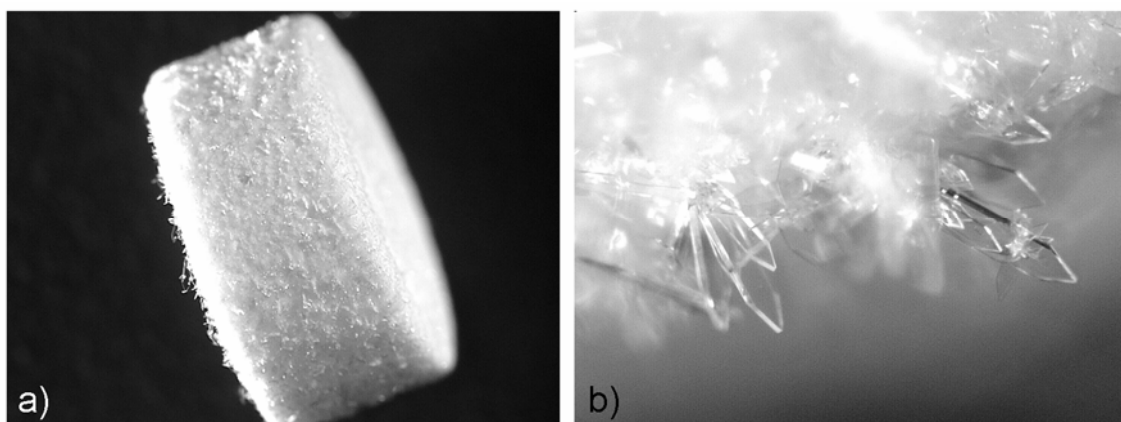


Figure 4.3.1. a) Optical micrograph of a ZnO tablet covered with $(H_2NEt_2)_2[Zn_3(BDC)_4]I \cdot 3DEF$ crystals; (b) particular of the crystals on the tablet surface.

X-ray powder diffraction analysis as well as semi-quantitative elemental analysis of both filtrated and surface crystals confirmed the synthesis of the new phase. The XRD pattern of a typical sample together with the simulated one, obtained from the crystallographic data, is presented in Figure 4.3.2.

IV. Results and Discussion

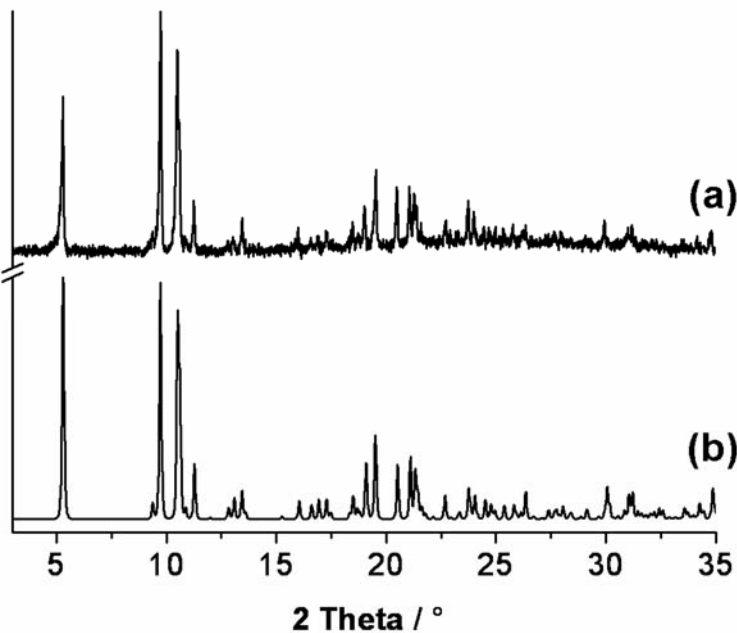


Figure 4.3.2. Comparison of the (a) X-ray powder diffraction pattern of a powder sample with (b) the theoretical pattern of $(H_2N\text{Et}_2)_2[\text{Zn}_3(\text{BDC})_4]\cdot 3\text{DEF}$.

Crystal structure determination

A single crystal of dimensions $0.19 \times 0.13 \times 0.03 \text{ mm}^3$, suitable for single-crystal X-ray diffraction analysis, was selected under a polarizing microscope and carefully attached to a capillary. The measurement was carried out on a Enraf-Nonius Kappa-CCD diffractometer, operating at 50 kV and 80 mA, equipped with a Enraf Nonius Rotating Anode X-ray generator (Mo $K\alpha$ radiation, $\lambda = 71.073 \text{ pm}$) running at 4 kW. For data reduction the programs HKL Denzo and Scalepack [33] were used. The structure was solved by direct methods and refined using the program package SHELXT. [34] All H-atoms bound to C-atoms and the N-atom of the diethylammonium ion were placed onto calculated positions. These H-atoms were refined using a riding model and fixing the temperature factor to be 1.2 times the value of the atom they are bonded to.

Crystal data as well as details of the data collection and refinement for $(H_2N\text{Et}_2)_2[\text{Zn}_3(\text{BDC})_4]\cdot 3\text{DEF}$ are summarized in Table 4.3.1. Selected bond lengths and angles are given in Table 4.3.2. Hydrogen bond distances and angles are presented in Table 4.3.3. CCDC 281855, contains the supplementary crystallographic data for this paper.

IV. Results and Discussion

The structure of $(\text{H}_2\text{NEt}_2)_2[\text{Zn}_3(\text{BDC})_4]\cdot\text{3DEF}$ consists of trimetallic zinc building units, that are interconnected by eight BDC units each. Thus a three-dimensional anionic framework is formed.

Table 4.3.1. Summary of crystal data, intensity measurement and refinement parameters for $(\text{H}_2\text{NEt}_2)_2[\text{Zn}_3(\text{BDC})_4]\cdot\text{3DEF}$.

crystal system	monoclinic
space group	$C2/c$
a (pm)	3337.24(5)
b (pm)	983.17(2)
c (pm)	1819.67(2)
β ($^{\circ}$)	92.455(1)
V (10^6 pm 3)	5965.0(2)
Z	4
formula mass (g mol $^{-1}$)	1304.29
ρ (g cm $^{-3}$)	1.452
$F(000)$	2720
crystal size (mm 3)	0.19 x 0.13 x 0.03
μ (mm $^{-1}$)	1.272
absorption correction	none
θ range ($^{\circ}$)	3.134–26.022
range in hkl	-41 $\leq h \leq$ 41 -12 $\leq k \leq$ 12 -22 $\leq l \leq$ 22
tot. data collected	22167
unique/observed data ($I > 2\sigma(I)$)	5859 / 4533
extinction coefficient	0.00027(7)
R (int)	0.0643
R_1 , wR_2 ($I > 2\sigma(I)$)	0.0395, 0.0843
R_1 , wR_2 (all data)	0.0620, 0.0914
goodness of fit	1.061
no. of variables	382
Δe min/max (10 6 e pm $^{-3}$)	-0.355 / 1.012

IV. Results and Discussion

Table 4.3.2. Selected bond lengths (pm) and bond angles ($^{\circ}$) for $(\text{H}_2\text{N}\text{Et}_2)_2[\text{Zn}_3(\text{BDC})_4]\cdot\text{3DEF}$.

bond lengths (pm)					
Zn1–O7	192.6(2)	Zn1–O3	196.6(2)	Zn1–O1	197.7(2)
Zn1–O6	198.5(2)	Zn2–O2 (x2)	202.1(2)	Zn2–O4 (x2)	204.7(2)
Zn2–O6 (x2)	224.9(2)	O1–C1	126.1(3)	O2–C1	125.8(3)
O5–C9	123.5(3)	O6–C9	129.7(3)	O7–C13	128.5(4)
O8–C13	123.3(4)	C1–C2	150.2(4)	C5–C8	149.7(4)
C9–C10	149.6(4)	C13–C14	150.1(4)	C–C _{ar.} (x10)	137.7(4) –
O9–C17	123.2(4)				139.2(4)

Table 4.3.3. Hydrogen bonds (bond distances in pm, angles in $^{\circ}$) for $(\text{H}_2\text{N}\text{Et}_2)_2[\text{Zn}_3(\text{BDC})_4]\cdot\text{3DEF}$; D = proton donor, A = proton acceptor.

D–H \cdots A	D–H	H \cdots A	D \cdots A	$\angle D\text{--H} \cdots A$
N2–H21 \cdots O5	90 *	203.3(1)	278.6(1)	140.4
N2–H22 \cdots O9	90 *	185.8(1)	274.8(1)	169.5

The pore space is occupied by DEF molecules and $\text{H}_2\text{N}\text{Et}_2^+$ ions, produced by in-situ hydrolysis of DEF. [35,36]

The asymmetric unit of the $[\text{Zn}_3(\text{BDC})_4]^{2-}$ network is shown in Figure 4.3.3. There are two symmetrically independent Zn^{2+} and three BDC ions. Zn1 is tetrahedrally coordinated to carboxylate oxygen atoms belonging to four carboxylate groups while Zn2 is octahedrally coordinated to six different carboxylate groups.

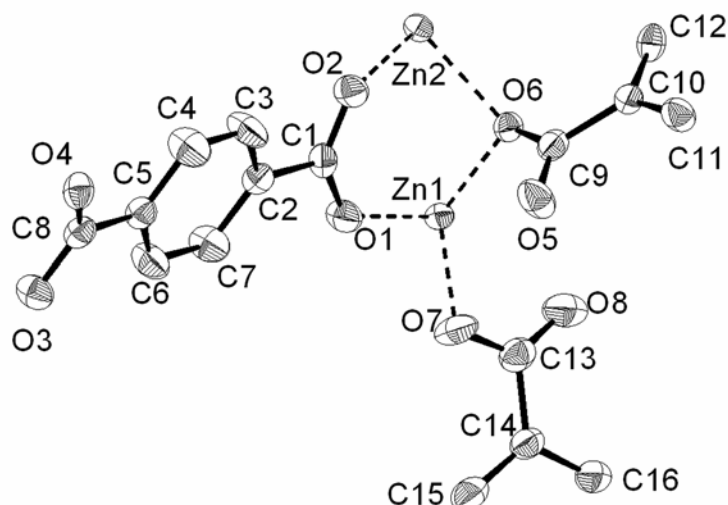


Figure 4.3.3. Asymmetric unit of the $[\text{Zn}_3(\text{BDC})_4]^{2-}$ network, with non-hydrogen atoms represented by thermal ellipsoids drawn at the 75% probability level.

IV. Results and Discussion

It is possible to distinguish three different coordination modes of the carboxylate groups to the trimetallic units (Figure 4.3.4). In the first one (type-A), both oxygen atoms of the carboxylate group are involved in the coordination of two zinc atoms, thus bridging Zn(1)O₄ tetrahedra and Zn(2)O₆ octahedra; in the second coordination mode (type-B) just one of the two oxygen atoms of the carboxylate groups is coordinating to both Zn1 and Zn2 at the same time, thus bridging the two metal centers; in the third coordination mode (type-C), also one oxygen atom of the carboxylic function is involved, but in this case only a terminal coordination to the tetrahedrally surrounded Zn1 atom is observed.

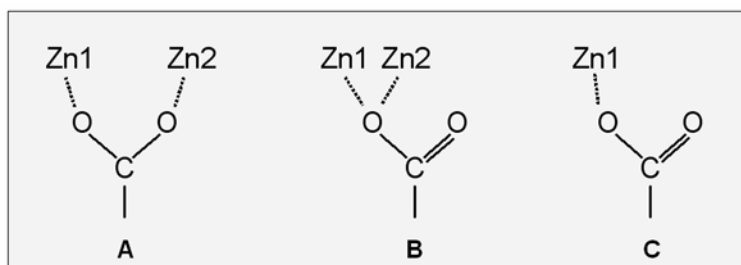


Figure 4.3.4. Coordination modes observed in $(\text{H}_2\text{NEt}_2)_2[\text{Zn}_3(\text{BDC})_4] \cdot 3\text{DEF}$. Type-A: both oxygen atoms of the carboxylic group are bridging two metal ions, Type-B: only one carboxylic oxygen atom (μ_2 -oxygen) is coordinating both tetrahedral and octahedral zinc centers, Type-C: one terminal coordinating oxygen atom.

The structure can be built using these different coordination modes in the following way: altogether, each trimetallic unit is connected to eight terephthalate molecules; in the *b,c*-plane six BDC ligands are found (four type-A and two type-B). Those terephthalic ions interconnect the trimetallic zinc units, and a (3,6)-net is formed (Figure 4.3.5).

IV. Results and Discussion

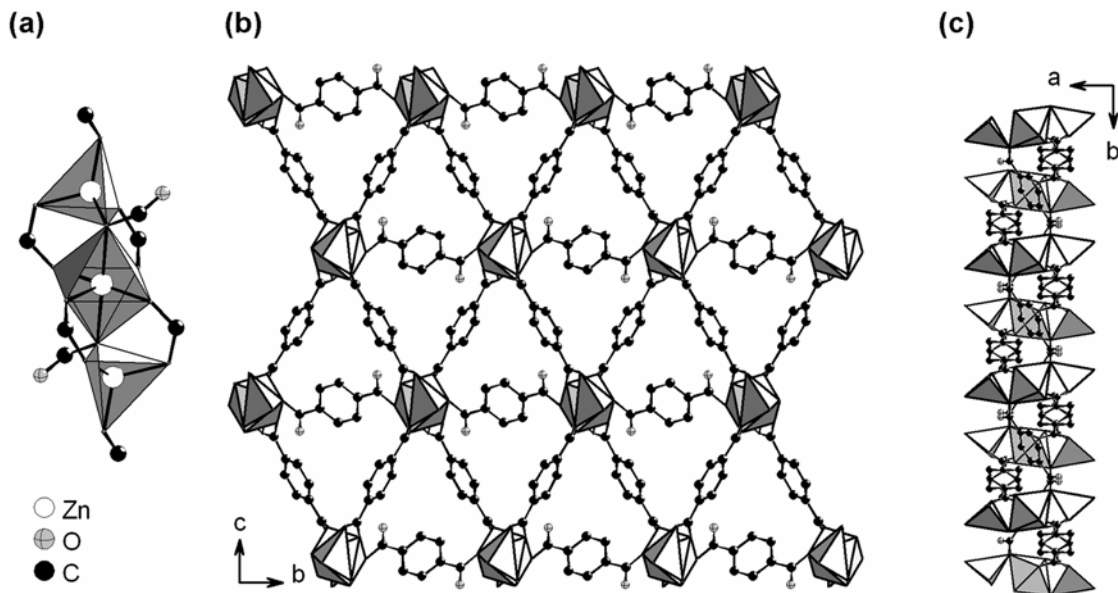


Figure 4.3.5. Trimetallic zinc unit (a); Type-A and B BDC-ligands interconnecting the trimetallic units (presented in the picture as polyhedra), thus forming a dense layer (b) in the b,c -plane. (c) view along the c -direction.

The other two BDC units are bridging the resulting 2D layers in a type-C mode through the terminal Zn(1) tetrahedra in the a -direction (Figure 4.3.6). Thus a two-dimensional porous system is formed with channels along [010] and [001] and pore openings around 800×670 pm and 800×550 pm, respectively. These dimensions were obtained from the corresponding H···H distances corrected by subtraction of the covalent radius of the H-atoms.

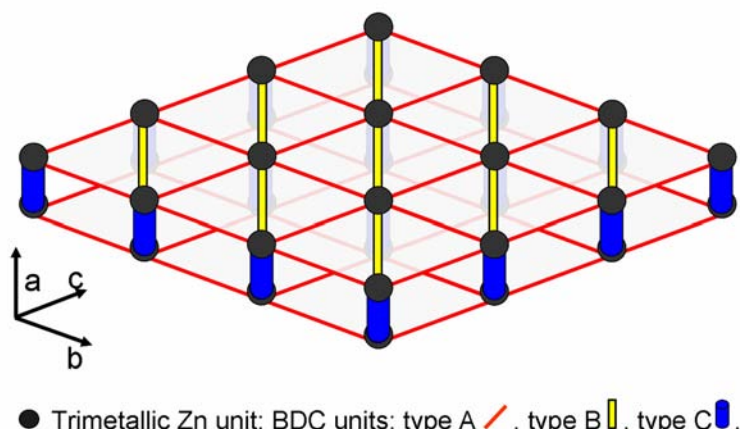


Figure 4.3.6. Schematic representation of the three-dimensional anionic framework: the layers in the b,c -plane are formed by the interconnection of the trimetallic units through type-A and type-B BDC ligands. These layers are bridged by type-C BDC units along the a -direction.

IV. Results and Discussion

Two crystallographically unique DEF molecules and one $\text{H}_2\text{N}^+\text{Et}_2^+$ ion are occupying the channel space. They are partially connected to the framework and to each other by hydrogen bonds. Thus, both hydrogen atoms (H21 and H22) of the ammonium ion are involved in medium strong hydrogen bond interactions (Figure 4.3.7).

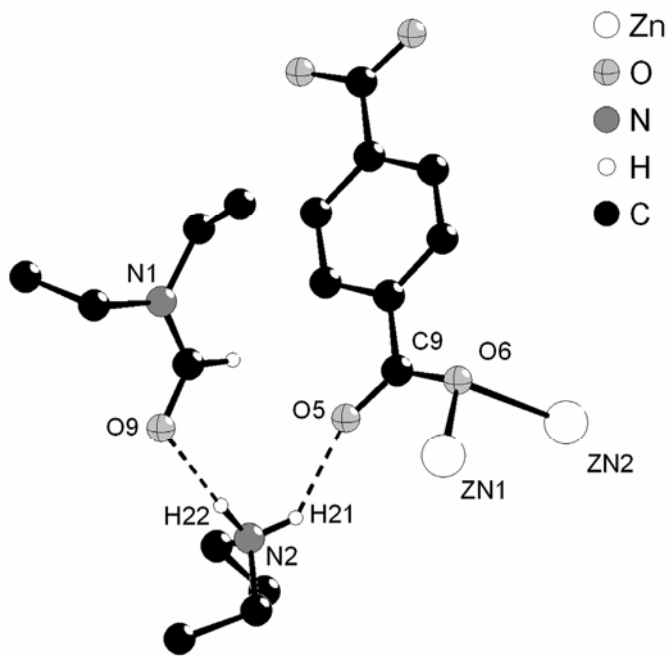


Figure 4.3.7. Hydrogen-bond interactions between the hydrogen atoms of the $\text{H}_2\text{N}^+\text{Et}_2^+$ ion, with the oxygen atoms of one DEF molecule and the $[\text{Zn}_3(\text{BDC})_4]^2-$ framework.

H21 interacts with the uncoordinated carboxylic oxygen-atom of the type-B BDC unit ($\text{N}2\cdots\text{O}5 = 278.6(1)$ pm); while H22 is bridging to the oxygen atom of one formamide group ($\text{N}2\cdots\text{O}9 = 274.8(1)$ pm). The other crystallographically distinct but structurally disordered DEF molecule shows no preferential interaction with the framework.

Thermogravimetric analysis.

The thermogravimetric diagram (Figure 4.3.8) shows a first weight loss of 34% in multiple, but not well defined steps between room temperature and 260 °C. This weight loss can be assigned to the removal of the molecules/ions present in the channels: three N,N' -diethylformamide and two diethylamine molecules per formula unit (calculated weight loss = 35%). In the next step (260-330 °C), a weight loss of 11% is detectable that could correspond to the degradation of one terephthalic-acid molecule per formula unit.

IV. Results and Discussion

(theoretical weight loss = 12.5%) leading to $[\text{Zn}_3(\text{BDC})_3]$. This composition was confirmed by elemental analysis of the compound thermally treated at 300 °C. The resulting structure is thermally stable up to 400 °C. Further increase of the temperature, above 500 °C, leads to the formation of ZnO .

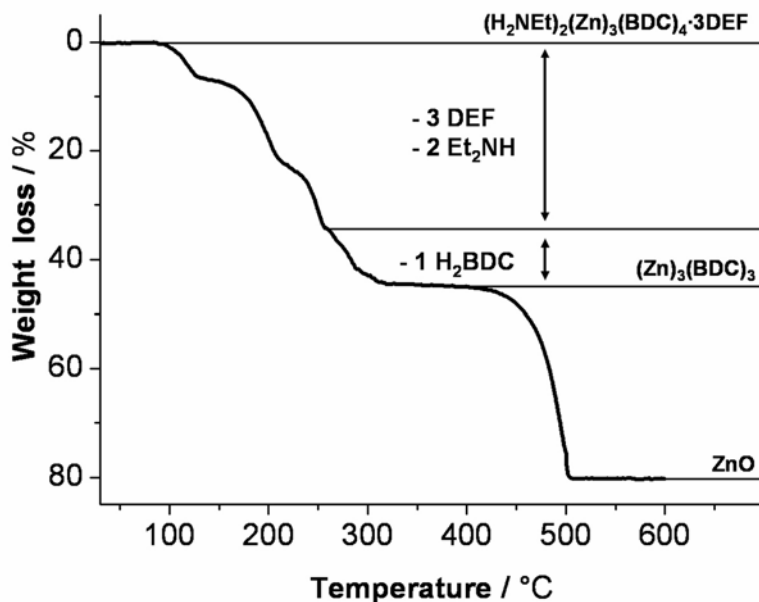


Figure 4.3.8. Thermogravimetric diagram of $(\text{H}_2\text{NEt}_2)_2[\text{Zn}_3(\text{BDC})_4] \cdot 3\text{DEF}$.

These results were confirmed by powder X-ray diffraction as well as elemental analysis of the as-synthesized product (Calcd.: C, 50.65; H, 5.64; N, 5.37. Anal. Found: C, 48.30; H, 5.64; N, 4.77), and the thermally treated compound at 300 °C (Calcd.: C, 41.87; H, 1.76; N, 0.00. Anal. Found: C, 40.99; H, 2.03; N, 0.08).

Temperatur- dependent X-ray diffraction analysis.

To obtain more information on the thermal behavior of the title compound and its structural stability at elevated temperatures, temperature dependent X-ray diffraction was performed. As can be seen in Figure 4.3.9, only small changes in the intensities of the diffraction peaks are observed up to 250 °C. This information in combination with the TGA data, indicates that the three-dimensional framework structure is maintained, and only the guest-molecules in the pores are removed. The proposed removal of one BDC molecule, between 260 and 330 °C, leads to a new crystalline phase with a distinct XRD pattern, stable up to 400 °C.

IV. Results and Discussion

The complete collapse of the framework and the formation of ZnO are clearly demonstrated by the XRD patterns collected from the decomposition product above 500 °C. No additional phases can be detected.

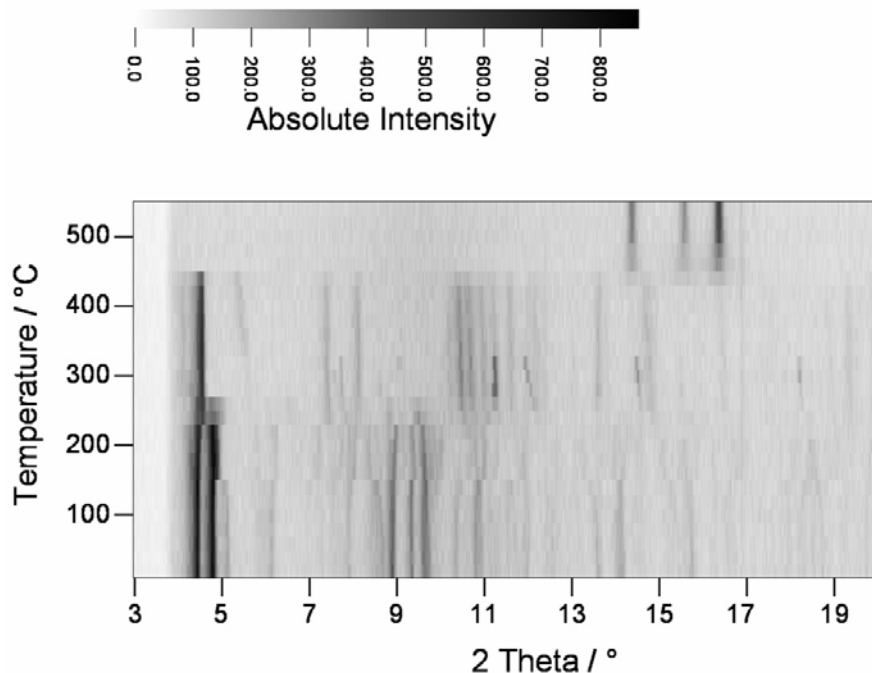


Figure 4.3.9. Temperature-dependent powder XRD analysis collected using Mo $K\alpha$ radiation ($\lambda = 71.073 \text{ pm}$).

Solid-state NMR spectroscopy.

The $^{13}\text{C}\{^1\text{H}\}$ decoupled MAS spectrum of $(\text{H}_2\text{NEt}_2)_2[\text{Zn}_3(\text{BDC})_4]\cdot 3\text{DEF}$ is shown in Figure 4.3.10. The signals can be separated into four different groups:

- 1) the $-\text{CH}_3$ groups (10-20 ppm)
- 2) $-\text{CH}_2-$ groups (30-60 ppm),
- 3) aryl C-atoms (140-120 ppm),
- 4) formamide and carboxylate C-atoms (165-170, and 170-175 ppm, respectively).

The signals at 10.60, 11.22, 12.90, and 14.28 ppm can be assigned to the methyl groups of the DEF molecules and the diethylammonium ions. Theoretically up to five signals could be present, but due to signal overlap not all resonances are observed. The methylene resonances occur between 30 and 60 ppm: five different lines can be identified (41.48, 43.78, 50.51, 52.59 and 57.51 ppm) and assigned to the $-\text{CH}_2$ of the DEF molecules and the

IV. Results and Discussion

diethylammonium ions. The two resonances of the C-atoms belonging to the formamide functionalities can be observed, as very weak signals, at 164.57 and 164.88 ppm.

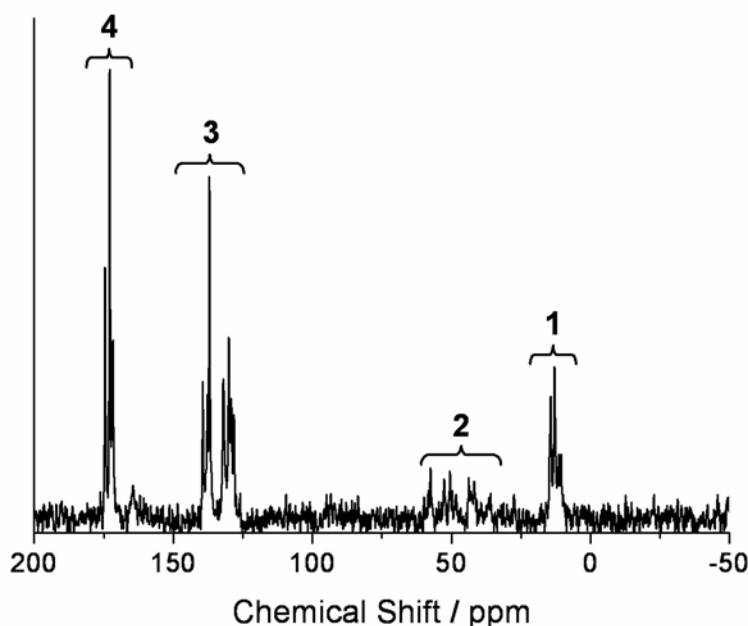


Figure 4.3.10. $^{13}\text{C}\{^1\text{H}\}$ decoupled MAS NMR spectra of $(\text{H}_2\text{NEt}_2)_2[\text{Zn}_3(\text{BDC})_4]\cdot 3\text{DEF}$ collected at spinning rates 10 kHz. 1} $-\text{CH}_3$ groups (10-20 ppm), 2} $-\text{CH}_2-$ groups (30-60 ppm), 3} aryl C-atoms (140-120 ppm), and 4} formamide and carboxylate C-atoms (165-170, and 170-175 ppm, respectively)

The strong resonances at $\delta = 171.70$, 172.89 and 174.54 ppm are due to the carboxylate groups of BDC. The three signals in this region could be related to different coordination types of the BDC units in the crystal structure. Evidences of the aromatic contribution of BDC ligands are present in the region from 139.40 to 129.99 ppm.

FT-IR and Raman spectroscopy.

The vibrational spectra of the title compound and the thermally treated compound up to 250 and 300 °C were collected. Analytically important regions of the spectra are the ones containing C–H or C=O vibrational bands typical for the incorporation of molecules in the channels and the coordination mode of the carboxylate functionality, respectively. The typical bands related to the BDC ligands, DEF molecules and ammonium ions could be observed in the vibrational spectra of the title compound. The Raman data are actually very useful to demonstrate the removal of the guest molecules from the channel system, in fact the stretching vibrations bands between 2850 and 2970 cm^{-1} that are due to $-\text{CH}_3$ and –

IV. Results and Discussion

CH_2- groups belong to the DEF molecules and to the ammonium ions only. In Figure 4.3.11a, the Raman spectra of the as-synthesized compound and the thermally treated products at 250 and 300 °C, respectively, are presented. The aliphatic C–H stretching vibration bands in the region 3000–2800 cm^{-1} disappear after heating the compound at 250 °C as does the band at 3058 cm^{-1} belonging to the N–H⁺ stretching vibrations; only the contribution of the aromatic C–H is still visible at 3080 cm^{-1} in the spectra of the heated compound.

The IR spectrum of the titled compound (Figure 4.3.11b top) is compared to the Raman data (bottom) collected at the same conditions. shows vibrational bands at 1598 cm^{-1} and 1392 cm^{-1} characteristic for the asymmetric and symmetric stretching vibration of the carboxylic groups of the BDC coordinated to a metal center; the absence of bands in the region of 1715–1680 cm^{-1} typical of protonated carboxylic groups of BDC is in agreement with the determined structure where a complete deprotonation of the terephthalic acid molecules was found.

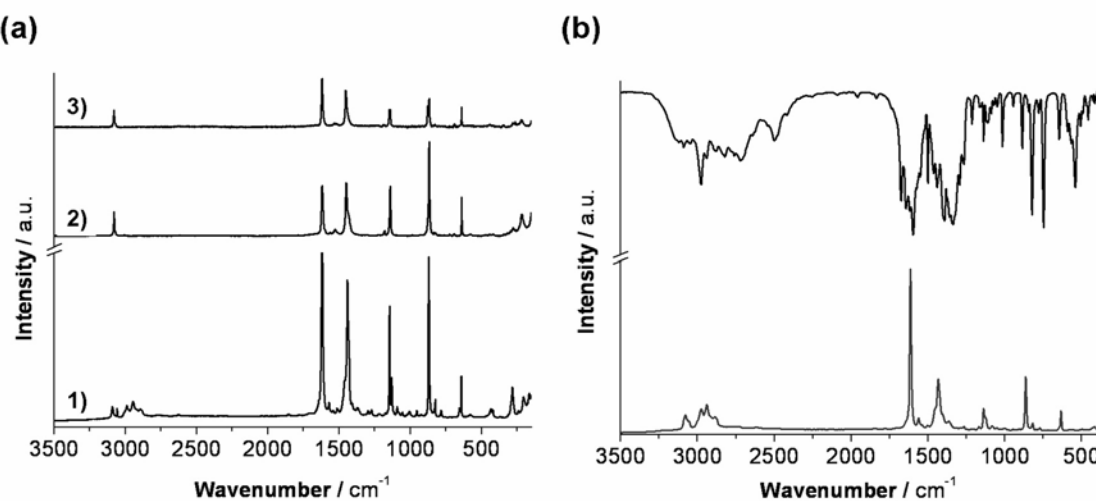


Figure 4.3.11. a) Single-crystal Raman spectra of $(\text{H}_2\text{N}\text{Et}_2)_2[\text{Zn}_3(\text{BDC})_4]\cdot 3\text{DEF}$ (1) as synthesized, thermally treated for three hours with a heating rate of 1°/min (2) at 250 °C and (3) at 300 °C. b) Comparison of IR (top) and Raman (bottom) powder spectra collected at the same conditions.

Other characteristic bands of the ligands due to the C=C stretching vibration of the *p*-disubstituted aromatic ring were found at 1502 cm^{-1} up to 1525 cm^{-1} . Overtone and combination bands due to the C–H out-of-plane deformation vibration and characteristic for 1,4-disubstituted benzene rings occur in the region 2000–1750 cm^{-1} . The absorption at

IV. Results and Discussion

1676cm^{-1} can be assigned to the C=O stretching of the amide (DEF) and the band at 648cm^{-1} is typical for the NCO bending vibration of the DEF molecules. It was also possible to assign some bands to the diethyl-ammonium ion: the broad N-H stretching bands in the region between 2900 and 2700 cm^{-1} are typical for the hydrogen bonds of the two hydrogen atoms of the ammonium ion.

The removal of the DEF and ammonium ions and the stability of the pore system can also be demonstrated by sorption measurements. Figure 4.3.12 shows the N_2 -adsorption isotherm of the title compound thermally treated at $250\text{ }^\circ\text{C}$. The isotherm present the typical shape of microporous materials isotherms (Langmuir type) with N_2 condensation at higher relative pressures, which could be due to textural porosity. The pore volume of the new MOF derived from the N_2 sorption isotherm using the Dubinin-Radushkevich equation (0.02345 cc g^{-1}) and the apparent Langmuir surface area ($66.33\text{ m}^2\text{ g}^{-1}$) are comparable with those of MOF-3 (0.038 cc g^{-1} and $140\text{ m}^2\text{ g}^{-1}$). As in that case, the low pore volume value can be explained by the inability of N_2 molecules to diffuse freely into the pores at 77.34 K . [37]

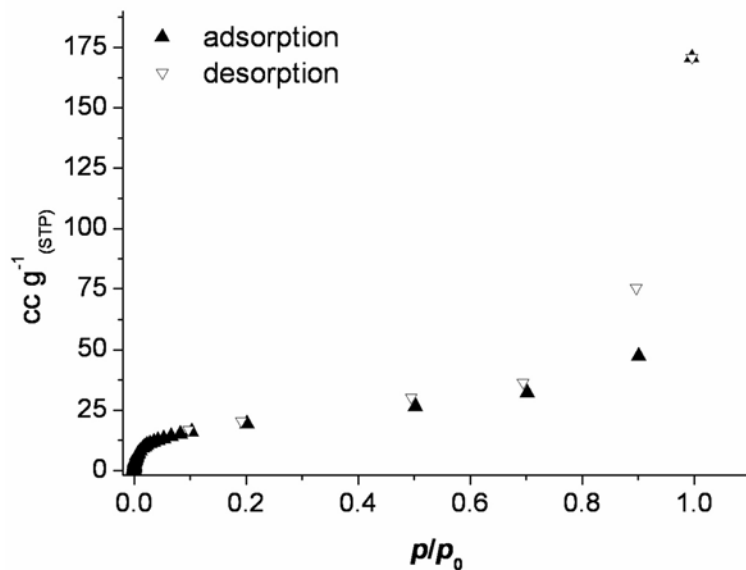


Figure 4.3.12. N_2 -sorption isotherm of the thermally treated title compound ($250\text{ }^\circ\text{C}$, 3 h).

The structure of $(\text{H}_2\text{NEt}_2)_2[\text{Zn}_3(\text{BDC})_4]\cdot3\text{DEF}$ can be compared to other compounds obtained in the $\text{Zn}^{2+}/1,4\text{-benzenedicarboxylic acid}$ reaction systems. While in MOF-5 a three

IV. Results and Discussion

dimensional cubic porous network is observed, the title compound contains some structural motives as observed in MOF-3. This framework, a triclinic system, contains also trimetallic zinc clusters and the coordination of the Zn^{2+} ions is similar to the one in the title compound: the central zinc atom (corresponding to Zn2 in our structure) is octahedrally coordinated to oxygen atoms of the carboxylic function as well, but the other two zinc centers are coordinated to five oxygen atoms; only three belonging to carboxylic groups and the other two from methanol molecules. Each two of the metal centers are bridged by three BDC units, two type-A and one type-B. The type-A BDC units are interconnecting the trimetallic cluster to form a (4,4)-net, different layers are pillared by a type-C BDC unit. Thus, a 3D inorganic-organic framework structure is formed. Another zinc terephthalate, $Zn_3(BDC)_3(H_2O)_3 \cdot 4DMF$, [38] can be considered in order to rationalize the possible structure of the crystalline product formed after heating the title compound up to 300 °C. This compound has a two-dimensional layered structure, consisting of trimetallic clusters that are connected in the *b,c*-plane by mono- and bidentate BDC groups in a (3,6)-net. The trimetallic unit contains one octahedral zinc ion between two tetrahedrally coordinated zinc ions binding to a terminal water ligand. The dimethylformamide molecules bridge the layers through hydrogen bonds with the water molecules.

4.3.2 Conclusion

A new zinc terephthalate $(H_2NEt_2)_2[Zn_3(BDC)_4] \cdot 3DEF$ has been synthesized and fully characterized. Trimetallic zinc units are interconnected by mono- and bidentate BDC groups (type-A and B) to form dense layers in the *b,c*-plane. The monodentate C-type BDC groups are bridging the layers along the *a*-direction, to form a 2D porous framework (Figure 4.3.13). The TGA data in combination with the temperature-dependent X-ray analysis as well as vibrational spectroscopy and elemental analysis of the as-synthesized and the heated (300 °C) compound, have confirmed the removal of the diethylformamide molecules as well as the diethylammonium ions.

IV. Results and Discussion

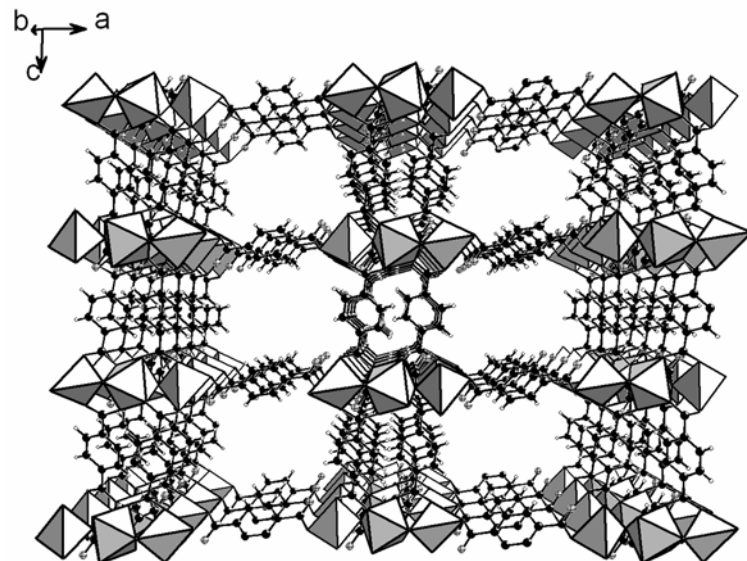


Figure 4.3.13. Three dimensional view of the channel system along [010].

The crystalline phase formed after temperature treatment above 250 °C is stable up to 400 °C and free pores are present in the framework, which was demonstrated by sorption measurements.

IV. Results and Discussion

4.4. Oriented growth of $\text{Cu}_3(\text{BTC})_2(\text{H}_2\text{O})_3 \cdot x\text{H}_2\text{O}$ on gold substrates tunable with functionalized self-assembled monolayers

In this part, the oriented growth of thin films of the metal-organic framework $\text{Cu}_3(\text{C}_9\text{H}_3\text{O}_6)_2(\text{H}_2\text{O})_3 \cdot x\text{H}_2\text{O}$ (HKUST-1) [20], on different functionalized self-assembled monolayers (SAMs) is presented.

The ability to control the orientation of the crystals and thus the pore-system in such films will open the way to more advanced applications such as selective gas-separation membranes or chemical sensors. The successful oriented growth of inorganic compounds such as calcium carbonate, [39] lead sulfide, [40] anatase, [41] zinc and iron oxide [21,42] and zeolites [43,44] on functionalized surfaces has inspired us to explore the effect of self-assembled monolayers with different functionalities on the growth of $\text{Cu}_3(\text{BTC})_2$. Its structural features and stability make this material an interesting candidate for the growth of thin films.

In many metal-organic frameworks such as MOF-5, the coordination sites of the metal-ions are blocked by the ligands serving as connectors in the network. In contrast, the Cu^{2+} -ions in $\text{Cu}_3(\text{BTC})_2$ present available coordination sites on the axial direction of the "paddle-wheel" Cu_2 -cluster (Figure 1.5), as described in Chapter 1. These accessible coordination sites are viewed as potential binding sites for the functional groups terminating different SAMs.

4.4.1 Results and Discussion

The detailed description of the experimental procedure for the direct growth of HKUST-1 on gold is presented in Section 2.3.2. (Scheme 2.6) For the growth of the $\text{Cu}_3(\text{BTC})_2$ crystals, gold substrates were modified with monolayers of $\text{HS}(\text{CH}_2)_{10}\text{X}$ (with $\text{X} = \text{CO}_2\text{H}$, CH_2OH , CH_3). The carboxylic acid functionality imitates the organic linker (1,3,5-benzenetricarboxylate (BTC)) in the open-framework structure, the alcohol-group mimics

IV. Results and Discussion

the coordinating water and the methyl-group presents an inert reference surface. Based on this reasoning and considering the fundamental differences in the coordination geometry in the structure, different orientations of the crystals on the -CO₂H and -OH functionalized SAMs respectively are anticipated. The formation of the self assembled monolayers has been proven by RAIR, as shown in Figure 4.4.1. The characteristic absorption bands indicating the -OH, -COOH, and -CH₃ functionalized surfaces are specifically emphasized in the graphs. Common to all the SAM are the -CH₂- groups of the aliphatic chain, which present high-frequency modes at 2920 and 2850 cm⁻¹ associated with the asymmetric and symmetric stretching vibrations, respectively; as well as the band at 721 cm⁻¹ assigned to the stretching vibration of the S-C bond. In spectrum (a), the band at 1060 cm⁻¹, which is typical of the C-O stretching vibration of primary alcohols, as well as the broad band (centered on 3350 cm⁻¹) related to the hydroxyl groups confirm the formation of the mercapto-1-undecanol-SAM. The C=O stretching characteristic of carboxylic acids in spectrum (b) validates the presence of the 11-Mercaptoundecanoic acid-SAM; while the -CH₃ groups are identify by the asymmetric and symmetric stretching vibrations at 2954 and 2875 cm⁻¹, respectively.

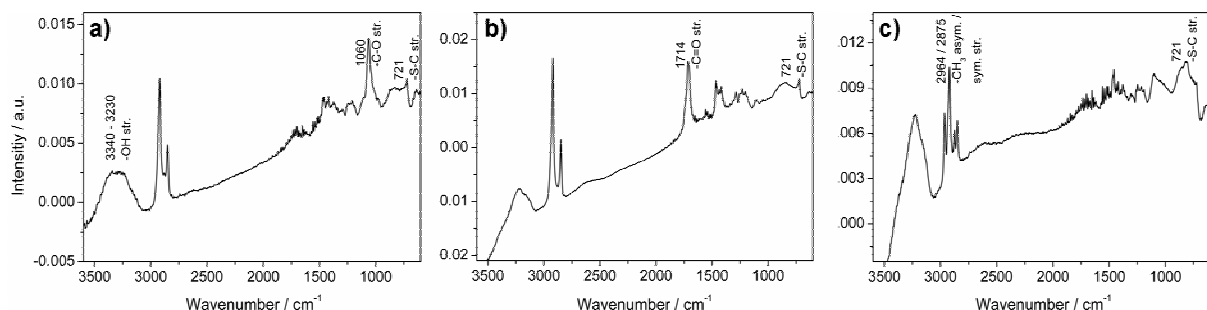


Figure 4.4.1. RAIR-spectra of alkanethiol self-assembled monolayers on gold substrate: (a) 11-Mercapto-1-undecanol-SAM, (b) 11-Mercaptoundecanoic acid-SAM, and (c) 1-Mercaptoundecan-SAM.

The stability of the -OH and -COOH SAMs was studied, via RAIR, after immersion of the gold slides in a Cu²⁺/H₂O/EtOH solution for the longest immersion time of 112 h. No indications of damage to the SAM were found as shown in Figure 4.4.2. Interestingly, in the case of the COOH-terminated SAM it is possible to observe a shift of the C=O band, from 1714 cm⁻¹ in the as synthesized SAM typical of a COOH group, to lower wavenumbers

IV. Results and Discussion

(1554 and 1454 cm⁻¹) typical of the asymmetric and symmetric stretching of the carboxylate units, [45] which indicates the binding of copper ions to the SAM (but no damage to the SAM). Furthermore, eventual esterification reaction of the -OH functionality of the SAM with the H₃BTC in solution could be studied. The OH-SAM was immersed for 112 h at room temperature in a 0.02 M H₃BTC solution in H₂O : EtOH mixture (ratio 1 : 1; the concentration selected is comparable to the BTC concentration in the RT crystallization solution used for the MOF growing step). No bands related to ester features or to the aromatic ring of BTC could be detected in this experiment (Figure 4.4.2b). Since the formation of an ester is an equilibrium reaction, at these conditions the presence of a great excess of water in the mother liquor (50%), strongly disfavors the esterification of the BTC with the OH-terminated SAM. Thus, esterification of the OH-SAM does not occur. Nevertheless, several studies reported in the literature describe esterification of an OH-functionalized SAM in solution in the presence of H₂SO₄ or other catalysts, [46] or by reaction of the OH groups with a carboxylic acid chloride [47] (all at rather low yield). Other examples concern reactions of the -OH-SAM with the vapor phase or *via* ionic collision. [48] The difficulties of esterification on an OH-SAM interface are mainly due to sterical impediments. One can find examples of esterification on mixed OH-SAMs, where shorter chain thiols are used as spacer to avoid steric limitations. [49]

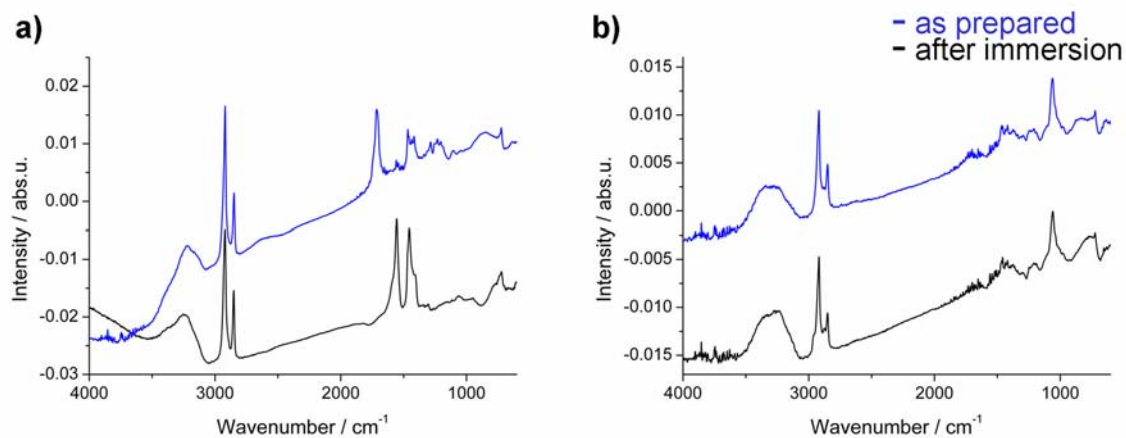


Figure 4.4.2. RAIR-spectra of alkanethiol self-assembled monolayers on gold substrate before (blue) and after (black) immersion of the gold slides in a Cu²⁺/H₂O/EtOH solution for the longest immersion time of 112 h. The spectra in (a) are related to 11-Mercapto-1-undecanol-SAM, while (b) corresponds to 11-Mercaptoundecanoic acid-SAM.

IV. Results and Discussion

Thin films of $\text{Cu}_3(\text{BTC})_2$ crystals were obtained on each modified gold surface. No crystallization takes place on bare gold surfaces. Figure 4.4.3 shows the interesting feature of the MOF consisting in a typical color change, from turquoise to deep blue, when removing the weakly coordinated water molecules from the coordination sites on the axial direction of the “paddle-wheel” Cu_2 -cluster. Thus, a first proof of the formation of the structure $\text{Cu}_3(\text{C}_9\text{H}_3\text{O}_6)_2(\text{H}_2\text{O})_3 \cdot x\text{H}_2\text{O}$. Highly-ordered thin films of $\text{Cu}_3(\text{BTC})_2$ were formed on the SAMs as demonstrated by the diffraction patterns shown in Figure 4.4.4.

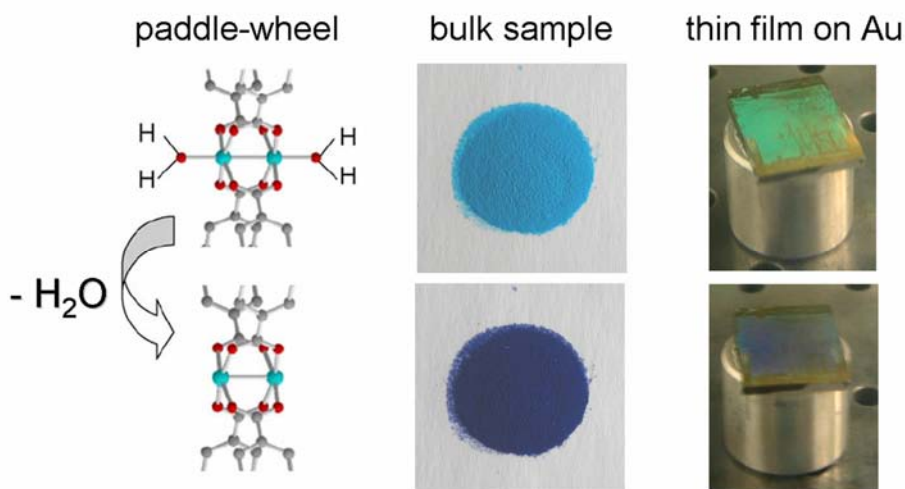


Figure 4.4.3. Color change in HKUST-1 samples (bulk as well as film) due to the removal of the water molecules coordinated to the Cu^{2+} in the axial direction of the paddle-wheel unit. The copper atoms are represented by the light-blue spheres, oxygen and carbon atoms correspond to the red and grey spheres, respectively.

The film grown on the -COOH self-assembled monolayer is highly oriented along the [100]-direction, while the OH-modified surface induces a completely different orientation along the [111]-direction. Homogeneous but less oriented thin films are also obtained on the methyl-SAM. Taking into account the typical octahedral morphology (Figure 4.2.6) of the HKUST-1 crystals, a schematic illustration of the surface-induced oriented growth of $\text{Cu}_3(\text{BTC})_2$ crystals is shown in Figure 4.4.5.

IV. Results and Discussion

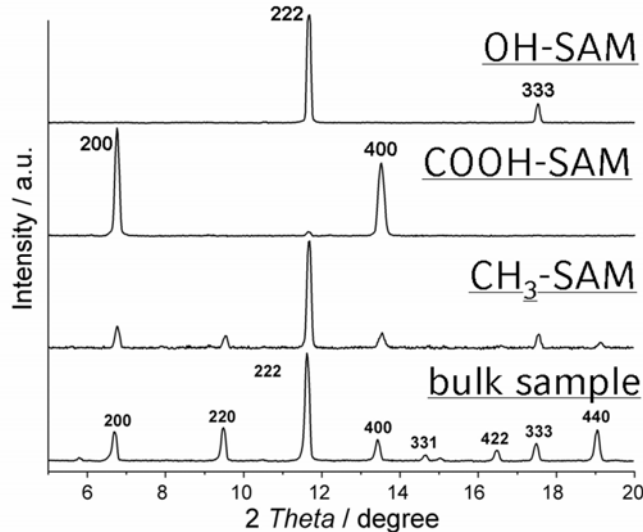


Figure 4.4.4. X-ray diffraction patterns (background corrected) of thin films of $\text{Cu}_3(\text{BTC})_2$ on functionalized gold surfaces, compared with a randomly oriented $\text{Cu}_3(\text{BTC})_2$ powder sample measurement. Each pattern is normalized to the most intensive reflection.

The two different termini of the SAMs (-COOH and -OH) force the oriented attachment of appropriate growth species at the molecular interface, followed by oriented crystal growth on the molecular layer on the substrate.

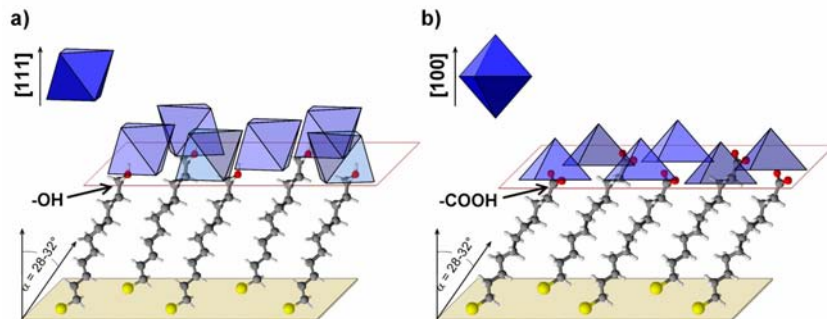


Figure 4.4.5. Schematic illustrations of oriented growth of HKUST-1 nano-crystals controlled via surface-functionalisation: (a) on an 11-mercaptoundecanoic acid SAM, and (b) on 11-mercaptoundecanol-modified gold surfaces. The alkanethiol self-assembled monolayers are represented with a tilt of about 30° from surface normal as reported in the literature. [50]

A close inspection of the respective lattice planes in (100) and (111) direction shows clearly the presence, in both orientations, of planes (cuts) where the Cu₂-units are in-plane oriented, and other cuts shifted by a quarter of a unit cell, where the bimetallic units are tilted 35° for the (100), and 45° for the (111) cut respectively.

IV. Results and Discussion

As shown in Figure 4.4.6, the growth on the COOH-SAM should be in favor of in-plane growth of the Cu₂ units (with radial coordination of the carboxylate group).

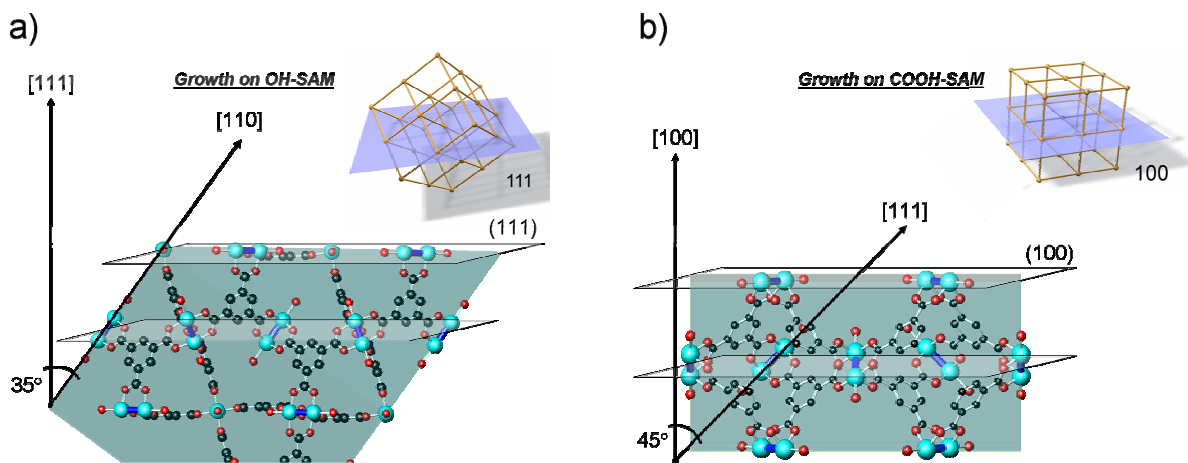


Figure 4.4.6. Schematic illustrations of the respective lattice planes of HKUST-1 in (100) and (111) direction. Crystal cuts perpendicular (a) to the [111]-direction and (b) to the [100]-direction, respectively.

While picture (b) shows that in case of the 100 orientation the in-plane bimetallic units are coordinated by two carboxylate-groups, the 111 direction (Figure 4.4.6a) offers just one coordination per bimetallic-cluster. Thus, statistically the first option should be preferred on a SAM presenting a rather dense population of -COOH groups.

In the case of OH-SAM, which following our hypothesis could mimic the axially coordinating water molecules, a close-to-upright orientation of the paddle-wheel unit with respect to the self-assembled monolayer interface would be expected. Both the [100] and the [111] crystal orientations present planes with tilted Cu₂-units. The [111]-orientation offers Cu₂-units with a tilt of 35° with respect to the vertical, in contrast to the 45° tilt in the [100] case. Taking into account steric factors (crowding by the BTC ligands), in our view this difference could be the deciding factor in favoring the [111]-orientation for the OH-functionalized gold surfaces. After long immersion times (> 100 h), about 600 nm thin films composed of a monolayer of close-packed intergrown crystals are found on all functionalized gold substrates. (Figure 4.4.7) The orientation of the crystals at this stage is difficult to recognize, because the films are composed of a monolayer of close-packed intergrown crystals.

IV. Results and Discussion

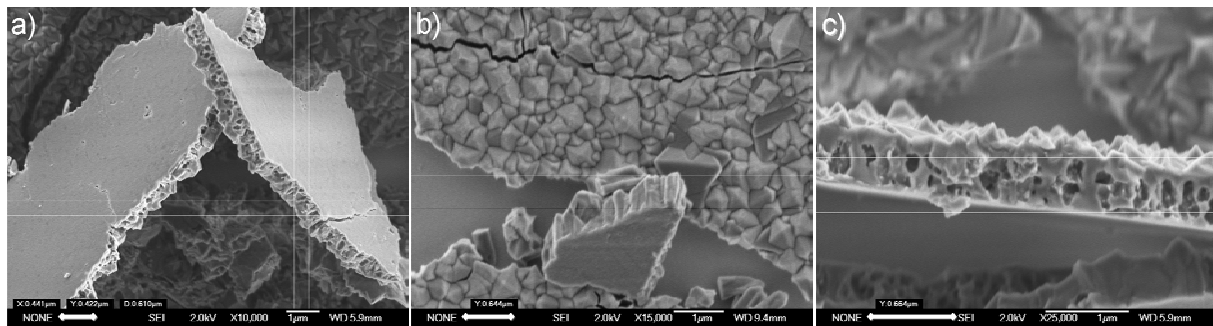


Figure 4.4.7. SEM-pictures of HKUST-1 thin films on 11-Mercapto-1-undecanol-SAM (a), 11-Mercaptoundecanoic acid-SAM (b), and 1-Mercaptoundecan-SAM (c). All samples were measured after equal immersion time (112 h). The thickness was measured directly on the images, and is similar for all the samples (ca. 600 nm). The orientation of the crystals at this stage is difficult to recognize, because the films are composed of a monolayer of close-packed intergrown crystals.

The temporal evolution of the growth process was followed employing X-ray diffraction (in reflection geometry) in order to learn more about the mechanism of formation of the thin films on each modified surface (-OH, -COOH, and -CH₃-terminated SAMs). Scanning electron microscopy confirmed the preferential crystal orientation on the different SAM-functionalized gold surfaces.

The samples were removed from the crystallization solution after different immersion times, dried at RT and characterized. The compared samples where all obtained from the same batch, and different batches are comparable: the difference in the amount of HKUST-1 obtained in different batches is always consistent with variations smaller than 1 %. The original solutions were all prepared in the same way with particular attention to composition, aging time and temperature. Figure 4.4.8a shows the evolution of the diffraction patterns of [111]-oriented Cu₃(BTC)₂ crystals on an OH-SAM, collected after immersion times between 16 and 210 h. The intensity of the reflections increases with the reaction time, because both the number and the size of the crystals on the surface increase. The scanning electron micrographs presented in Figure 4.4.9 show, in detail, the morphological development of the crystals from “rounded” octahedra of 150-200 nm in diameter at the first stages (a) up to 1 µm well-shaped crystals after 45 h (c).

IV. Results and Discussion

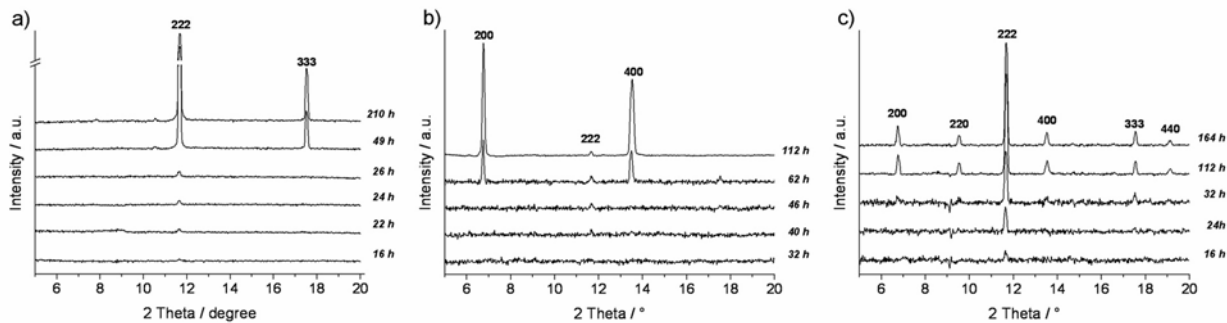


Figure 4.4.8. X-Ray temporal evolution of the growth process: (a) diffraction patterns of [111]-oriented Cu₃(BTC)₂-crystals on OH-SAMs collected after immersion times between 16 and 210 h. b) sample-set relative to the gold-slides modified with the COOH-SAM after immersion times between 32 and 112 h, c) measurements of thin films grown on methyl-functionalized gold surfaces after immersion times between 16 and 164 h.

Analogous results were obtained for the COOH- and CH₃-functionalized samples.

Figure 4.4.8b shows the diffraction patterns of the gold slides modified with the carboxylic acid SAM. After 48 h only the (222)-reflection is detectable, after 64 h both the (200) and the (400)-reflections with comparable intensity are observed and after 112 h the latter completely dominate the pattern.

The morphology of the film after 48 h Figure 4.4.10a reveals that already after 48 h in solution many small [100]-oriented crystals can be detected “growing-out” of the SAM-gold substrate, in addition to a few [111]-oriented crystals which cause the (222)-reflection. The crystals are growing on the COOH surface with the described [100] orientation albeit somewhat more slowly than on the -OH and -CH₃ terminated SAMs. The slower nucleation/growth is related to the more selective coordination of growth species required in this case. The interim detection of the weak (222) reflection on this particular series of samples is attributed to the occasional growth of a small number of [111] oriented crystals – the latter orientation appears to be favorable due to the octahedral morphology of the crystals. Furthermore, the detection of the latter crystals in the XRD is also favored because the (222) reflection is by far the strongest reflection in the diffractogram of Cu₃BTC₂.

The Cu₃BTC₂ crystal layer on the methyl-terminated SAM shows a faster growth process than on the other two polar layers, with no unique orientation (as shown in the SEM pictures presented in Figures 4.4.11). The X-ray diffraction patterns present all typical

IV. Results and Discussion

reflections of $\text{Cu}_3(\text{BTC})_2$, while the (222)-reflection is predominant (Figure 4.4.8c). Thus, the [111]-direction appears to be favored for less selective crystal growth – a possible explanation is that in this case the growth species have already assumed an octahedral shape with {111}-faces that can attach to the surface.

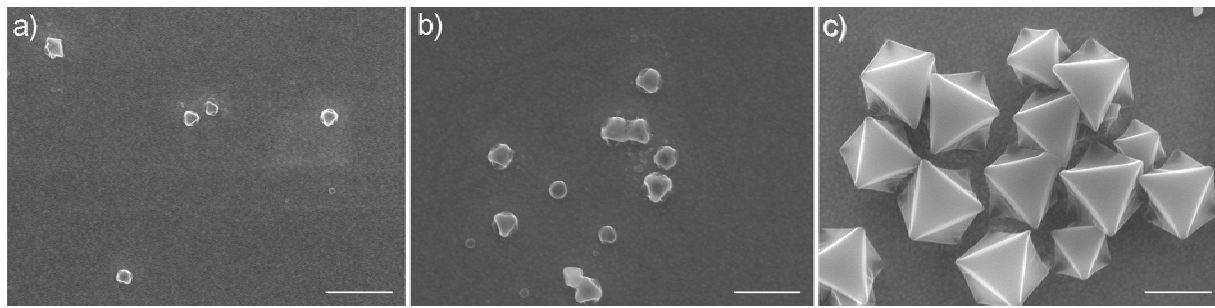


Figure 4.4.9. Scanning electron micrographs of face-down samples of [111]-oriented HKUST-1 grown crystals on OH-SAM modified gold-slides after immersion in the crystallization solution for (a) 16, (b) 24, and (c) 45 hours.

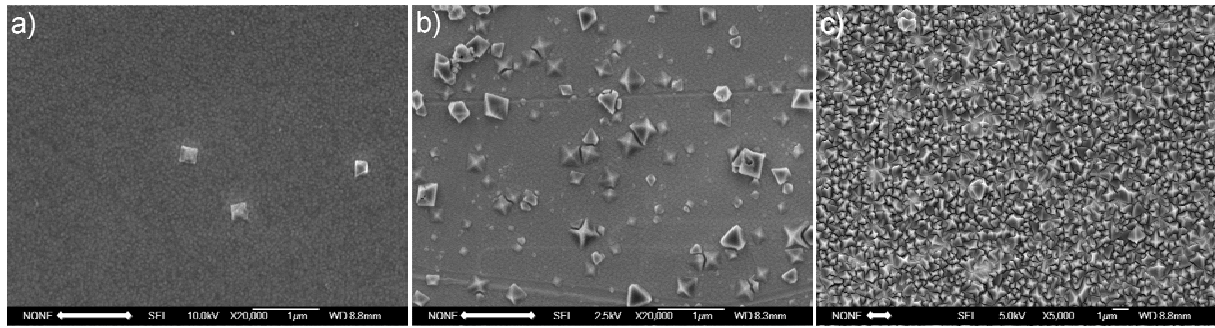


Figure 4.4.10. Scanning electron micrographs of [100]-oriented HKUST-1 grown crystals on COOH-SAM modified gold-slides. The measurements were performed on different samples after immersion times of a) 32 h, b) 40 h and c) 112 h.

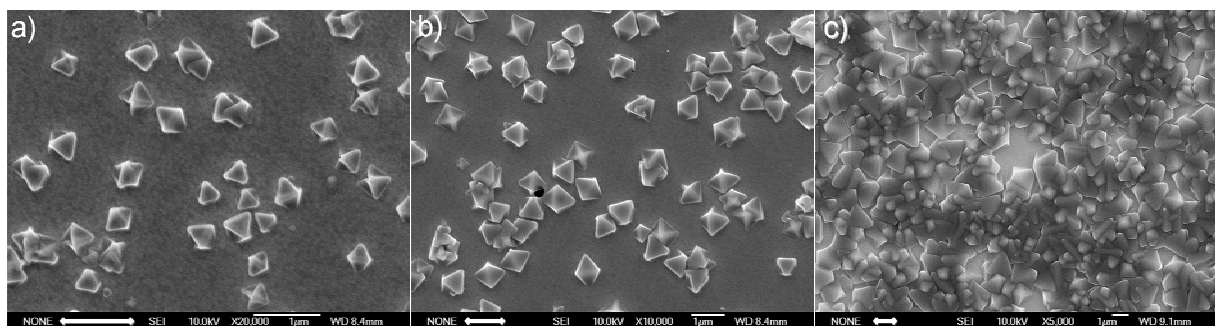


Figure 4.4.11. SEM-pictures of HKUST-1 crystals grown on CH_3 -SAM. No unique orientation can be observed. a) represent a sample immersed for 16 h, while b) show a gold-slide after 24 h crystallization time, and (c) 112 h.

This should constitute a favorable attachment mechanism if dispersive forces between the organically-terminated crystal faces and the alkyl-terminated SAM are dominant. Thus, the non-oriented surface-growth on methyl-functionalized surfaces becomes dominant.

IV. Results and Discussion

Furthermore, non-specific, sterically non-demanding interactions are believed to assist in the faster growth kinetics on these surfaces.

4.4.2. Conclusion

The above results clearly demonstrate that different molecular functionalities of the self-assembled monolayers induce different, well-defined orientations of the Cu₃(BTC)₂ crystals grown on gold. Although the mechanism of this remarkable effect is still unknown, a reasonable model could invoke selective interactions of crystal building blocks in solution with the functionalized surfaces. The thermal pretreatment of the synthesis solution (8 d at 75 °C) induces the crystallization process; after filtration of the solid product the existence of colloidal or molecular building blocks of Cu₃(BTC)₂ in the solution is anticipate. [51] Taking into account the paddle-wheel motif in the open-framework structure, different coordination modes of the carboxylic or the alcoholic groups might control the selective nucleation on the substrate, thus mimicking either axial (as with water) coordination with the alcohol terminus or chelating coordination (as with BTC) with the -COOH terminus of the SAM, respectively.

These result represent the “proof of concept” that by combining structural features of metal-organic frameworks with specific molecular functionalities of the self-assembled monolayers allow tuning the orientation of crystals grown on gold. Noteworthy, the deposition of microcrystalline HKUST-1 under solvothermal conditions on silica surfaces modified with -COOH self assembled silane monolayers has been reported. The [100]-orientation of the crystals is obtained on silica surfaces modified with -COOH self assembled silane monolayers, which is in contrast with the results presented in this thesis. Thus, by direct growth of HKUST-1 at RT on 11-mercaptopoundecanoic acid-SAM [111]-oriented films were obtained. The analysis of these contrasting results must take into account the drastically different conditions under which the experiments were performed. SAMs on silica do not present the same grade of homogeneity as thiol SAMs on gold. [52]

IV. Results and Discussion

Furthermore, under solvothermal conditions (120 °C) the interchain forces which stabilize the self-assembled monolayer are affected. At these conditions the -COOH silane functionalized surface does not present the same features as the thiol-SAM. Thus, the influence on crystals orientation is not comparable.

IV. Results and Discussion

4.5. Direct growth of $\text{Cu}_3(\text{BTC})_2(\text{H}_2\text{O})_3 \cdot x\text{H}_2\text{O}$ thin films on modified QCM-gold electrodes – water sorption isotherms

This section presents how the successful procedure for the direct growth of metal-organic frameworks on functionalized surfaces (Section 4.4) was employed to prepare a thin film of $\text{Cu}_3(\text{BTC})_2(\text{H}_2\text{O})_3 \cdot x\text{H}_2\text{O}$ on the sensing area of an acoustic wave device. Thin films were formed on the gold electrode of a quartz-crystal microbalance (QCM) by direct growth on 11-mercaptoundecanol as well as 11-mercaptoundecanoic acid self-assembled monolayers. A thorough characterization of the HKUST-1 thin film was performed. The formation of a stable and compact thin film, interfacing with an appropriate transducer concept for sensitive detection, allows the characterization of the porous films by means of molecular sorption experiments. Thus, water vapor sorption measurements were performed to collect the sorption isotherms of the thin film grown on the electrode of the QCM-device.

This work was carried out in cooperation with Alexander Darga from the research group of Prof. Bein at LMU, who performed the QCM water vapor sorption measurements. Details about this part of the work may be found in his thesis and in the related publication. [53] The present thesis is focused on the preparation of the thin films, as well as on the characterization with conventional methods (diffraction, vibrational spectroscopy, electron microscopy). The results corresponding to the sorption measurements will be briefly discussed here.

4.5.1 Results and Discussion

In order to achieve direct growth of HKUST-1 thin films on the gold electrodes of a QCM-device, the stepwise synthesis strategy described in Section 2.3.2 was employed. Briefly, a crystalline film of $\text{Cu}_3(\text{BTC})_2(\text{H}_2\text{O})_3 \cdot x\text{H}_2\text{O}$ was prepared directly on SAM-modified gold electrodes of a QCM-device, by immersion of the device in upright position at room

IV. Results and Discussion

temperature for 24 - 48 h in a clear HKUST-1 crystallization solution. (Figure 4.5.1a) Evidence for the formation of the self-assembled monolayers on the QCM gold electrodes was obtained by RAIR spectroscopy, as previously shown in detail (Section 4.4.1).

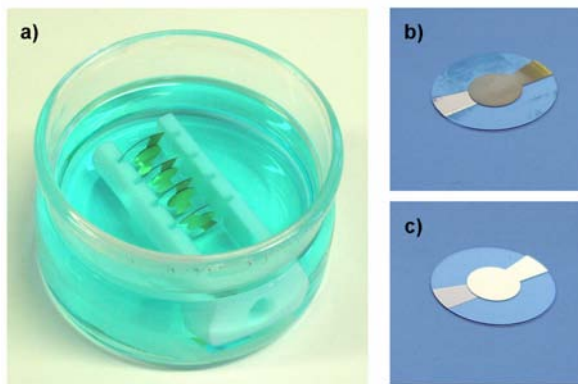


Figure 4.5.1. a) QCM-devices immersed upright in the HKUST-1 crystallization solution. QCM-chip after $\text{Cu}_3(\text{BTC})_2(\text{H}_2\text{O})_3 \cdot x\text{H}_2\text{O}$ growth step: b) opaque layer on the SAM-modified gold electrode; c) reference chip without SAM on the gold surface.

A thin opaque layer of HKUST-1 was visible on the coated gold electrode area; additional crystals present on the quartz surface were easily washed away (Figure 4.5.1b). The reference QCM device (Figure 4.5.1c) without the self-assembled monolayer did not show the formation of any crystalline $\text{Cu}_3(\text{BTC})_2(\text{H}_2\text{O})_3 \cdot x\text{H}_2\text{O}$.

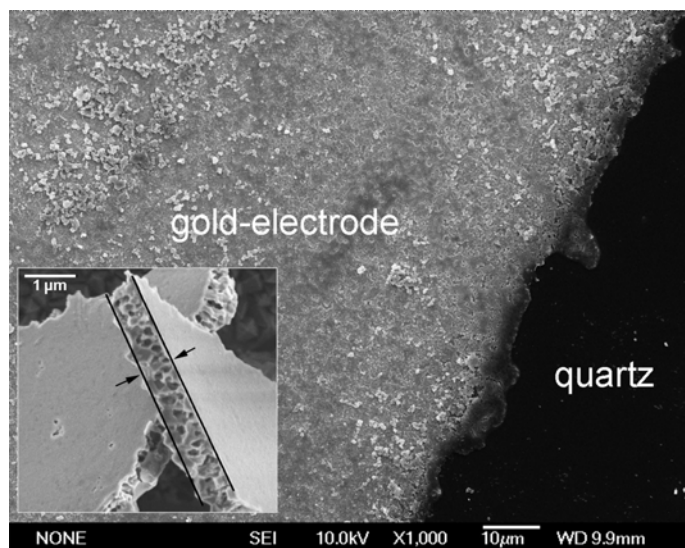


Figure 4.5.2. Scanning-electron micrograph of a thin film of $\text{Cu}_3(\text{BTC})_2$ on the gold electrode of a QCM. The presence of the crystals just on the SAM-functionalized gold surface is evident; no growth is observed on the quartz surface. The film thickness (ca. 600 nm) was directly measured on a scratch of the film, as shown in the enlargement.

IV. Results and Discussion

The scanning electron micrograph (Figure 4.5.2) shows in detail the gold-electrode/quartz boundary on the QCM-device: crystallization takes only place on the unique gold surface of the electrode, and the film is about 600 nm thick, as presented in the inset. X-ray diffraction confirmed the growth of a thin layer of $\text{Cu}_3(\text{BTC})_2(\text{H}_2\text{O})_3 \cdot x\text{H}_2\text{O}$ on the QCM gold-electrode. Figure 4.5.3 show the diffraction pattern of a film grown on a OH-SAM functionalized QCM gold electrode, compared with the theoretical pattern obtained from the crystallographic data of HKUST-1. The measurement was performed over night to enhance the signal to noise ratio. The relative intensities of the reflections demonstrate the preferential orientation of the crystals parallel to the [111] direction, as reported in Section 4.4.1. [26]

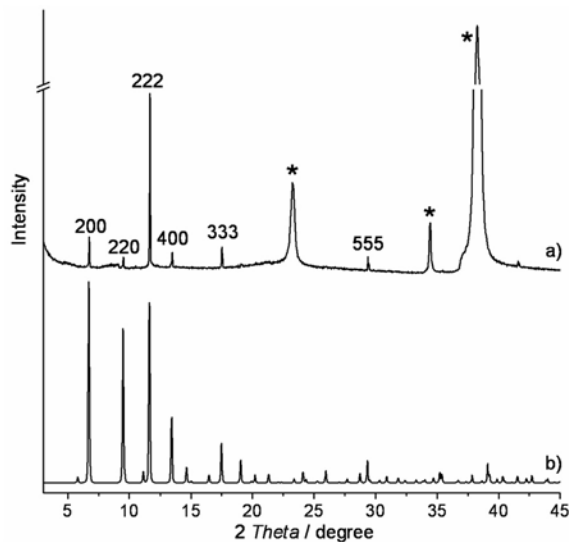


Figure 4.5.3. X-ray diffraction pattern of a thin film of HKUST-1 on a gold substrate (a), and simulated pattern of $\text{Cu}_3(\text{BTC})_2(\text{H}_2\text{O})_3 \cdot x\text{H}_2\text{O}$ (b). The reflections marked with (*) are due to the gold substrate.

The QCMs need to be immersed upright because of the presence of piezoactive electrodes on both faces of the quartz crystal. The potential influence of this geometrical expedient on the orientation of the crystalline film was studied by X-ray diffraction. The tunable orientation is the result of the SAM-functionality, no effect of the immersion geometry was observed (Figure 4.5.4).

The Raman spectra of the as-synthesized HKUST-1 film and the reference powder sample are compared in Figure 4.5.5. The presence of vibrational modes involving the metal

IV. Results and Discussion

species is detectable in the low-frequency region between 600 and 100 cm^{-1} . [54] Many modes associated with the organic part of the $\text{Cu}_3(\text{BTC})_2$ framework are observed.

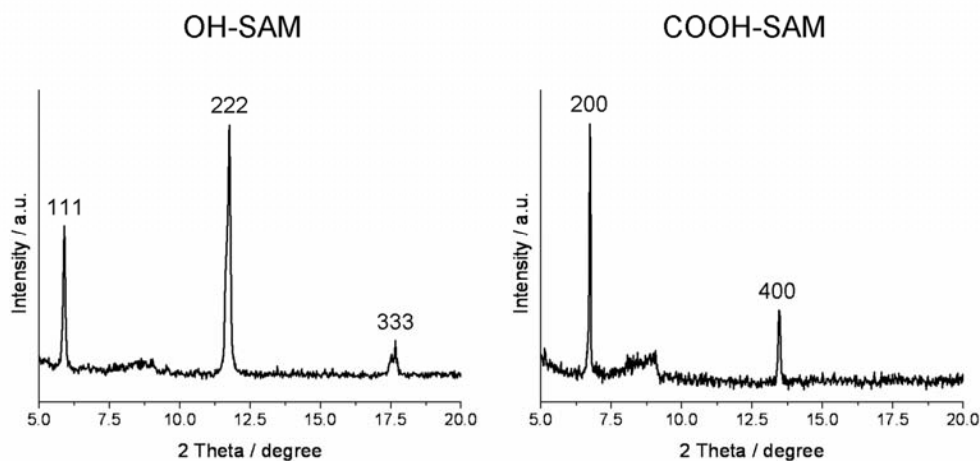


Figure 4.5.4. X-ray diffraction patterns of grown thin films of $\text{Cu}_3(\text{BTC})_2$ on functionalized the gold substrates (Section 2.3.2) positioned upright in the crystallization solution for 64 h.

For example, the bands at 746 and 829 cm^{-1} are due to out-of-plane ring bending vibrations and to out-of-plane ring (C–H) bending modes, respectively. The bands at 1610 and 1006 cm^{-1} are associated with (C=C) stretching modes of the benzene ring; while the ones at 1463 and 1551 cm^{-1} are due to the symmetric and asymmetric stretching of the carboxylate units. [45]

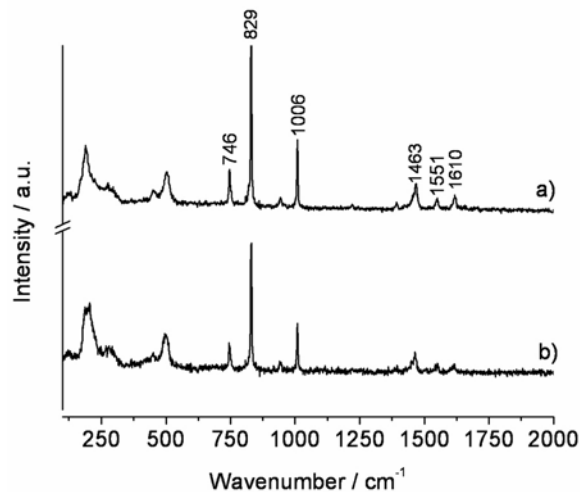


Figure 4.5.5. Raman spectra of $\text{Cu}_3(\text{BTC})_2(\text{H}_2\text{O})_3 \cdot x\text{H}_2\text{O}$, a) bulk sample and b) thin-film grown of a OH-SAM functionalized QCM electrode.

Water sorption in this material is of general interest in the fields of humidity sensing and of heat transformation for climate control, due to the large pore volume and the high

IV. Results and Discussion

framework stability. The study on the sorption properties of water vapor in the metal-organic framework at different temperatures is presented in the following.

The sorption isotherms of water vapors were recorded on grown films of $\text{Cu}_2(\text{BTC})_3$ (film weights between 45 and $71 \cdot 10^{-6} \text{ g cm}^{-2}$). Water sorption measurements were performed at temperatures of 294, 313, 328 and 343 K on a LabView-controlled QCM-sorption system featuring mass flow controllers for the adjustment of vapor streams. The QCM-system is equipped with a fully automatic carrier/analyte flow system for gases and vapors. The relationship between the mass-loading and the frequency-change of the QCM-chip is described by the Sauerbrey equation, as explained in Section 3.4.

A detailed description of the measurement setup as well as the method employed for the calculation of the amount of adsorbed analyte vapor is presented in the related publication. [53] All frequency changes, measured as ΔHz , were recorded when the dynamic adsorption/desorption process had reached the equilibrium conditions. Considering the non-ideality of the adsorptive vapors (water), the partial pressures were corrected considering van-der-Waals behavior.

The water vapor isotherm recorded on the thin film at room temperature (294 K) with the QCM setup is presented in Figure 4.5.6.

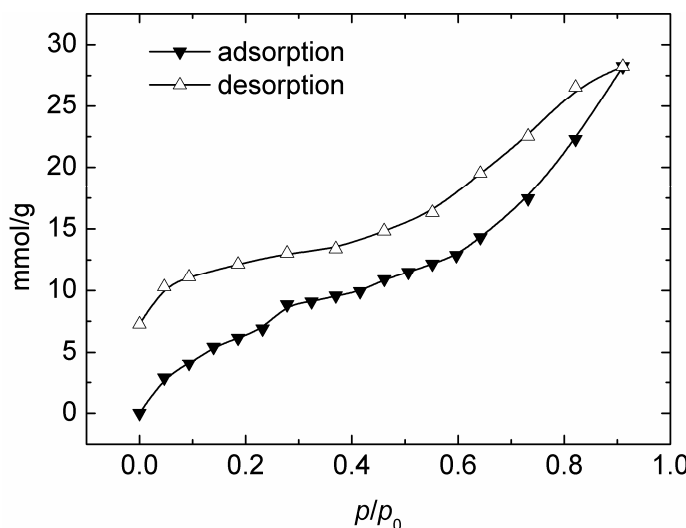


Figure 4.5.6. Water-sorption isotherm on $\text{Cu}_3(\text{BTC})_2$ thin film with the QCM setup recorded at 294 K.

IV. Results and Discussion

The isotherm-shape can be classified as Type I in the IUPAC classification (Figure 3.5a). The adsorption data are confirmed by the data from the TGA measurement. The amount of water adsorbed at $p/p_0 = 0.8$ is approximately 16 mmol g^{-1} , which is in accordance with the TGA data. Thus 16 mmol g^{-1} of water (weight-loss 31 %) are desorbed between room temperature and 130°C . Considering that the bulk sample used for the thermogravimetric analysis was pretreated under an atmosphere of about 80 % relative humidity ($p/p_0 = 0.8$ at $T = 294 \text{ K}$), the two results are consistent.

Thermogravimetric analysis was performed on a dried powder sample of HKUST-1 prepared at the same conditions as the thin film (RT, 296 K).

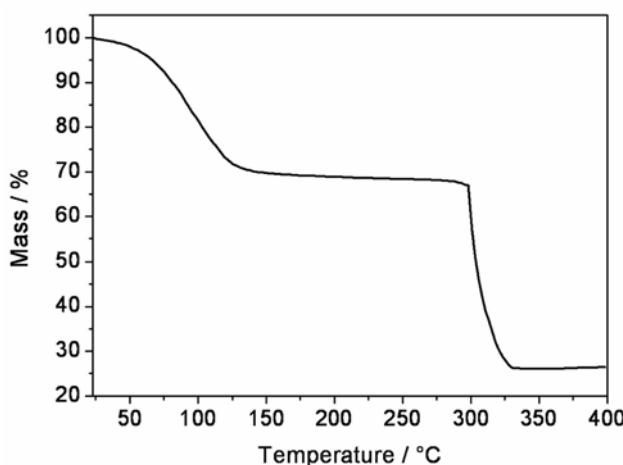


Figure 4.5.7. Thermogravimetric analysis of a bulk sample of $\text{Cu}_3(\text{BTC})_2(\text{H}_2\text{O})_3 \cdot x\text{H}_2\text{O}$ in synthetic air flow ($50 \text{ cm}^3 \text{ min}^{-1}$), with a heating rate of $10^\circ\text{C min}^{-1}$. The film was pre-saturated in water atmosphere ($\approx 80\%$ RH) for 48 h.

The sample was exposed to an atmosphere with relative humidity of 80 % ($p/p_0 = 0.8$) at RT (294 K) for 48 h. These humidity conditions were reached in a closed dessicator containing a saturated NH_4Cl solution. [55] The thermogravimetric diagram (Figure 4.5.7) shows a first weight loss of 31 % between room temperature and 150°C . This weight loss can be assigned to the removal of the H_2O molecules present in the channels and coordinated to the metal centers of the MOF-structure, which corresponds to about 16 mmol g^{-1} . The dehydrated framework ($\text{Cu}_3(\text{BTC})_2$) is thermally stable up to 300°C in synthetic air. In the next step ($300 - 330^\circ\text{C}$), a weight loss of 43 % (63 % referred to dry $\text{Cu}_3(\text{BTC})_2$) is detectable that corresponds to the oxidative degradation of the two organic linker

IV. Results and Discussion

molecules per formula unit (theoretical weight loss from dry $\text{Cu}_3(\text{BTC})_2$: 64.6 %). A further increase of the temperature, above 350 °C, leads to the final formation of Cu_2O . These results were confirmed by powder X-ray diffraction (Figure 4.5.8).

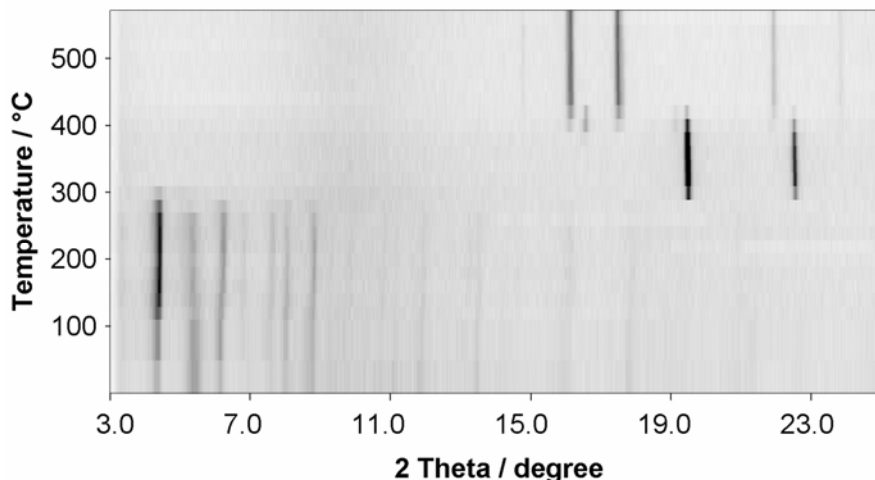


Figure 4.5.8. XRD patterns of HKUST-1 collected between 20 and 560 °C, at intervals of 20 °C. The heating rate in between the measurements was 50 °C min⁻¹ with a temperature holding time before each acquisition of 45 min. The measurement were collected using Mo $K\alpha$ radiation ($\lambda = 71.073 \text{ pm}$).

Temperature dependent X-ray diffraction provides interesting information on the thermal behavior of the metal-organic framework and its structural stability at elevated temperatures. As shown in Figure 4.5.8, only small changes in the intensities of the diffraction peaks are observed up to 300 °C. This, information in combination with the TGA data, confirms that the three-dimensional framework structure is maintained, and only the guest-molecules in the pores are removed. At higher temperature the rapid decomposition to CuO can be observed, which is stable up to temperatures around 420 °C. Further heating of the sample leads to the formation of Cu_2O .

Figure 4.5.9 shows the isotherms recorded at 313, 328, 343 and 358 K respectively. The difference between the adsorption and the desorption branches decreases with the increase of the measurement temperature up to 328 K and disappear completely at 343 K. Apparently equilibrium is reached faster at higher temperature. Thus a full reversibility of the sorption process can be observed for measurement at about 343 K. All measurements were collected at equilibrium conditions for the adsorption branch; while the desorption (a much slower process) data were collected at the delay-time limit of the analytical system

IV. Results and Discussion

(measurement-step duration of 4 h). The partial pressure of the analyte was increased in sequential steps and the corresponding frequency shifts were recorded. The measurements, especially at higher temperatures, are subjected to frequency fluctuations (heater fluctuations) and to the flow-controller fluctuations (< 0.1%) of the corresponding MFC. In the analytical setup employed in this study, the frequency stabilizes and is constant over 16.000 measurement points, corresponding to more than four hours. However, the desorption of water at RT takes even longer compared to the adsorption process which is reflected in the observed discrepancy between the adsorption and desorption branches (non-closing isotherms).

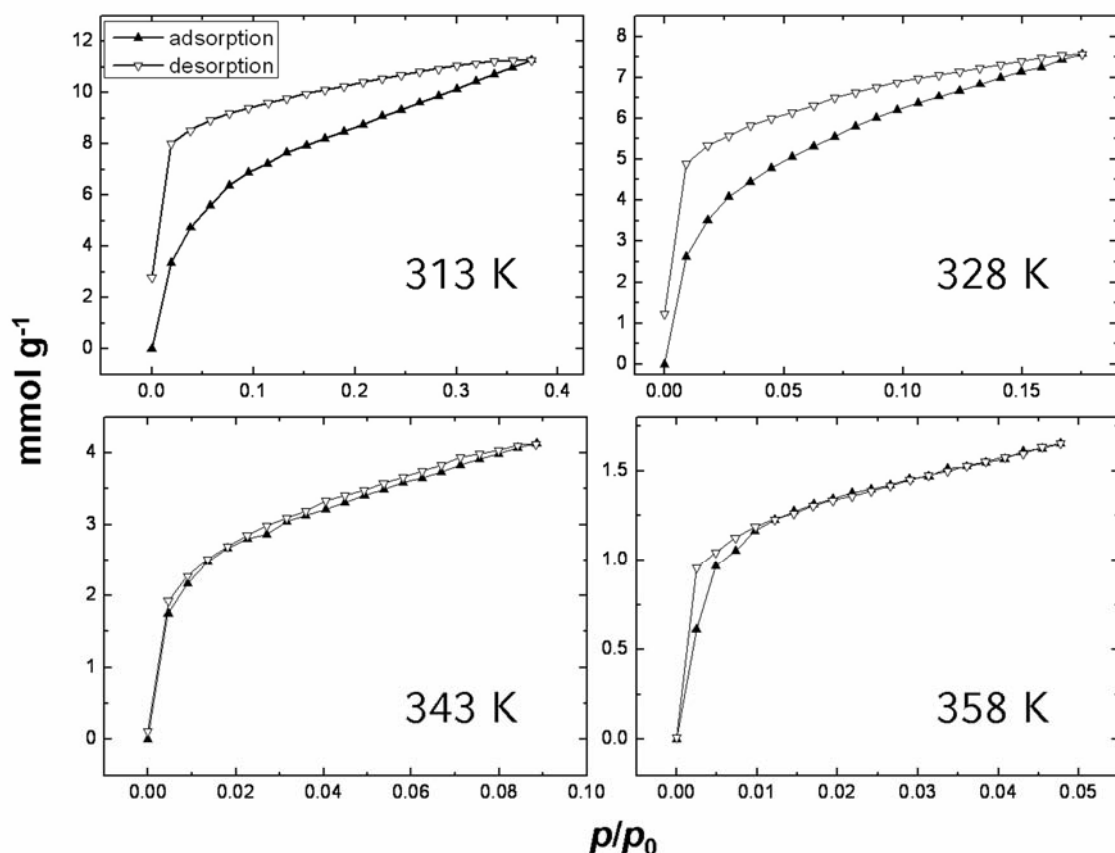


Figure 4.5.9. Water-sorption isotherms of a thin film of $\text{Cu}_3(\text{BTC})_2$ collected at 313 (a), 328 (b), 343 (c) and 358 K (d) respectively.

Due to structural features of the metal-organic framework HKUST-1, presenting a 3D cubic porous system, the sorption data collected on different oriented samples didn't differ substantially. Thus, the accessibility of the pore system is equivalent.

IV. Results and Discussion

4.5.2 Conclusion

The selective growth of thin films of the metal-organic framework $\text{Cu}_3(\text{BTC})_2(\text{H}_2\text{O})_3 \cdot x\text{H}_2\text{O}$ on the functionalized gold electrodes of a QCM device was successfully achieved. The tunable orientation of the metal-organic framework on the QCM- electrodes was confirmed for the up-right geometry. The nature of the film was fully characterized by X-ray diffraction, Raman spectroscopy, and scanning-electron microscopy. The direct growth of the MOF layer on the gold electrodes of a QCM device allowed us to evaluate the sorption properties of the MOF thin film representing a very small amount of the porous material (with sample weights per cm^2 ranging from 45 to 71 μg).

Water sorption isotherms were recorded at different temperatures. The adsorption and the desorption data corresponding to the lower temperatures do not overlap as expected at equilibrium conditions. This discrepancy decreases with the increase of the measurement temperature up to 328 K and disappear completely at 343 K. Equilibrium is reached faster at higher temperature, and a full reversibility of the sorption process can be observed for measurements performed at temperatures higher than 328 K. The combination of a well known transducer concept as the acoustic wave device with a relative new class of porous materials offer a solid technique for the investigation of sensitive molecular sorption. Thus, these results are promising for the design of selective sensors based on metal-organic frameworks.

IV. Results and Discussion

References

- [1] K. A. Marx, *Biomacromolecules* 4 (2003) 1099.
- [2] C. K. O'Sullivan, G. G. Guilbault, *Biosensors & Bioelectronics* 14 (1999) 663.
- [3] I. I. Postinkov, *Acoustical Physics* 40 (1994) 586.
- [4] R. Schumacher, *Angew. Chem.* 102 (1990) 347.
- [5] C. A. Fyfe, Y. Feng, H. Grondy, G. T. Kokotailo, H. Gies, *Chem. Rev.* 91 (1991) 1525.
- [6] J. Klinowski, *Chem. Rev.* 91 (1991) 1459.
- [7] M. Templin, U. Wiesner, H. W. Spiess, *Adv. Mater.* 9 (1997) 814.
- [8] M. J. Wirth, R. W. P. Fairbank, H. O. Fatunmbi, *Science* 275 (1997) 44.
- [9] M. K. Ferguson, E. R. Low, J. R. Morris, *Langmuir* 20 (2004) 3319.
- [10] V. L. Furer, *Zh. Prikl. Spektrosk.* 53 (1990) 270.
- [11] G. Socrates: *Infrared and Raman Characteristic Group Frequency*, John Wiley & Sons, Chichester, UK, 2001.
- [12] D. W. Breck: *Zeolite Molecular Sieves: Structure, Chemistry, and Use*, Wiley and Sons, London, 1974.
- [13] R. Szostak: *Molecular Sieves: Principles of Synthesis and Identification*, Van Nostrand Reinhold Catalysis Series, New York, 1989.
- [14] S. Bauer, N. Stock, *Angew. Chem. Int. Ed.* 46 (2007) 6857.
- [15] P. M. Forster, N. Stock, A. K. Cheetham, *Angew. Chem. Int. Ed.* 44 (2005) 7608.
- [16] N. Stock, T. Bein, *Angew. Chem. Int. Ed.* 43 (2004) 749.
- [17] K. Choi, D. Gardner, N. Hilbrandt, T. Bein, *Angew. Chem. Int. Ed.* 38 (1999) 2891.
- [18] J. Klein, C. W. Lehmann, H.-W. Schmidt, W. F. Maier, *Angew. Chem. Int. Ed.* 37 (1999) 3369.
- [19] H. Li, M. Eddaoudi, M. O'Keeffe, M. Yaghi, *Nature* 402 (1999) 276.
- [20] S. S. Y. Chui, S. M. F. Lo, J. P. H. Charmant, A. G. Orpen, I. D. Williams, *Science* 283 (1999) 1148.
- [21] J. W. P. Hsu, Z. R. Tian, N. C. Simmons, C. M. Matzke, J. A. Voigt, J. Liu, *Nano Lett.* 5 (2005) 83.
- [22] S. Hausdorf, F. Baitalow, J. Seidel, F. O. R. L. Mertens, *J. Phys. Chem. A* 111 (2007) 4259.
- [23] T. Loiseau, H. Muguerra, G. Ferey, M. Haouas, F. Taulelle, *J. Solid State Chem.* 178 (2005) 621.
- [24] E. Biemmi, T. Bein, N. Stock, *Solid State Sci.* 8 (2006) 363.
- [25] K. Schlichte, T. Kratzke, S. Kaskel, *Microporous Mesoporous Mater.* 73 (2004) 81.
- [26] E. Biemmi, C. Scherb, T. Bein, *J. Am. Chem. Soc.* 129 (2007) 8054.

IV. Results and Discussion

- [27] C. N. R. Rao, S. Natarajan, R. Vaidhyanathan, *Angew. Chem. Int. Ed.* 43 (2004) 1466.
- [28] A. Thirumurugan, C. N. R. Rao, *J. Mater. Chem.* 15 (2005) 3852.
- [29] M. Eddaoudi, J. Kim, N. Rosi, D. Vodak, J. Wachter, M. O'Keeffe, M. Yaghi Omar, *Science* 295 (2002) 469.
- [30] N. L. Rosi, J. Eckert, M. Eddaoudi, D. T. Vodak, J. Kim, M. O'Keeffe, O. M. Yaghi, *Science* 300 (2003) 1127.
- [31] H. Li, M. Eddaoudi, T. L. Groy, O. M. Yaghi, *J. Am. Chem. Soc.* 120 (1998) 8571.
- [32] H. Li, C. E. Davis, T. L. Groy, D. G. Kelley, O. M. Yaghi, *J. Am. Chem. Soc.* 120 (1998) 2186.
- [33] Z. Otwinowski, W. Minor, *Methods Enzymol.* 276 (1997) 307.
- [34] SCHELXTL, X-ray Syngle Crystal Analysis System, Version 5.1. Brucker, AXS, Madison, WI, 1998.
- [35] L. Xie, S. Liu, B. Gao, C. Zhang, C. Sun, D. Li, Z. Su, *Chem. Commun.* (2005) 2402.
- [36] W. Chen, J. Y. Wang, C. Chen, Q. Yue, H. M. Yuan, J. S. Chen, S. N. Wang, *Inorg. Chem.* 42 (2003) 944.
- [37] M. Eddaoudi, H. Li, O. M. Yaghi, *J. Am. Chem. Soc.* 122 (2000) 1391.
- [38] M. Edgar, R. Mitchell, A. M. Z. Slawin, P. Lightfoot, P. A. Wright, *Chem. Eur. J.* 7 (2001) 5168.
- [39] J. Aizenberg, A. J. Black, G. M. Whitesides, *J. Am. Chem. Soc.* 121 (1999) 4500.
- [40] F. C. Meldrum, J. Flath, W. Knoll, *J. Mater. Chem.* 9 (1999) 711.
- [41] D. Wang, J. Liu, Q. Huo, Z. Nie, W. Lu, R. E. Williford, Y.-B. Jiang, *J. Am. Chem. Soc.* 128 (2006) 13670.
- [42] B. C. Bunker, P. C. Rieke, B. J. Tarasevich, A. A. Campbell, G. E. Fryxell, G. L. Graff, L. Song, J. Liu, J. W. Virden, G. L. McVay, *Science* 264 (1994) 48.
- [43] S. Feng, T. Bein, *Nature* 368 (1994) 834.
- [44] J. S. Lee, Y.-J. Lee, E. L. Tae, Y. S. Park, K. B. Yoon, *Science* 301 (2003) 818.
- [45] C. Prestipino, L. Regli, J. G. Vitillo, F. Bonino, A. Damin, C. Lamberti, A. Zecchina, P. L. Solari, K. O. Kongshaug, S. Bordiga, *Chem. Mater.* 18 (2006) 1337.
- [46] A. Mahapatro, D. M. Johnson, D. N. Patel, M. D. Feldman, A. A. Ayon, C. M. Agrawal, *Langmuir* 22 (2006) 901.
- [47] I. Engquist, M. Lestelius, B. Liedberg, *Langmuir* 13 (1997) 4003.
- [48] N. Wade, B. Gologan, A. Vincze, R. G. Cooks, D. M. Sullivan, M. L. Bruening, *Langmuir* 18 (2002) 4799.
- [49] L. Bertilsson, B. Liedberg, *Langmuir* 9 (1993) 141.
- [50] J. C. Love, L. A. Estroff, J. K. Kriebel, R. G. Nuzzo, G. M. Whitesides, *Chem. Rev.* 105 (2005) 1103.

IV. Results and Discussion

- [51] F. Taulelle, M. Haouas, C. Gerardin, C. Estournes, T. Loiseau, G. Ferey, *Colloids Surf., A* 158 (1999) 299.
- [52] A. Ulman, *Chem. Rev.* 96 (1996) 1533.
- [53] E. Biemmi, A. Darga, T. Bein, *Microporous Mesoporous Mater.* (2007) submitted.
- [54] P. L. Holland, C. J. Cramer, E. C. Wilkinson, S. Mahapatra, K. R. Rodgers, S. Itoh, M. Taki, S. Fukuzumi, L. Que, Jr., W. B. Tolman, *J. Am. Chem. Soc.* 122 (2000) 792.
- [55] *Handbook of Chemistry and Physics*, CRC Press, 2004-2005.

V. Conclusion

V. Conclusion

Conclusion

The aim of this thesis is the formation of stable and compact thin films, interfacing with an appropriate transducer concept for molecule-selective detection. Layers of periodic porous materials on piezoelectric devices such as a quartz crystal microbalance (QCM) or a surface-acoustic-wave device can impart molecular selectivity to the sorption response. [1]

One class of porous materials used in this study involves zeolites. Many types of stable zeolites with different pore geometries and topologies can be synthesized, thus providing a large variety of different sorption behaviors. The other class of materials used here comprises metal organic frameworks (MOFs). MOFs are crystalline porous materials made by combining metal ions and organic ligands into extended networks. Both MOF and zeolite structures are promising candidates for the design of chemically selective layers.

Two types of strategies were explored for the formation of thin porous films on different substrates, including sensor transducers such as the QCM, i.e., “post-synthetic crystal attachment” and “direct growth”. To obtain a self-limiting monolayer of zeolite nano-crystals, the “post-synthetic crystal attachment” approach based on the molecular attachment of preformed porous nano-crystals was used in this study. [2] The crystals are chemically attached to gold by covalent bonding using appropriate organic self-assembled monolayers (SAM).

On the other hand, direct growth was successfully applied to prepare thin films of porous open-framework copper 1,3,5-benzenetricarboxylate (BTC , $\text{Cu}_3(\text{BTC})_2(\text{H}_2\text{O})_3 \cdot x\text{H}_2\text{O}$) on functionalized self-assembled monolayers on gold. The influence of different functionalized gold-surfaces on the orientation and morphology of the crystalline thin MOF films was investigated. The porous thin films on piezoelectric devices were also investigated with respect to their sorption behavior towards small molecules from the vapor phase.

V. Conclusion

In the course of this work, nano-sized zeolite crystals with ZSM-5 and LTA framework structures were synthesized as stable colloidal suspensions, and were used as building blocks for the assembly of porous films on the gold electrodes of QCM devices. The preparation of the thin films was achieved either by reaction of the as-synthesized nano-crystals with isocyanate-SAM functionalized gold surfaces; or by assembly of thiol-modified zeolite nano-particles on bare gold. Each step of the assembly strategies was fully characterized with different analytical techniques. Both procedures lead to the formation of a nano-crystal monolayer: higher coverage was obtained on the SAM-modified gold, where the ordered compact nature of the organic layer assures an ideal functional surface for the reaction with the free OH-groups of the zeolite crystal surface. The formation of a thin layer by direct functionalization of the zeolite nano-particles, even though slightly lower coverage was achieved, presents a promising starting point for further studies such as pin-printing applications of the zeolite crystal suspension serving as functional ink. Sorption isotherms of n- and i-butane were derived from frequency changes of a quartz crystal microbalance. The data collected at 296 K confirm that the response behavior of the zeolite-based piezoelectric sensor depends on the framework structure as well as on size and shape of the analyte molecule. Selective sorption of n-butane in the LTA-type structure was demonstrated, confirming the capability of producing a molecular sensor able to recognize and discriminate molecules within 1 Å.

In this thesis we demonstrate the efficiency of employing high-throughput methods to understand the influence of process and compositional parameters on the synthesis of metal organic frameworks. [3-7]

It was shown that compositional as well as process parameters can have a decisive influence on the morphology as well as the phase purity of metal organic frameworks. The understanding of these parameters is of crucial importance for applications and for industrial production, respectively. For both MOF-5 and HKUST-1, the choice of the metal salt has an enormous effect on the phase purity as well as the product morphology. In

V. Conclusion

particular, the influence of acetate anion as counter-ion is remarkable. When starting from metal acetates smaller crystals are obtained, a possible explanation is a change in the nucleation rate of the crystallization process. Thus, higher nucleation rate is usually responsible for a larger number of crystals having a smaller size. Whereas in the synthesis of MOF-5 the increase in the pH of the reaction media due to the presence of acetate does not lead to by-products, regarding the synthesis of HKUST-1, the formation of an additional unknown phase is observed. Unexpectedly in both systems no solid products have been obtained employing chloride salts under the conditions investigated. This might be due to differences in solubility or complexation properties of the Cl^- ions. In the case of HKUST-1, an influence of the metal salt on the product formation is only observed at higher temperatures.

The influence of co-solvents on the formation of MOF-5 was explored employing $\text{Zn}(\text{NO}_3)_2 \cdot 6\text{H}_2\text{O}$, as well as ZnO . The formation of the metal organic framework is sensitive to the presence of aromatic co-solvents. Thus, with decreasing polarity of the reaction medium less MOF-5 is formed in favor of other unknown phases. However, the chosen salt plays an important role: the mixture starting from ZnO leads to the formation of the desired compounds at any N,N -diethylformamide/co-solvent ratio.

The addition of small amounts of H_3O^+ or OH^- and water to the synthesis mixture of MOF-5 leads to the formation of two different compounds. While $\text{Zn}_3(\text{OH})_2(\text{BDC})_2 \cdot 2\text{DEF}$ is obtained under alkaline condition, the presence of H_3O^+ ions and water favor the formation of $(\text{H}_2\text{N}(\text{Et})_2)_2[\text{Zn}_3(\text{BDC})_4] \cdot 3\text{DEF}$. With the help of high-through put (HT) experiments, clear reaction trends could be identified.

Furthermore, by understanding the influence of different parameters on the formation of MOFs, the synthesis procedure for HKUST-1 has been optimized. Cu_2O free samples were obtained by decreasing the reaction temperature to 348 K; and the systematic investigation of the synthesis time shows that after 320 h a maximum yield is achieved. The size and the morphology of the HKUST-1 crystals could be controlled by varying the concentration of the starting mixture.

V. Conclusion

The structure of the zinc terephthalate $(H_2NEt_2)_2[Zn_3(BDC)_4] \cdot 3DEF$, synthesized during the HT-screening, was determined by single crystal X-ray diffraction and fully characterized. The open framework consists of trimetallic zinc units interconnected by mono- and bidentate terephthalate ligands to form dense layers in the b,c -plane. These layers are bridged along the a -direction by monodentate BDC groups. Thus, a 2D porous framework is formed. The possible removal of the guest-molecules from the pores has been demonstrated employing TGA data in combination with the temperature-dependent X-ray analysis as well as vibrational spectroscopy and elemental analysis. The crystalline phase formed after temperature treatment above 250 °C is stable up to 400 °C. Thus, free pores are present in the framework, which was demonstrated by sorption measurements.

The results concerning the direct growth of metal-organic frameworks on self-assembled monolayers clearly demonstrate that different molecular functionalities induce different, well-defined orientations of the HKUST-1 crystals grown on gold. The mechanism could involve selective interactions of crystal building blocks in solution with the functionalized surfaces. The thermal pretreatment of the synthesis solution induces the crystallization process; thus, after filtration of the solid product the existence of colloidal or molecular building blocks of $Cu_3(BTC)_2$ in the solution can be anticipate. [8] Taking into account the paddle-wheel motif in the open-framework structure, different coordination modes of the carboxylic or the alcoholic groups might control the selective nucleation on the substrate, thus mimicking either axial (as with water) coordination with the alcohol terminus or chelating coordination (as with BTC) with the -COOH terminus of the SAM, respectively.

The strategy of selective growth of metal organic framework developed in this thesis permitted the preparation of $Cu_3(BTC)_2(H_2O)_3 \cdot xH_2O$ thin films on QCM devices. Thus, the sorption properties of the MOF thin film have been directly estimated. Water sorption in this microporous material has been studied in relation to the applications in the field of humidity sensing as well as heat transformation. Sorption isotherms were recorded at different temperatures.

V. Conclusion

These successful results on the production of thin porous oriented films opens new perspectives for potential applications of metal-organic frameworks, such as selective separation membranes [9] or for sensor applications.

References

- [1] S. Mintova, B. Schoeman, V. Valtchev, J. Sterte, S. Mo, T. Bein, *Adv. Mater.* 9 (1997) 585.
- [2] K. B. Yoon, *Acc. Chem. Res.* 40 (2007) 29.
- [3] S. Bauer, N. Stock, *Angew. Chem. Int. Ed.* 46 (2007) 6857.
- [4] P. M. Forster, N. Stock, A. K. Cheetham, *Angew. Chem. Int. Ed.* 44 (2005) 7608.
- [5] N. Stock, T. Bein, *Angew. Chem. Int. Ed.* 43 (2004) 749.
- [6] K. Choi, D. Gardner, N. Hilbrandt, T. Bein, *Angew. Chem. Int. Ed.* 38 (1999) 2891.
- [7] J. Klein, C. W. Lehmann, H.-W. Schmidt, W. F. Maier, *Angew. Chem. Int. Ed.* 37 (1999) 3369.
- [8] F. Taulelle, M. Haouas, C. Gerardin, C. Estournes, T. Loiseau, G. Ferey, *Colloids Surf., A* 158 (1999) 299.
- [9] M. Arnold, P. Kortunov, D. J. Jones, Y. Nedellec, J. Kaerger, J. Caro, *Eur. J. Inorg. Chem.* (2007) 60.

VI. Appendix

VI. Appendix

List of Abbreviations

2D	Two-Dimensional
3D	Three-Dimensionall
AC	Alternating Current
Anal.	Analitical
BDC	1,4-Benzendicarboxylate
BET	Brunauer Emmett and Teller
BSE	Back Scattered Electrons
BTC	1,3,5-Benzentricarboxylate
Calcd.	Calculated
CP	Cross Polaristaon
CSA	Chemical Shift Anisotropy
DEF	<i>N,N</i> -Diethylformamide
DFT	Density Functional Theory
DIC-4	Diisocyanatebutane
DLS	Dynamic Light Scattering
DMF	<i>N,N</i> -Dimethylformamide
DSC	Differential Scanning Calorimetry
EDX	Energy Dispersive X-ray (analysis)
FT	Fourier Transformation
HKUST-1	Hong-Kong University Structure 1 → Cu ₃ (BTC) ₂ (H ₂ O) ₃ ·XH ₂ O
HR	High Resolution
HT	High-Throughput
IR	Infrared
IRMOF	Isoreticular Metal-Organic Framework
IUPAC	International Union Of Pure And Applied Chemistry
LTA	Linde Type A
MAS	Magic Angle Spinning
MFC	Mass Flow Controller
MFI	Acronym Defining The Framework Type Of Important Zeolites, E.G., Silcalite-1 (S-1), Zsm-5, Titanium Silicalite-1 (Ts-1), According To The Rules Of International Zeolite Association (Iza).
MIL	Matériaux de l'Institut Lavoisier
MOF	Metal-organic Framework
MOF-5	Metal-organic Framework 5 → Zn ₄ O(BDC) ₃ ·(DMF) ₈ (C ₆ H ₅ Cl)
MPS	3-Mercaptopropyltrimethoxysilane

VI. Appendix

NMR	Nuclear Magnetic Resonance
QCM	Quartz Crystal Microbalance
RAIRS	Reflection Absorption Infrared Spectroscopy
rf	radio frequency
RT	Room Temperature
SAM	Self Assembled Monolayers
SAW	Surface Acoustic Wave
SBU	Secondary Building Unit
SE	Secondary Electrons
SEM	Scanning Electron Microscopy
SP	Single Pulse
STP	Standard Temperature and Pressure
TEM	Transmission Electron Microscopy
TGA	Thermogravimetric Analysis
TMA(OH)	Tetramethylammonium hydroxide
TPA(OH)	Tetrapropylammonium hydroxide
UHV	Ultra High Vacuum
XRD	X-Ray Diffraction
ZSM-5	Zeolithe Socony Mobil 5

VI. Appendix

Curriculum Vitae Enrica Biemmi

Persönliche Angaben

Nationalität: Italienisch
Geburtsdatum: 23. Oktober 1975
Geburtsort: Gavardo (BS), Italien
Familienstand: ledig

Ausbildung

- 10/2002 – 6/2007 Ludwig-Maximilians-Universität, München
Promotion in Physikalischer Chemie (Prof. Dr. T. Bein)
Thema: Synthese und Charakterisierung funktioneller Beschichtungen von Glas-, Halbleiter-, und Metalloberflächen mit porösen nanostrukturierten Materialien für die Entwicklung von Sensoren
- 09/1994 – 05/2002 Università degli Studi di Milano, Mailand, Italien
Studium der Industriechemie
Schwerpunkte: physikalische und analytische Chemie anorganischer Materialien
- 02/2001 – 05/2002 Directorate General Joint Research Centre (EC), Ispra (VA), Italien
Diplomarbeit & praktische Ausbildung
Thema: Optimierung eines Überwachungsprozesses von wassergefährdenden Stoffen mit Hilfe der chemischen Fluoreszenzanalyse
(Gesamtnote 104/110)

Schulbildung

- 09/1989 – 07/1994 Liceo Scientifico Statale A. Calini, Brescia, Italien
Diploma di Maturità Scientifica
Gymnasialabschluss (Gesamtnote 46/60)

Berufserfahrung

- 07/2007 – heute Rodenstock GmbH, F&E Optische Polymere und Gläser, München
Entwicklung von Lackbeschichtungen

Auszeichnungen

- 07/ 2006 Shortlisted für "The Royal Microscopical Society Micrograph Competition 2006"
- 10/ 2002 – 10/2004 Stipendium der "Università degli Studi di Milano" und der Europäischen Union für Forschung außerhalb Italiens

München, 27.01.2008



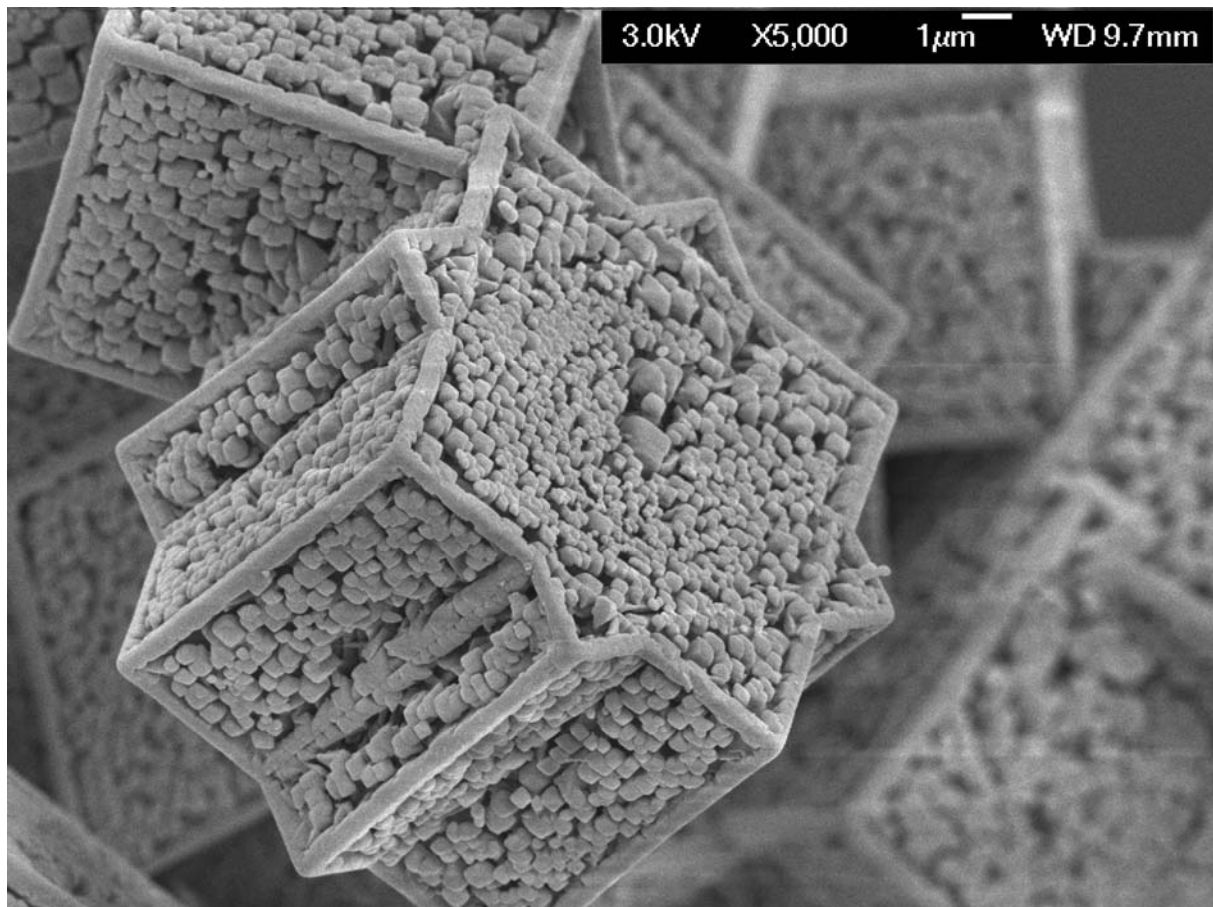
Enrica Biemmi

VI. Appendix

Publications and Presentations

- Publications**
- E. Biemmi, C. Scherb, T. Bein "Oriented Growth of the Metal Organic Framework $\text{Cu}_3(\text{BTC})_2(\text{H}_2\text{O})_3 \cdot x\text{H}_2\text{O}$ Tunable with Functionalized Self-Assembled Monolayers" *J. Am. Chem. Soc.* 129 (2007) 8054
- E. Biemmi, T. Bein, N. Stock, "Synthesis and characterization of a new metal organic framework structure with 2D porous system: $(\text{H}_2\text{NEt}_2)_2[\text{Zn}_3(\text{BDC})_4] \cdot 3\text{DEF}$ " *Solid State Sci.* 8 (2006) 363
- E. Biemmi, T. Bein, "Assembly of nanozeolite monolayers on the gold substrates of piezoelectric sensors" (2007) submitted (*Langmuir*)
- E. Biemmi, S. Christian, T. Bein, N. Stock, "Screening of synthesis parameters in the formation of the metal-organic frameworks MOF-5 and HKUST-1 employing HT-methods" (2007) submitted (*Microporous Mesoporous Mater.*)
- E. Biemmi, A. Darga, N. Stock, T. Bein, "Direct growth of $\text{Cu}_3(\text{BTC})_2(\text{H}_2\text{O})_3 \cdot x\text{H}_2\text{O}$ thin films on modified QCM-gold electrodes – water sorption isotherms" (2007) submitted (*Microporous Mesoporous Mater.*)
- Presentations**
- E. Biemmi, "Direct Growth of HKUST-1 Thin Films on Self-assembled Monolayers: Control of Crystal Orientation and Vapor Sorption-Measurements" 19. Deutsche Zeolith Tagung, 2007, Leipzig, Deutschland.
- E. Biemmi, "Layers of Porous Materials on Gold Substrates: Linking Chemistry for Sensing Applications" 17. Deutsche Zeolith Tagung, 2005, Giessen, Deutschland
- E. Biemmi, "Morphological Evolution of Oriented HKUST-1 Crystal-Layers on Different Functionalized SAMs on Gold Substrates" 19. Deutsche Zeolith Tagung, 2007, Leipzig, Deutschland.
- E. Biemmi, "Layers of Porous Materials on Gold Substrates: Linking Chemistry for Sensing Applications" FEZA 2005, Prag, Tschechien.
- E. Biemmi, A. Darga, K. Möller, A. Müller, T. Bein and J. P. Kotthaus, "Lab-on-a-Chip: Nanostructured Building Units for Parallel Analysis" CeNS-Winterschule, 2003, Seeon, Deutschland.

VI. Appendix



"Nano-Lego Star"

Eight-point star generated by intergrown cubic MOF-5 crystals. Nano-sized molecular building blocks are assembled in a symmetric construction. The picture of a gold-coated sample was collected on a JEOL JSM-6500F scanning electron microscope, operating at 3 kV. (Short-listed at the 2006 RMS International Micrograph Competition)